

Dislocation Based Modelling of Fusion Relevant Materials



Daniel Celis Garza

University of Oxford

Harris-Manchester College

Department of Materials

Supervisors: Edmund Tarleton & Angus Wilkinson

A thesis submitted for the degree of

Doctor in Philosophy

Hilary Term 2021

Dedication

“Ohana significa familia, y tu familia nunca te abandona, ni te olvida.”
“Ohana means family, family means nobody gets left behind, or forgotten.”
– Stitch, Lilo & Stitch

Malle santa, cuando te hablé desde el trabajo para darte la noticia me dijiste que siempre lo supiste. Recuerdo que lloraste en el teléfono, se te cerró la garganta y a mí también. A diferencia de otras veces, no pudimos platicar mucho porque nos quedamos sin aliento. Así que le hablaste a abuelita Raquel mientras le hablé a papá. Madre, David y yo te debemos tanto que no podemos repagar en mil vidas, pero ten por seguro que eres nuestro ejemplo a seguir. Nuestra madre chingona y chambeadora, solo hay una y como ella no hay ninguna. Sin tí el mundo sería un lugar más cruel y pobre, no merece un ángel tan grande y puro como tú.

Dad, “Igualito que tu jefe, wey.” con tu risa característica fue lo primero que dijiste cuando te avisé “Sí dad, igualito que mi jefe.” entre risas respondí. Como siempre, no platicamos mucho pero esta vez porque le querías avisar a abuelita Teté y a mis tíos, y yo le quería avisar a David. Pensé que seguirías aquí para carcajearte al verme en la túnica ridícula, así como lo hicimos nosotros cuando te vimos a tí en la tuya. Escribo esta dedicatoria antes de acabar porque una promesa es una promesa y esta madre la voy a acabar. No te tendré para pedirte consejos y contarte mis avances y tropiezos. Pero a veces pretendo que me escuchas mientras intento comprender o arreglar algo. Te queremos y te extrañamos muchísimo. Buenas noches, dad.

David, “Te mamaste we.” me dijiste cuando me abrazaste al llegar a casa después del trabajo el día que me aceptaron. Me has hecho un chingo de falta ojete, te extraño mucho we. Perdón por no hablar tan seguido, pero me duele colgar we. No estoy tan chisqueado como mamá pero siento feo cuando terminamos de platicar. Me gusta mucho ver tus streams porque me recuerda un poco a sentarme a tu lado a verte jugar... o a cuando veíamos Twitch juntos y veíamos a TB “missing legal”.

Esto es para mi Ohana por sangre y por elección. Ustedes creyeron en mí cuando yo no lo hacía. Me empujaron a ser mejor. Me extendieron la mano cuando nadie más lo hizo. Me hicieron reir cuando solo sabía llorar. Gracias por hacerme quien soy.

This is for my Ohana by blood and by choice. You believed in me when I did not. You pushed me to be better. Offered me a helping hand when nobody would. Made me laugh when all I knew was sorrow. Thank you for making me who I am.

Acknowledgements

“You can always judge a man by the quality of his enemies.”

– Oscar Wilde

I did not get here alone. Truly I don't have much idea what I did to deserve the help and encouragement of such an eclectic mix of incredible people. The list is long, but like the proverbial beating of a butterfly's wings, there is no telling where I'd be without the aid and support of these people.

- Ed and Angus, I have no idea what I did to deserve your guidance and support.
- Fusion CDT
- Harris-Manchester
- We would like to thank Prof. Sylvain Queyreau and Lawrence Livermore National Laboratory for their invaluable input.
- Anatoly Kolomeisky, John F. Stanton
- Isla
- Clan del Rano Sentado
- Goosehood
- Kopse Lane Krump v1.0 and v2.0
- Kristmas Karnage: # n
- OUPLC: Perhaps the heaviest things that we lift are not our weights, but our feels.
- Damian Rouson
- Bruce Bromage, Haiyang Yu, Fenxian Liu, Daniel Hortelano-Roig, Junnan Jiang

I guess I'll content myself with being judged unfavourably by the world.

Contents

List of Figures	iii
List of Tables	vi
List of Algorithms	vii
0 Preface	1
0.1 Notation and abbreviation	1
0.2 Typesetting	2
0.3 Diagrams	2
1 Introduction	3
1.1 Materials science and history	3
1.2 Fusion energy production	4
1.2.1 Operating environment	4
1.2.2 Effects of radiation on reactor materials	6
1.2.2.1 Radiation Damage	6
1.2.2.2 Transmutation	7
1.3 Parallel computing	8
1.3.1 Computation on graphics processing units	10
1.3.1.1 Hurdles for parallelisation	12
1.4 3D dislocation dynamics modelling	15
1.4.1 Coupling dislocation dynamics to finite element methods .	16
1.4.1.1 Superposition model	16
1.4.1.2 Discrete continuum model	17
1.4.1.3 Level set method	19
1.4.2 Non-singular continuum theory of dislocations	21
1.4.3 Analytical forces exerted by a dislocation line segment on surface elements	24
1.4.4 Multiphase simulations	26
1.4.4.1 Polycrystalline materials	27

1.4.4.2	Inclusions	30
1.4.5	Parallelising discrete dislocation dynamics	32
1.5	Project outline and new science	34
2	EasyDD v2.0	37
2.1	Bug fixes	37
2.1.1	Correct time-adaptive integrator	37
2.1.2	Matrix conditioning	40
2.2	Research software engineering	44
2.2.1	Organisation	46
2.2.1.1	Source control	46
2.2.1.2	Folder structure	46
2.2.2	Modularisation	47
2.2.2.1	Encapsulation	47
2.2.2.2	Generic functions	48
2.2.3	Optimisation	50
2.2.3.1	Spurious memory allocation	50
2.2.3.2	Finite element optimisation	50
2.2.4	Misc quality of life improvements	51
2.3	Conclusions	52
3	Topology improvements	53
3.1	Collision	53
3.1.1	Hinges	53
3.1.2	Collision distance	55
3.2	Non-commutativity of topological changes	56
3.3	Conclusions	57
4	Dislocation-induced surface tractions	59
4.1	Numeric v.s. analytic tractions	59
4.1.1	Introduction	59
4.1.2	Theory	61
4.1.3	Methodology	67
4.1.4	Results and discussion	74
4.1.5	Conclusions	84
4.2	GPU parallelisation of analytic tractions	85
4.2.1	Introduction	85
4.2.2	Methodology	86
4.2.2.1	Data mapping	86
4.2.2.2	Parallelisation schemes	88

4.2.2.3	Maximising performance	90
4.2.2.4	Solving parallelisation problems	92
4.2.3	Results, discussion and conclusions	92
5	Simulations	95
5.1	Zinc tensile cantilever	95
5.1.1	Introduction	95
5.1.2	Methodology	95
5.1.3	Results and discussion	95
5.1.4	Conclusions	95
5.2	Tungsten cyclic loading and unloading cantilever	95
5.2.1	Introduction	95
5.2.2	Methodology	95
5.2.3	Results and discussion	95
5.2.4	Conclusions	95
6	Future work	97
7	Conclusions	99

List of Figures

1.1	Hohlraum design for indirect drive in Inertial Confinement Fusion.	6
1.2	Energy expenditure of CPU vs Voltage.	9
1.3	CUDA runtime schematic.	10
1.4	Memory access pattern example.	13
1.5	GPU and CPU asynchronous execution.	14
1.6	Explanation of warp divergence.	14
1.7	Superposition Model for DDD-FEM coupling.	16
1.8	The eigenstrain formalism.	18
1.9	Level set Dislocation Dynamics.	20
1.10	Analytic tractions on linear rectangular surface elements.	26
1.11	Modelling twinned multicrystals with DDD.	29
1.12	Modelling dislocation inclusion interactions with the discrete continuum model.	31
1.13	Parallelisation strategies for three problems in 3D DDD.	33
2.1	Node movement along dislocation line should have no drag contribution.	41
3.1	A single dislocation hinge can lead to three different final topologies.	54
3.2	Dislocation segments inside different collision radii.	55
4.1	Superposition Model for DDD-FEM coupling.	60
4.2	2D Gauss-Legendre quadrature on quadrangles.	63
4.3	Analytic tractions on linear rectangular surface elements.	63
4.4	Relative error comparison of analytic v.s. numeric tractions on a surface as a function of mesh coarseness.	67
4.5	Test cases for comparing numeric v.s. analytic tractions using an edge dislocation near a surface.	68
4.6	Sample analytical forces on an element as a function of angle between surface and segment.	69
4.7	FE nodes are shared between surface elements.	71

4.8	Set up comparing infinite-domain, singular solutions of stress fields to those obtained via a non-singular formulation with analytic and numeric tractions coupled to FEM.	73
4.9	Relative error for an edge dislocation perpendicular to a surface element.	75
4.10	Relative error for an edge dislocation parallel to a surface element.	76
4.11	Symmetry in stress fields leads more accurate numeric tractions.	77
4.12	Image stresses for an edge dislocation running parallel to a free surface with a Burgers vector perpendicular to the surface.	78
4.13	Image stresses for an edge dislocation running parallel to a free surface with a Burgers vector parallel to the surface.	79
4.14	Image stresses for a screw dislocation running parallel to a free surface.	80
4.15	Line plots of the infinite domain, analytic and traction image stresses.	81
4.16	Convergence of the image and total stresses as a function of distance from the free surface.	82
4.17	Line plots showing the convergence of the image and total stresses as a function of distance from the free surface.	83
4.18	Unloaded simulations using analytic and numeric tractions.	84
4.19	Memory access patterns.	87
4.20	Linear rectangular surface element mapping.	89
4.21	Sample parallel execution.	91
4.22	Parallel speedup on an NVidia GTX 750 and an Intel Core i5-8500 @ 3.0 GHz.	93

List of Tables

1.1	Estimated operating conditions of MCF and ICF fusion reactors.	5
4.1	Numeric v.s. analytic tractions. Unloaded simulation comparison.	74

List of Algorithms

2.1	Adaptive Euler-trapezoid predictor-corrector algorithm.	38
2.2	Improved adaptive timestep algorithm.	39
2.3	Bad way of avoiding drag matrix inversion singularity.	42
2.4	Dampening the drag matrix inversion singularity.	44
4.1	Calculating total force on a node using analytic tractions.	72

Chapter 0

Preface

0.1 Notation and abbreviation

For the sake of clarity the following notation and abbreviation conventions have been used:

- GPU: Graphics Processing Unit.
- CPU: Central Processing Unit.
- Tensors are denoted by sans serif bold italics, \mathcal{T} .
- Matrices are denoted by serif bold roman, \mathbf{M} .
- Vectors are denoted by serif bold italics, \mathbf{V} .
- Scalars are denoted by serif italics, S .
- Operators and special functions are roman, $\exp(x)$, $\det \mathbf{J}$.
- Angles are in radians unless otherwise stated.
- Einstein notation for tensor components is used unless otherwise stated.
- Individual items, be they nodes, surface elements, dislocation segments or indices are denoted by a lower-case subscript to the right, a_n .
- Ensembles are denoted by an upper-case subscript to the right, $a_N := \sum a_n$.
- Host variables (CPU variables in parallelisation) are denoted by a roman h-superscript on the left, $^h a$.
- Global device variables (global variables visible only to the GPU) are denoted by a roman d-superscript on the left, $^d a$.

- Thread variables (variables visible only to a GPU thread) are denoted by a roman t-superscript on the left, $^t a$.
- Serial indices/counters are the traditional $i, j, k \dots$
- Parallel indices are denoted as roman variables, a .
- Pseudo-code is C-style—row-major order, 0-based indexing—because it provides a more direct translation of the C-code.

0.2 Typesetting

The repository https://github.com/dcelisgarza/latex_templates contains the custom document class used to typeset this document. It was compiled with X_EL^AT_EX and B_IB_TE_X. We recommend compiling the source with X_EL^AT_EX or L_UaL^AT_EX. Compilation requires `minted`, <https://ctan.org/pkg/minted?lang=en>, and its dependencies.

0.3 Diagrams

All diagrams were drawn with Inkscape: Open Source Scalable Vector Graphics Editor, <https://inkscape.org/>, “Draw Freely.”

Chapter 1

Introduction

1.1 Materials science and history

Metals and alloys are of such importance to humankind that entire eras of our history have been defined by and named after discoveries and advances in metallurgy [1, 2]. A civilisation’s ability to gain mastery of the properties and usage of materials is often strongly correlated with its success in history [3]. The historical influence of metals and alloys has touched all areas of human existence, from fashion to warfare [4].

It should come as no surprise that a material’s use is often linked to its properties. When a civilisation learned to harness the properties of a novel material, its influence often grew as a result [5, 6]. Whether building a woodcutter’s axe or a fusion reactor, the mechanical behaviour and deformation of materials—metals and alloys in particular—are still among their most important properties for engineering applications.

Traditionally such properties have been largely studied via empirical methods such as tensile and compressive tests, beam bending, and indentation [7–9]. Such tests have mainly focused on macroscopic scales, thus offering bulk-averaged properties valuable for engineers. Unfortunately such tests only describe observed behaviours without truly elucidating the fundamental mechanisms behind them [10]. This has recently started to change with the advent of micro-scale testing, where tests can be performed on single crystals or individual crystal boundaries, and can even probe specific slip systems to see how they behave under various loading scenarios [11, 12]. The increased resolution and more thorough parameter control goes a long way in providing a window through which more fundamental behaviours can be observed and hopefully explained; thus providing a way of deconvoluting macroscopic observations into their constituent phenomena [13, 14].

However, understanding the underlying mechanisms behind empirical results

through experimental means has proven difficult at every scale [15, 16]. Fortunately modelling and simulation can be powerful allies in this task. In particular, the study of dislocations is experimentally challenging [17–19]. By virtue of being such an important player in the mechanical properties of materials, dislocations demand careful study from both empirical and *in-silico* avenues.

The need for a more detailed picture of material properties is especially relevant in highly engineered alloys subjected to extreme conditions, such as those found in fusion reactors. The time-dependent shift in material properties and composition is of the utmost concern such extreme environments; radiation damage, large temperature gradients, gas diffusion and plasma instabilities provide the means for properties to change drastically over a components’ lifetime [20–22]. It is therefore imperative that we find ways of predicting and accounting for these changes. This requires a deeper understanding of the process driving the mechanical behaviour. Virtual experiments allow analysis and interpretation of micromechanical tests and can help provide new fundamental insight.

1.2 Fusion energy production

There currently exist two major branches of research for fusion energy production [23]: 1) magnetic confinement fusion (MCF) [24] which confines the plasma using magnetic fields and 2) inertial confinement fusion (ICF) [25] which uses a frozen fuel pellet which is either directly or indirectly compressed by arrays of powerful lasers. The physics and engineering challenges vary greatly between both approaches but the fundamental materials problems remain largely the same, with few exceptions such as divertors [26, 27].

1.2.1 Operating environment

One constant feature of nuclear energy production is ionising and non-ionising radiation. In the case of fission, this is mostly in the form of low energy neutrons and residual radiation of fission products; fusion on the other hand, deals with the sparsely explored 14 MeV neutron spectrum [28]. The lack of appropriate sources of suitably energetic neutrons [29] has meant that modelling, and searching for experimental analogues of damage cascades have become a crucial part of materials research [30].

Operating environments change vastly between ICF and MCF as described by table 1.1 [31]. The table should be read with a measure of skepticism as the numbers and conditions are approximate because they are not yet fully known, especially for ICF. However it is still, a fairly reasonable first approximation into

Location	Radiation Type	MCF (ITER)	ICF (LMJ)
1 st Wall	Neutron flux	$3 \times 10^{18} \text{ m}^{-2} \text{ s}^{-1}$	$1.5 \times 10^{25} \text{ m}^{-2} \text{ s}^{-1}$
	Neutron fluence*	$3 \times 10^{25} \text{ m}^{-2}$	$3 \times 10^{18} \text{ m}^{-2}$
	γ -ray dose rate	$2 \times 10^3 \text{ Gy s}^{-1}$	$\sim 1 \times 10^{10} \text{ Gy s}^{-1}$
	Energetic ion/atom flux	$5 \times 10^{19} \text{ m}^{-2} \text{ s}^{-1}$...
1 st Diagnostic	Neutron flux	$1 \times 10^{17} \text{ m}^{-2} \text{ s}^{-1}$	$1 \times 10^{26} \text{ m}^{-2} \text{ s}^{-1}$
	Neutron damage rate	$6 \times 10^{-9} \text{ dpa s}^{-1}$	negligible
	Neutron fluence*	$2 \times 10^{24} \text{ m}^{-2}$	$\sim 1 \times 10^{19} \text{ m}^{-2}$
	Neutron damage	$1 \times 10^{-1} \text{ dpa}$	negligible
	γ -ray dose rate	$\sim 1 \times 10^2 \text{ Gy s}^{-1}$	$\sim 1 \times 10^{10} \text{ Gy s}^{-1}$
	Energetic ion/atom flux	$\sim 1 \times 10^{18} \text{ m}^{-2}$...
	Nuclear heating	1 MW m^{-3}	0
	Operating temperature	520 K	293 K
	Atmosphere	Vacuum	Air
Other	EM pulse	...	$10 \text{ to } 500 \text{ kV m}^{-1} @ 1 \text{ GHz}$
	Shrapnel	...	$1 \text{ to } 10 \text{ km s}^{-1} @ \sim 30 \mu\text{m}$

Table 1.1: Estimated operating environment comparison between MCF (ITER) and ICF (LMJ). Reproduced from [31]. Note these numbers are unrepresentative of actual fusion power plants as both ITER and the LMJ are experiments—it is likely power plants will require much harsher operating conditions.

* End of life.

the materials requirements for both “mainstream” types of fusion energy production. That said, the components needed for energy harvesting—a divertor in the case of MCF, and an open problem for ICF—are conspicuous by their absence.

Table 1.1 shows that dosages and dosage rates vary wildly between approaches. For the most part, MCF receives higher doses of neutrons and ions in both the first wall and diagnostic equipment. This seems to indicate that the material requirements for MCF are stricter than for ICF. However, shrapnel production is a strong possibility in ICF, especially in indirect drive reactors; where a specially made container called a “hohlraum” holds the fuel pellet and is subsequently obliterated when the pellet undergoes fusion (see fig. 1.1 [32]). This is a huge challenge as such high energy shrapnel would be capable of destroying diagnostic equipment and damaging the first wall [33–35].

Overall, the table is unrepresentative of potential operating environments in large-scale power stations, but sets lower limits on the demands of the materials involved in both “mainstream” proposals for fusion energy production.

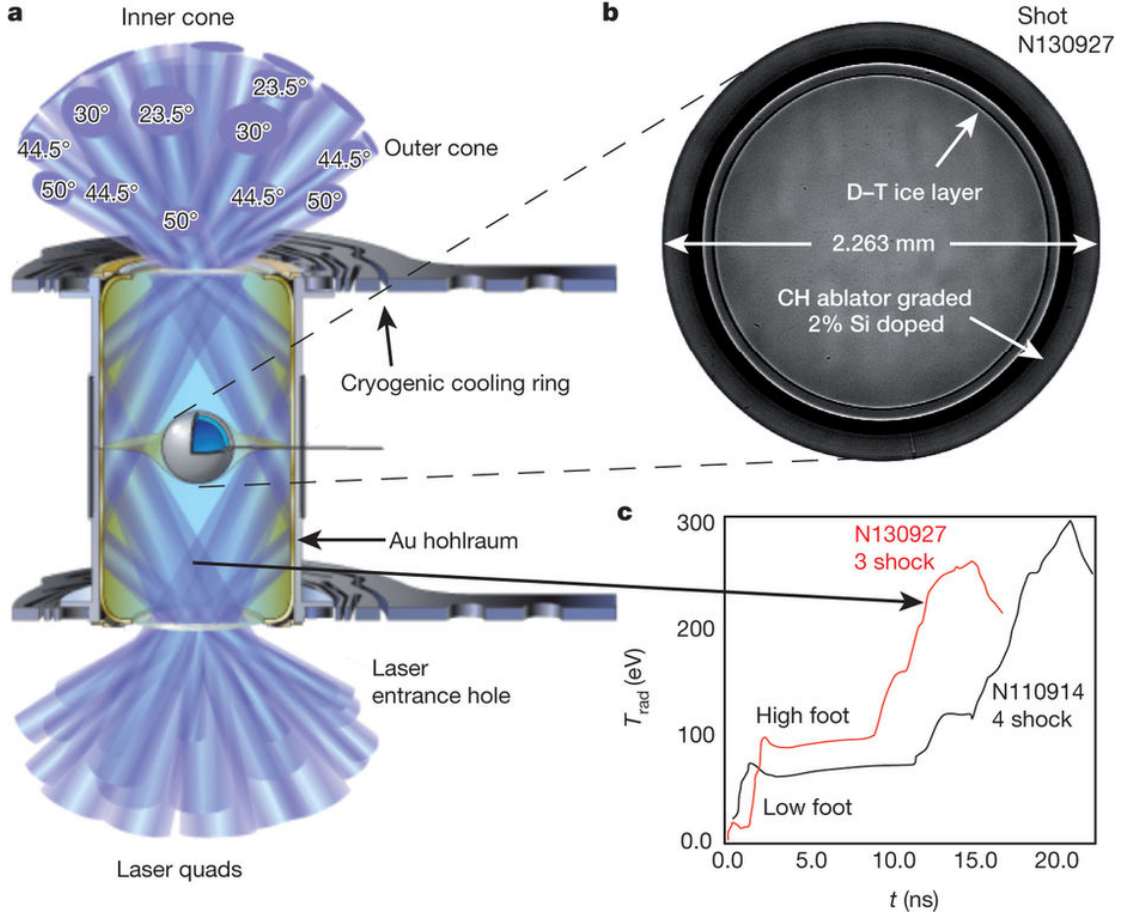


Figure 1.1: **a**, Cross section of the National Ignition Facility’s ICF target design showing the gold hohlraum and plastic capsule, fuel pellet, and incident laser bundles. **b**, X-ray image of the actual capsule for N130927 with DT fuel layer and surrounding CH (carbon–hydrogen) plastic ablator. **c**, X-ray radiation drive temperature as a function of time for the National Ignition Campaign (NIC) low-foot implosion and the post-NIC high-foot implosion. Image taken from [32].

1.2.2 Effects of radiation on reactor materials

1.2.2.1 Radiation Damage

One of the bigger problems in radiation damage research is the lack of a truly standardised way of measuring damage on materials [36]. The most common unit is displacements per atom (dpa) [37]. It is defined as the average number of displacements undergone by each atom in a material as a result of being irradiated. The “fundamental” unit of measurement for this is the number of displacements per unit volume per unit time, R

$$R = N \int_{E_{\min}}^{E_{\max}} \int_{T_{\min}}^{T_{\max}} \phi(E) \sigma(E, T) v(T) \, dT \, dE , \quad (1.1)$$

where N is the atom number density (no. of atoms per unit volume); E the incoming particle's energy; T the energy transferred in a collision of a particle of energy E and a lattice atom; $\phi(E)$ the energy dependent particle flux; $\sigma(E, T)$ the cross section for the collision of a particle with energy E resulting in a transfer of energy T to the struck atom; and $v(T)$ the number of displacements per primary knock on atom as a function of transferred energy T . DPA can be calculated by naïvely multiplying R by the sample volume and total exposure time (or we could use fluence rather than flux). This ignores the fact that $\sigma(E, T)$ and $v(T)$ will be locally perturbed in the neighbourhood of damage cascades, since the bulk volume is much greater than that of the damage cascades', we assume the functions remain globally unchanged.

In principle, this is a rather good measure of damage [37]. The catch is that generalised, analytical expressions for $\sigma(E, T)$ and $v(T)$ depend on a slew of parameters and are therefore incredibly hard if not impossible to derive. This does not mean they cannot be discretised and roughly approximated via Monte Carlo (MC) approaches [36–38]. However, damage cascade modelling falls squarely in the realm of pico- to nanosecond timescales and as such only feasable with Molecular Dynamics (MD) and Kinetic Monte Carlo (KMC) [39, 40] approaches. At the end of such cascades, we are often left with dislocation sources or prismatic dislocation loops [41] which can be used as inputs by a Dislocation Dynamics (DD) simulation to study larger temporal and spatial scales [30].

1.2.2.2 Transmutation

Transmutation products are one of the biggest sources of problems for materials in fusion applications [20, 21]. Not only do they tend to embrittle materials, they often also reduce their thermal conductivity [42]. The former presents significant challenges for structural materials [43]; the latter is especially egregious for energy extraction by limiting the divertor's ability to conduct heat thus lowering the reactor's efficiency and causing thermal stresses due to the generation of hot spots that cannot be easily dissipated. As a result, understanding the mechanical and thermal behaviour of transmutation alloys is crucial for moving forward [44–46] but doing so requires knowledge of the time evolution of a reactor's components. Because the composition changes in a non-trivial way, so do the mechanical properties. Worse still are the long timescales over which this happens—on the order of years or tens of years [47]. Even if we were able to experimentally irradiate fusion-relevant materials with appropriately energetic neutrons, it would take years before we could characterise their behaviour, and doing so would be problematic due to radioactive decay.

The way we go about addressing the time-dependent compositional change of a material is to model it. Culham Centre for Fusion Energy's (CCFE) FISPACT [48] software takes an MC approach at calculating transmutation and decay products of a sample given certain conditions. The code utilises external data provided by the European Activation File which provides cross sections and decay rates for a wide range of isotopes [49]. Unfortunately there is a lack cross section data for certain neutron energies that contribute in a non-negligible manner to a fusion environment. Interpolating to fill the gaps would not be appropriate as the data is non-smooth and subject to resonance peaks, so the solution is imperfect.

Transmutation products will always be problematic, but they are a fact of working with fusion-relevant materials. Fortunately there are ways in which inclusions may be modelled via DD (section 1.4.4.2). DD may also be used to model dislocation movement and interaction within heterogenous media (section 1.4.4) as is the case for oxide-dispersion-strengthened (ODS) steels; and transmutation alloys of Tungsten divertors, where Osmium, Rhenium and Tantalum clusters which prove highly problematic for its temperature conductivity and structural integrity [50–56].

1.3 Parallel computing

Processing chips are made up of millions or even billions of transistors acting as switches in logic gates. Each time a logic gate fires, the capacitors inside them charge and discharge at the chip's frequency or clock speed [57]. Consider the power of any electronic component,

$$P(t) = I(t)V(t), \quad (1.2)$$

where I is current and V is voltage both as a function of time. The current, I , of a capacitor and the definition of power, P , as functions of time, t , are given by,

$$I(t) = C \frac{dV(t)}{dt}, \quad P(t) = \frac{dE(t)}{dt}, \quad (1.3)$$

where C is capacitance and E the energy stored in the capacitor. Substituting eq. (1.3) into eq. (1.2) and integrating twice, we obtain the expression for the energy stored in a capacitor,

$$E_c = \frac{CV_c^2}{2}, \quad (1.4)$$

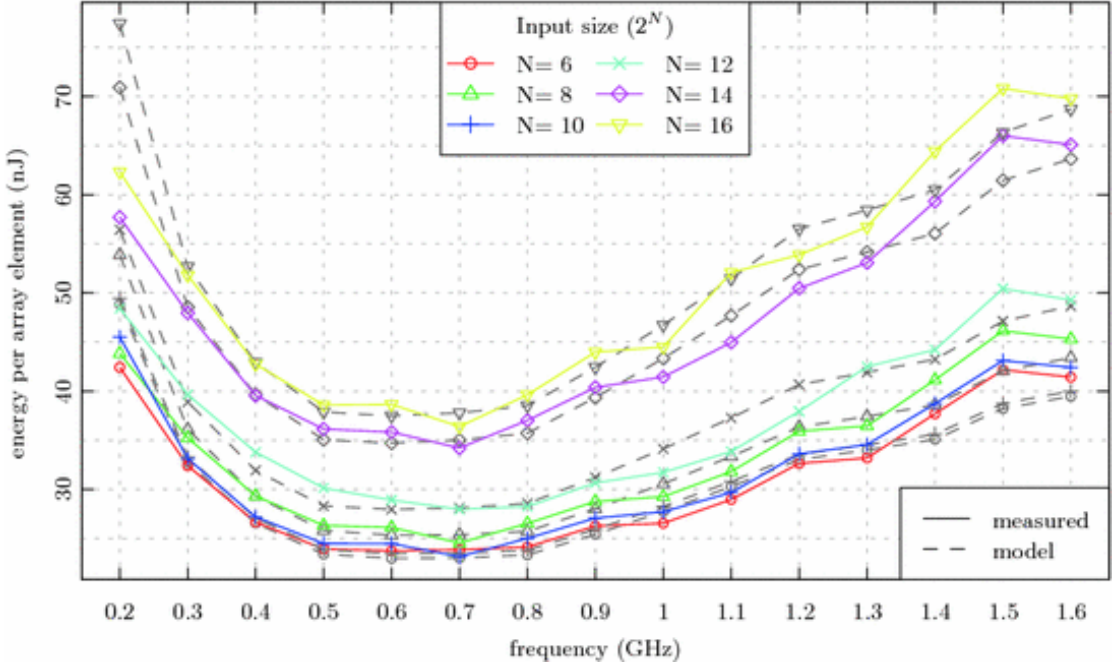


Figure 1.2: Energy required by a Samsung Galaxy S2 CPU at 37 °C to complete the Gold-Rader implementation of the *bit-reverse* algorithm. The dashed lines denote a theoretical model, image and model found in [60].

where V_c and E_c are the voltage and energy stored in the capacitor. Recalling that in a processing chip, the capacitors are charged and discharged at the chip's clock speed f , we arrive at the expression for power consumption, P_c , of a capacitor charging and discharging at frequency f [58],

$$P_c = E_c f \propto CV_c^2 f. \quad (1.5)$$

Computer chips are rather more complicated, but their power consumption (also known as power dissipation) is described by a simple addition of terms [59],

$$P = P_{\text{dyn}} + P_{\text{sc}} + P_{\text{leak}}, \quad (1.6)$$

where P_{dyn} is the dynamic power dissipation given by eq. (1.5). The two other dissipation mechanisms are: 1) short-circuit, sc , which depends on frequency and occurs when a direct path from transistor to ground is made as a result of multiple transistors conducting simultaneously; and 2) leakage, leak , which depends on the voltage and is due to micro-currents between doped parts of a transistor. Furthermore, higher voltages and frequencies result in higher temperatures, which in turn mean decreased transistor performance and increased capacitance. The overall result is an energy expenditure curve similar to fig. 1.2 [60] for every processor unit.

This set of optimum conditions is the reason behind the multicore and multi-

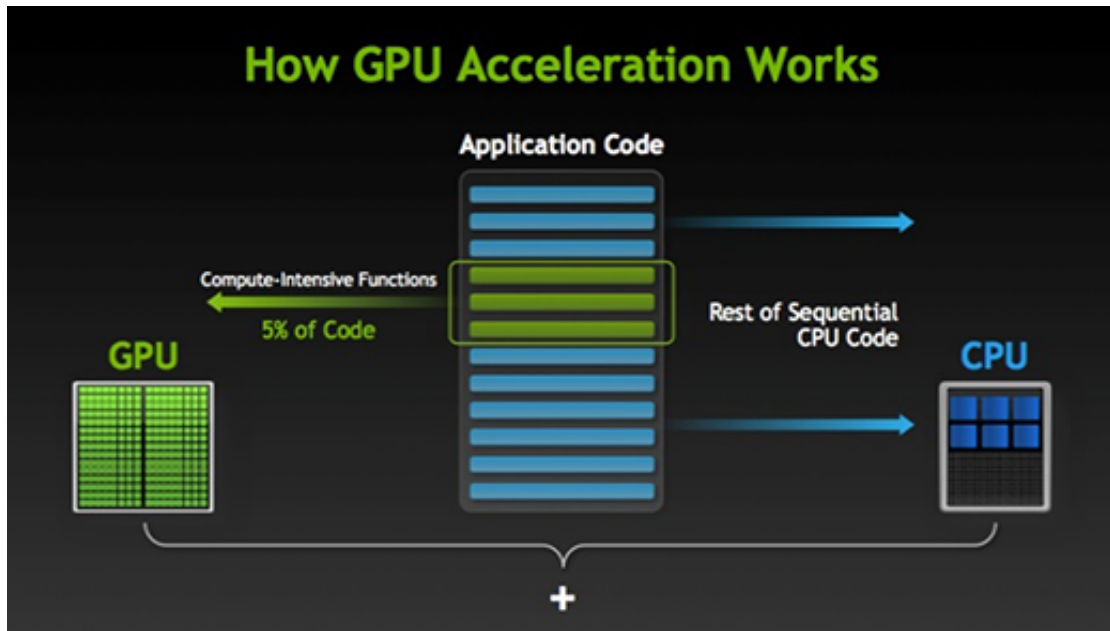


Figure 1.3: CUDA runtime schematic. Repetitive but computationally intensive tasks can be offloaded to the GPU. Both GPU and CPU are completely independent from each other and can work on different parts of the code at the same time, care must be taken to ensure proper synchronization. Image taken from [61].

threaded design of modern Central Processing Units (CPUs) and Graphics Processing Units (GPUs). It is also why in recent years there has been such a massive push for parallelism in all computing markets. It is simply not feasible to continually increase clock speeds and voltages because cooling solutions would struggle to remove heat fast enough, and power consumption would skyrocket.

1.3.1 Computation on graphics processing units

Central Processing Units (CPUs) are designed not only to perform mathematical operations but logical ones that control program flow. They are tailored to perform the wide variety of operations required by an operating system. These include program scheduling (load balancing), instantiation (program loading, unloading, loops, recursion instances) & branching (if/case statements, go to's), memory operations (fetching, storing, allocation), input/output (IO), and program monitoring (program counters, recursion counters). Modern CPUs have a degree of parallelism that allows them to increase their total throughput while keeping their operation within near optimum conditions as previously mentioned. They are commonly divided into cores and threads, though certain high-end chips have an additional layer named hyperthreading [62].

Given the limited scope of the first computers, the general purpose of CPUs was enough to cover their needs. With the advent of personal computers, the demands

on CPUs drastically increased. For industrial users these revolved around data acquisition, filtering and preprocessing [63–65]. On the other hand, the domestic market demanded ever increasing levels of abstraction and usability in the form of Graphical User Interfaces (GUIs) such as windows, cursors and their accompanying sound effects. Manufacturers identified this and moved to provide specialised modules that freed CPU resources and improved user experience by accelerating different processes through hardware means [66–69]. These modules include Sound Cards (SCs), Field Programmable Gate Arrays (FPGAs), Graphics Processing Units (GPUs), Application Specific Integrated Circuits (ASICs), Cryptographic Accelerators, Regular Rxpression (RegEx) Accelerators, among others. They are collectively dubbed “hardware accelerators”.

Graphics Processing Units were originally intended to offload the very data-intensive but computationally simple operations needed for 3D gaming and rendering [66–68]. Graphics processing was seen as a prime candidate for hardware acceleration because the operations on each pixel are largely the same across the screen. Due to their original purpose as gaming and rendering accelerators, they were never designed to operate on higher than single precision data. In fact, single precision (32-bit precision) is still good enough to encode 32-bit colour depth (8-bit channel per RGB colour + 8-bit alpha channel), which only the most high-end monitors support [70]. It is also worth noting that because the same operations apply to different pieces of (mostly) independent data, they can all be performed at the same time, often trivially reducing the order of polynomial complexity algorithms.

As previously mentioned, GPU parallelism frees up enormous amounts of CPU processing power that can be put to good use running other programs or performing complementary serial processes, while the GPU works concurrently on its dataset. Parallelism has been used by the scientific community for years, but the focus has mainly been on CPU parallelism [71]. Consequently, its scope was largely limited to the use of computational clusters. The two main reasons for this were the fact that GPUs lacked support for higher precision arithmetic, and the very limited to non-existent support for scientific computing in languages such as OpenGL [72].

It wasn’t until the development of the OpenCL and OpenACC standards that GPUs caught the attention of the scientific community as a viable way of exploiting parallelisation without access to a computing cluster.

OpenCL allows one to work with heterogeneous systems and is similar to C in that it’s very low level. It works on a wide range of hardware accelerators and is therefore useful for many scientific and engineering applications, but it’s also relatively hard to use. One can make use of libraries written in OpenCL to

facilitate development, but it is still a fully fledged C-type language [73].

OpenACC is similar to OpenMP in that they both use pragmas¹ and they both work in shared memory environments—same GPU and same CPU respectively. This is no coincidence as OpenACC was designed as an extension of OpenMP for developing parallel applications on hardware accelerators. Unfortunately, being pragma based, the standard requires significant work by compiler manufacturers, so its adoption has therefore been slow [74]. Furthermore, despite simplifying development and minimising the barrier to entry, the use of pragmas limits the flexibility and adaptability of the framework compared to OpenCL.

Recently however, a third option has become increasingly viable. NVidia’s Computer Unified Device Architecture (CUDA) framework provides the best aspects of both OpenCL and OpenACC. The tradeoff is that it only works on NVidia GPUs and is a closed source product. However, the accessibility and flexibility of CUDA provides anyone familiar with C/C++ the means to develop a GPU application with little issue. NVidia is also strongly backing scientific research by adding double precision support on their GPUs. They have also worked to provide parallel equivalents of well known serial libraries—such as cuBLAS & cuFFT—for scientific computing. They have additionally developed a wide range of specialist graphics cards tailor-made for scientific purposes. As such, they are the leaders in GPU computing in scientific communities [61].

1.3.1.1 Hurdles for parallelisation

The difficulty in parallelisation varies tremendously from problem to problem. Problems where data is uncorrelated and independent—such as sampling well-behaved probability distributions—are almost trivially parallelisable. Problems where data is correlated or strongly dependent on its neighbours—such as Dislocation Dynamics—require a more careful approach [75].

The largest hurdle when implementing parallel algorithms is often the efficient use of data. In order to obtain good parallel performance, a lot of thought has to be placed on data access patterns, data read/write conflicts, and memory allocation and transfer [61]. For best performance, all this must be analysed on a case by case basis. If done incorrectly, the performance of a parallel application may be lower than the serial version. One must consider a wide range of parameters to

¹Pragmas are especially formatted comments that specific compilers recognise and turn into special instructions (often for moving memory to the appropriate hardware) at compile time. They are not part of the programming language’s official standard, but rather compiler-specific extensions. Pragmas are usually programmed in C or Assembly and must be implemented by the compiler manufacturer. Nothing prevents application developers from writing the would-be pragma’s code directly into their application, but this can prove a lengthy and difficult process. The rigid nature of pragmas, and the compiler manufacturer’s priorities limit their scope and usability.

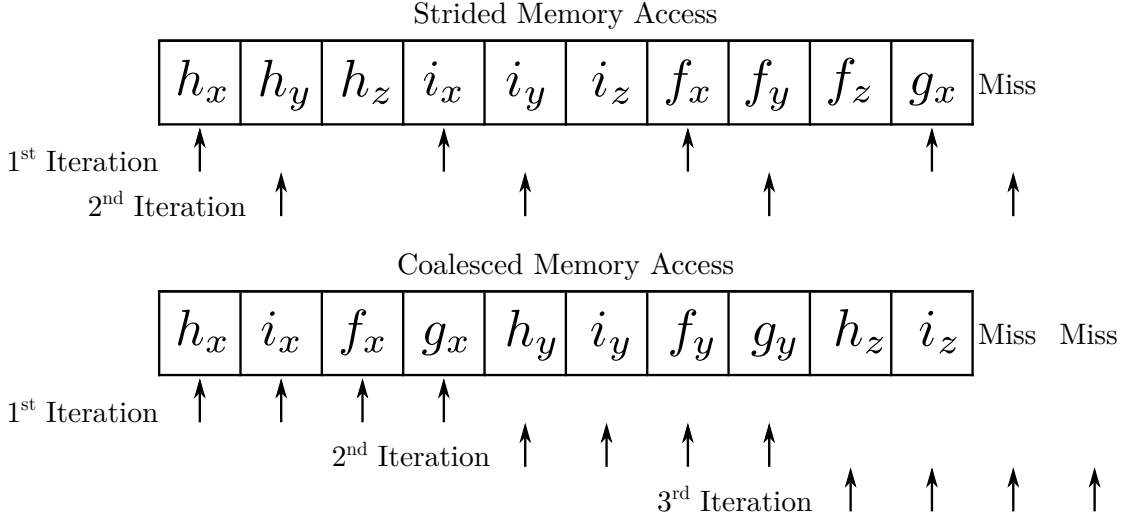


Figure 1.4: Arrows represent fetch requests by single threads in a GPU. Data should be arranged in such a way that all threads in a warp (collections of 32 threads) access contiguous memory locations to reduce time-consuming memory fetch operations. This is often unintuitive but extremely important, especially on scientific computing cards which are optimised for long computational times and low memory fetch frequency.

successfully parallelise a problem. Among these are GPU architecture, problem size, computational and memory complexity, code branching, required arithmetic precision, and error tolerances [61, 76].

Efficient parallelisation of many problems requires “coalesced memory access” as shown in fig. 4.19, which means we have to be extremely careful when mapping CPU memory to global GPU (device) memory. The fact that threads work “simultaneously”² means that in order to obtain good performance, data which is to be “simultaneously” loaded into each thread must be contiguous. This maximises cache memory use and therefore reduces slow memory fetch operations to global or shared memory.

Special cases, such as having a parallel dislocation line segment to a surface as discussed in section 1.4.3, must be treated carefully due to the way code branching works in GPUs. There are various ways of doing so: 1) if the special case is inexpensive, it can be treated within the same GPU function; 2) if the special case is expensive and always known (certain boundary conditions in FEM), it can be placed in its own GPU function that treats it separately; 3) if the special case is expensive and found at runtime it may be asynchronously treated by the CPU or buffered into its own GPU function to be executed at a later time.

One of the advantages of GPU-CPU independence is that both can work concurrently on the problem. If both systems have to talk to each other, then one

²Not quite but essentially simultaneously. See [61] for details.

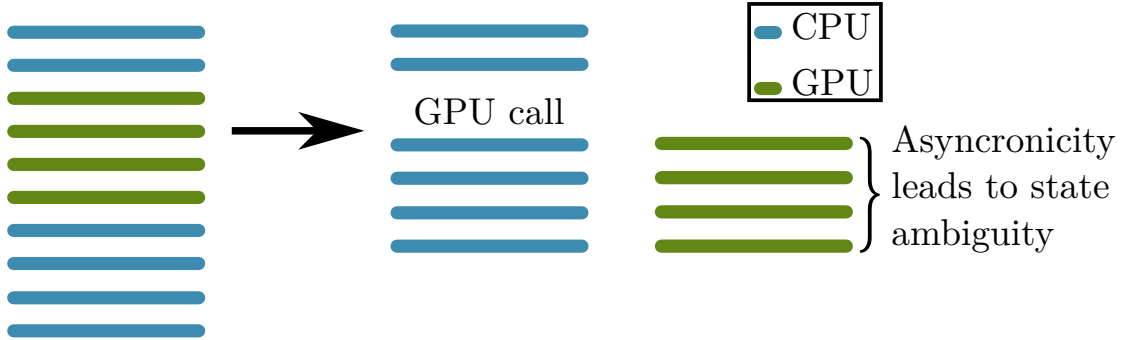


Figure 1.5: GPU and CPU code run independent of each other. Leads to state ambiguities if both sides need to talk to each other [61].

```

if (y == 0){
    x = a+b;
}
else if (y == 1){
    x = a*b;
}
else{
    x = a/b;
}

```

```

p = (y == 0);
p: x = a+b;
p = (y == 1);
p: x = a*b;
!p: x = a/b;

```

(a) CPU code will only execute if the condition is met. This is called code branching.

(b) GPU code executes every line but only stores results if the flag before the colon is true.

Figure 1.6: The NVidia CUDA compiler replaces **if** and **case** statements with logical flags **p**. Every line is executed, but the data is only stored if the flag prior to the colon is true [61]. This means that having rare but computationally expensive special cases will tank parallel performance and must therefore be dealt with separately.

must tread carefully, ensuring proper syncronisation and data mapping before moving (see fig. 1.5).

The reason why code branching is bad for GPU parallelisation is down to the fact that they work like software customisable vector machines. Where collections of threads all carry out the same operation on different pieces of data at the same time. This means that regardless of whether a condition is true or false, the code will execute. It is only data storage that depends on the condition, as illustrated in fig. 1.6.

Dislocation Dynamics (DD)—in particular 3D Discrete Dislocation Dynamics (3D DDD)—can greatly benefit from parallelisation, especially when coupling to Finite Element Methods (FEM). It is worth noting that there are potential issues arising from the very computationally expensive functions and special cases that often arise from analytical solutions in 3D DDD. There are also potential issues

with data redundancy—which are non-limiting in the short term—that may eventually require a more data-efficient approach as the computational capabilities and data capabilities of GPUs converge. Section 1.4.5 expands on these issues in the context of DD.

1.4 3D dislocation dynamics modelling

The plastic deformation of materials is generally governed by the generation and motion of line defects known as dislocations through the crystal lattice. Microstructural features such as grain boundaries, precipitates and inclusions impede dislocation motion causing strengthening but often limiting ductility [77]. Understanding the behaviour of the dislocation ensemble is highly complicated even when ignoring dislocation-microstructure interactions. However, if we want to truly comprehend their real-world behaviour, we cannot limit ourselves to idealised scenarios.

One of the most often used parametrisations of DD is Discrete Dislocation Dynamics (DDD). Where dislocations are parametrised as a series of nodes linked by straight line segments. This reduces computational requirements and allows for analytic solutions to be obtained. At present, neither DDD or Finite Element (FE) models can truly handle all of the complexities of real-world alloys [78–81]. For one, DDD relies on assuming a linear-elastic isotropic solid domain with periodic boundary conditions, while FE relies on assuming continuum properties inside its *finite* domain.

Crystal Plasticity Finite Element Methods (CPFEM) use constitutive equations to calculate dislocation motion and generation on a set of slip systems. These are given as dislocation densities and thus are still “bulk” models because they don’t interact with each other [82]. CPFEM can handle finite strains and anisotropy but not strain localisation/slip bands, etc.

Furthermore, dislocations often accumulate in the vicinity of microstructural features. The interaction of dislocations with microstructure can lead to further increased hardening and local hot spots in stress that can lead to failure initiation [83, 84]. Hardware acceleration, i.e. using Graphics Processing Units (GPUs), has been shown to be very effective in DDD [85], and has the potential to enable the simulation of much larger numbers of dislocations for longer timescales. In order to study these phenomena we must find a way of coupling DDD and FEM into a single multiscale model that can simulate micromechanical tests more accurately than CPFEM. With a model such as this we may potentially be able to predict and observe emergent phenomena/properties, explain micromechanical behaviours, and even predict and explain experimental results based on underlying dislocation

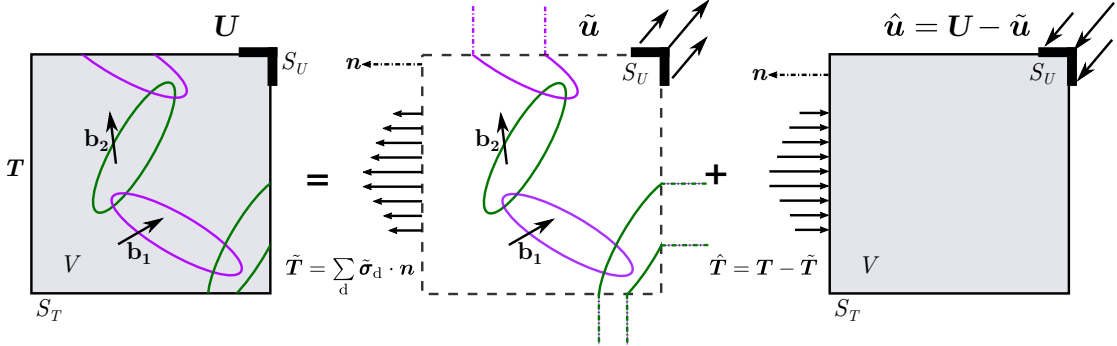


Figure 1.7: Decomposition of the boundary value problem. The volume V is bounded by surface S contains a dislocation ensemble and is subjected to initial traction conditions \mathbf{T} on S_T and \mathbf{u} on S_u . First, the traction, $\tilde{\mathbf{T}}$, and displacement, $\tilde{\mathbf{u}}$, fields due to the dislocations in the infinite domain (DDD) are evaluated on the boundaries S_T and S_u respectively. Then a traditional FE method is used to calculate the stress field satisfying the boundary conditions $\hat{\mathbf{T}} = \mathbf{T} - \tilde{\mathbf{T}}$ and $\hat{\mathbf{u}} = \mathbf{u} - \tilde{\mathbf{u}}$. Image edited from [86].

mechanisms.

1.4.1 Coupling dislocation dynamics to finite element methods

Coupling dislocation dynamics (DD) to FEM is important to properly simulate micromechanical tests because DD provides us with a more precise set of inputs and greater granularity for solving the FE problem. There are at present two methods with which to do so, the Superposition model and the Discrete continuum model. The most accurate implementation of dislocation dynamics is discrete dislocation dynamics, where the dislocation is broken into nodes and connecting segments. This is computationally efficient and allows for analytical solutions. However, as discussed in section 1.4.1.3 explicit discretisation is not the only way to tackle the problem.

1.4.1.1 Superposition model

The Superposition Model (SM) works by decomposing the problem into separate DDD and FE problems (fig. 1.7). It is assumed that a linear-elastic body V bounded by a surface S is subject to traction boundary conditions, \mathbf{T} , on S_T and displacement boundary conditions, \mathbf{u} , on S_u . The formulation proposed in [87] to impose traction-displacement boundary conditions on DDD problems in finite domains states that the total displacement and stress fields can be written as a

superposition of displacement and stress fields obtained from DDD and FE,

$$\mathbf{u} = \tilde{\mathbf{u}} + \hat{\mathbf{u}}, \quad (1.7a)$$

$$\boldsymbol{\sigma} = \tilde{\boldsymbol{\sigma}} + \hat{\boldsymbol{\sigma}}. \quad (1.7b)$$

The (\sim) fields are those associated with the dislocation in an infinite medium and are obtained by evaluating analytic fields in a DDD simulation. While the corrective $(\hat{\cdot})$ fields are those which must be superimposed to ensure the boundary conditions are met. This means that the image fields can be obtained by running a FE simulation with the “corrected” displacement and traction fields,

$$\hat{\mathbf{u}} = \mathbf{u} - \tilde{\mathbf{u}}, \quad (1.8a)$$

$$\hat{\boldsymbol{\sigma}} \cdot \mathbf{n} = \hat{\mathbf{T}} = \mathbf{T} - \underbrace{\tilde{\mathbf{T}}}_{\tilde{\boldsymbol{\sigma}} \cdot \mathbf{n}}, \quad (1.8b)$$

where \mathbf{n} is the outer unit normal vector to S . As a dislocation segment moves closer to the surface, its (\sim) field diverges and starts causing numerical problems [88]. A further problem with this method is that modelling elastic inclusions not only requires the calculation of forces induced by dislocations on the inclusion’s surface, but also demands the calculation of so-called polarisation stresses due to differences in the inclusion’s and matrix properties [87–89].

The relative simplicity of the superposition method has made it a popular choice [86, 90, 91] for coupling DDD and FEM because all it requires is the calculation of forces and displacements on the boundaries (see section 1.4.3).

1.4.1.2 Discrete continuum model

The Discrete Continuum Model (DCM) takes an alternative approach to solving the same problem. The DCM only treats short-range dislocation-dislocation interactions analytically while all other interactions are numerically calculated via FEM [92]. It is based on the regularisation of the atomic displacement jump across the slip plane into a plastic strain inclusion according to eigenstrain theory [93]. Like the Superposition Model, the DCM also assumes the simulated volume to be linear-elastic.

The eigenstrain formalism assumes that material defects can be represented as stress-free strain distributions dubbed eigenstrains [93]. For example, a dislocation loop of any shape may be approximately represented, thin, coherent, plate-like inclusion with the same contour as the loop and a characteristic thickness h as shown in fig. 1.8 [92]. The eigenstrain tensor, ϵ^P , can then be defined as

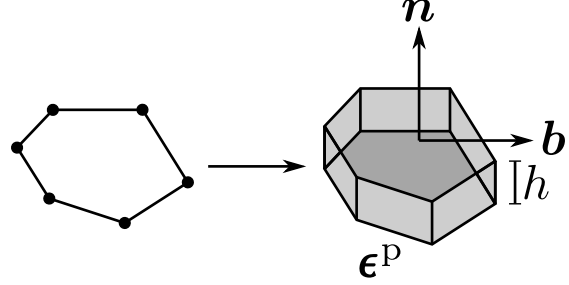


Figure 1.8: The eigenstrain formalism as defined in [93]. The dislocation is being approximated by a thin coherent inclusion of thickness h , whose strain-free stress tensor σ^p as defined by eq. (1.9). The vectors n and b are the normal vector to the slip plane and the dislocation line's Burgers vector.

a symmetric dyadic product of the Burgers vector, \mathbf{b} , and slip plane normal \mathbf{n} ,

$$\boldsymbol{\epsilon}^p \equiv \frac{1}{2h}(\mathbf{b} \otimes \mathbf{n} + \mathbf{n} \otimes \mathbf{b}). \quad (1.9)$$

eq. (1.9) can be used to calculate approximate elastic fields from the stress-free eigenstrain distribution. The approximation is accurate far from the dislocation core [94]. As we move closer but still outside of the core region, the approximation tends toward the exact discrete dislocation solution as $h \rightarrow 0$. Due to linear elasticity, the total plastic strain is the sum of the individual plastic strains due to each dislocation segment.

The formalism then lets us solve the boundary value problem by finding the stress tensor σ , elastic strain ϵ^e and displacement \mathbf{u} in mechanical equilibrium with the boundary conditions and plastic strain distribution $\boldsymbol{\epsilon}^p$ from the “inclusions”.

It is worth noting that in order to calculate the eigenstrains, there must be sufficient FE nodes inside the thin plate. Therefore smaller values of h necessitate finer FE meshes. Furthermore, the original DCM experienced numerical blow up as dislocation-dislocation distances approached h [95], but this has since been addressed. Assuming linear-elasticity, the revised model [92] yields,

$$\nabla \cdot \sigma + \mathbf{f} = \mathbf{0} \quad \in V \setminus \{A\}, \quad (1.10a)$$

$$\sigma = \mathbf{E} : \boldsymbol{\epsilon} \quad \in V \setminus \{A\}, \quad (1.10b)$$

$$[[\mathbf{u}]] \quad \text{across } \{A\}, \quad (1.10c)$$

$$\mathbf{u} = \mathbf{u}_0 \quad \in S_u, \quad (1.10d)$$

$$\sigma \cdot \mathbf{n} = \mathbf{T} \quad \in S_T. \quad (1.10e)$$

At time t , $\{A\}$ denotes the area swept by the dislocation loops since the start of the simulation. $[[\mathbf{u}]]$ denotes displacement jumps tangent to $\{A\}$ due to dislocation glide; its magnitude and direction depend on the Burgers vector \mathbf{b} . \mathbf{E} is the 4th-

order elasticity tensor, $\boldsymbol{\sigma}$ the small strain tensor, \mathbf{f} are the body forces and, $\cdot\cdot$, is the double dot product defined as, $(\mathbf{E} : \boldsymbol{\epsilon})_{ij} = E_{ijkl}\epsilon_{kl}$, for a rank 4 tensor \mathbf{E} and rank 2 tensor $\boldsymbol{\epsilon}$. The operator, \setminus , is the set difference defined as, $A \setminus B = \{x \in A | x \notin B\}$. We use the same notation for the volume, surface normal and boundary conditions as in section 1.4.1.1. eq. (1.10) can then be linearly decomposed three parts which are solved via FEM or DDD and coupled.

It is worth noting that the DCM is substantially more complicated than the SM. By requiring the finite elements be small enough for the eigenstate formalism to work, it strongly couples DDD to the FE model and software. It shifts the brunt of the computational workload from DDD to FEM. Essentially trading computationally intensive long range interactions which scale on the order of $\mathcal{O}(N^2)$, where N is the number of dislocation line segments; for computationally intensive tasks scaling on the order of $\mathcal{O}(M^3)$ where M is the number of finite elements in a cubic mesh with N elements per side. Furthermore, it cannot be used with BE methods as the eigenstrain formalism demands the use of internal elements rather than simply requiring a surface mesh.

That said, the DCM allows for reductions in the computational complexity of certain parts of the problem which would otherwise have to be done via DDD [92]; namely long-range dislocation-dislocation or dislocation-surface interactions via an interaction distance cutoff that is only possible with the eigenstrain formulation. Compared to the SM, gains in computational efficiency grow as dislocation density increases with respect to the number of finite elements. Since dislocation-dislocation and dislocation-surface interactions are among the most computationally expensive aspects of DDD, the DCM can reduce the overall computational cost of simulations with large enough dislocation densities.

1.4.1.3 Level set method

Even though the level set method has not strictly been used to couple DD to FEM, it has been used to model inclusions [96] as described in section 1.4.4.2. This type of dislocation dynamics is fundamentally distinct from DDD because Level Set DD uses arbitrary functions rather than a discretisation approach to represent dislocations lines. The idea is that in 3D, a dislocation $\gamma(t)$ can be represented by the intersection of two zero levels of two level set functions (see fig. 1.9),

$$\phi(x(t), y(t), z(t), t) = 0, \quad \psi(x(t), y(t), z(t), t) = 0, \quad (1.11a)$$

$$\frac{d\phi}{dt} = \partial_t \phi + \mathbf{v} \cdot \nabla \phi = 0, \quad \frac{d\psi}{dt} = \partial_t \psi + \mathbf{v} \cdot \nabla \psi = 0, \quad (1.11b)$$

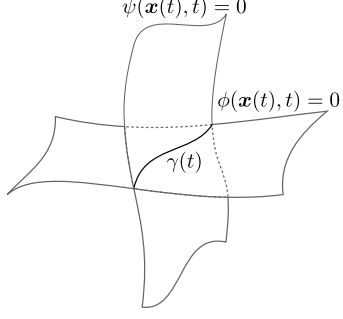


Figure 1.9: Diagram of a continuous dislocation $\gamma(t)$ as the intersection of the zero level of two level set functions $\phi(\mathbf{x}(t), t)$, $\psi(\mathbf{x}(t), t)$ as posed by eq. (1.11). Image edited from [97].

where \mathbf{v} is the dislocation velocity. This definition uses the material derivative because it is assumed that the function and its spatial coordinates are all functions of time, t . The material derivative also comes up when deriving the Navier-Stokes equations of fluid dynamics.

The level set method is significantly more computationally more expensive than DDD [97]. It must solve two coupled quasi-linear partial differential equations whose character is in general undefined. It therefore requires the use of very robust numerical solvers such as higher order Total Variation Diminishing (TVD) Runge-Kutta methods for time discretisation (TVD-RK4 or higher) and high order ENO (Essentially Nonoscillatory $\mathcal{O}(N^5)$ or higher) or WENO (Weighted Essentially Non-Oscilatory) interpolation methods for spatial discretisation [98] for the solutions to converge satisfactorily. The method also makes it impossible to obtain many of the useful analytical solutions one can find by discretising dislocations into straight line segments. Another problem is that this method has never been truly coupled to the finite element method. However, if one were to do so there are two naïve ways of going about it: 1) numerically integrating along the dislocation lines and finding a way to numerically calculate the forces on FE nodes, or 2) discretising the level set curves and using either the DCM or SM to find forces and displacements. The former would be very computationally expensive. Furthermore, no one has found a way to compute the forces or displacements exerted by generally shaped, non-discretised dislocations, numerical solutions are possible as they are needed to find self-interaction energies and dislocation-dislocation forces [97] but general, closed-form analytical ones are most likely impossible to find. The latter defeats the purpose of the level set method by abandoning the continuum framework. As a result of this, the level set method is not nearly as popular as DDD utilising either the SM or DCM.

1.4.2 Non-singular continuum theory of dislocations

The Peach-Koehler formula describes the fundamental interactions of dislocations [99] according to the force, \mathbf{f} , that a local stress $\boldsymbol{\sigma}$ exerts on a dislocation line with Burgers vector, \mathbf{b} , and line direction, $\boldsymbol{\xi}$,

$$\mathbf{f} = (\boldsymbol{\sigma} \cdot \mathbf{b}) \times \boldsymbol{\xi}. \quad (1.12)$$

According to [100], the internal stress field of a dislocation loop in a homogeneous, infinite, linear-elastic medium is given by the contour integral around a loop L ,

$$\sigma_{ij}^{\infty}(\mathbf{x}) = C_{ijkl} \oint_L \epsilon_{lnh} C_{pqmn} \frac{\partial G_{kp}(\mathbf{x} - \mathbf{x}')}{\partial x_q} b_m \, dx'_h, \quad (1.13)$$

where C_{ijkl} is the elastic stiffness tensor, ϵ_{lnh} the permutation operator, \mathbf{b} the Burgers vector, and $G_{kp}(\mathbf{x} - \mathbf{x}')$ is Green's function of elasticity [100]. $G_{kp}(\mathbf{x} - \mathbf{x}')$ is defined as the displacement component in the x_k direction at point \mathbf{x} in response to a unit point force applied in the x_p direction at point \mathbf{x}' [101]. In an isotropic elastic solid, $G(\mathbf{x} - \mathbf{x}')$, takes the form,

$$G_{ij}(\mathbf{x} - \mathbf{x}') = \frac{1}{8\pi\mu} \left[\delta_{ij} \partial_{pp} - \frac{1}{2(1-\nu)} \partial_{ij} \right] R(\mathbf{x} - \mathbf{x}'), \quad (1.14)$$

where μ, ν are the isotropic shear modulus and Poisson's ratio respectively, δ_{ij} is the Kronecker Delta, $\partial_{x_1 \dots x_n} \equiv \frac{\partial^n}{\partial x_1 \dots \partial x_n}$, and $R = \|\mathbf{x} - \mathbf{x}'\|$. However considering that $\mathbf{x} \rightarrow \mathbf{x}' \Rightarrow R \rightarrow 0 \Rightarrow \partial_i R \rightarrow \infty$, some (or all) components of the stress field diverge. Furthermore, the total elastic energy also diverges,

$$E = \frac{1}{2} \int S_{ijkl} \sigma_{ij}(\mathbf{x}) \sigma_{kl}(\mathbf{x}) \, d^3x, \quad (1.15)$$

where $S = C^{-1}$ is the elastic compliance tensor. These divergent properties often prove problematic when numerically computing dislocation forces and energies. Equation (1.15) can also be expressed as a double line integral [102, 103],

$$\begin{aligned} E = & -\frac{\mu}{8\pi} \iint_L \partial_k \partial_k R(\mathbf{x} - \mathbf{x}') b_i b'_j \, dx_i \, dx'_j \\ & - \frac{\mu}{4\pi(1-\nu)} \iint_L \partial_i \partial_j R(\mathbf{x} - \mathbf{x}') b_i b'_j \, dx_k \, dx'_k \\ & + \frac{\mu}{4\pi(1-\nu)} \iint_L \partial_k \partial_k R(\mathbf{x} - \mathbf{x}') b_i b'_i \, dx_j \, dx'_j \\ & - \nu \iint_L \partial_k \partial_k R(\mathbf{x} - \mathbf{x}') b_i b'_j \, dx_j \, dx'_i, \end{aligned} \quad (1.16)$$

which is important when describing how Cai et al. [101] derived their non-singular expression.

The singularity in R is the result of unreasonably and unphysically assuming a dislocation loop's Burgers vector distribution is a Delta function. The assumption was made to allow for closed-form and relatively simple expressions. As noted in [104], other distributions may be used but they either result in significantly more complicated expressions or destroy the analytical nature of the classical formulation.

There have been many attempts at removing this singularity, including finite-strain elasticity [105], non-local and gradient elasticity [106, 107], interaction cut-off radius [99], average stress at two points on opposite sides of the dislocation line [108, 109], and spreading the Burgers vector distribution out over a finite width [104, 110, 111]. Unfortunately all of these approaches failed in one way or another [101]. Depending on the approach, the following undesirable qualities may present themselves include inconsistencies, impractical implementation, lack of closed-form solutions for non-straight finite dislocations, lack of self-consistency, and the possibility for multiple expressions and solutions for the line integral of the dislocation line energy.

Cai et al. [101] took it upon themselves to define and justify a different Burgers vector distribution that maintains the mathematical convenience of the classical formulation that also eliminates such an unphysical assumption. They did so by introducing a Burgers vector density function,

$$\mathbf{b} = \int \mathbf{g}(\mathbf{x}) d^3\mathbf{x}, \quad (1.17a)$$

$$\mathbf{g}(\mathbf{x}) = \mathbf{b}\tilde{w}(\mathbf{x}) = \mathbf{b}\tilde{w}(r), \quad (1.17b)$$

where $r \equiv \|\mathbf{x}\|$. When substituting eq. (1.17a) into eqs. (1.13) and (1.16) the result of multiplying R with components of \mathbf{b} results in the following integrals,

$$R(\mathbf{x} - \mathbf{x}') b_m = \int R(\mathbf{x} - \mathbf{x}'') g_m(\mathbf{x}'' - \mathbf{x}') d^3\mathbf{x}'', \quad (1.18a)$$

$$R(\mathbf{x} - \mathbf{x}') b_m b'_n = \iint R(\mathbf{x}'' - \mathbf{x}''') g_m(\mathbf{x} - \mathbf{x}'') g_n(\mathbf{x}''' - \mathbf{x}') d^3\mathbf{x}'' d^3\mathbf{x}'''. \quad (1.18b)$$

Using eqs. (1.17) and (1.18) as guidelines, they defined the following convolutions,

$$w(\mathbf{x}) \equiv \tilde{w}(\mathbf{x}) * \tilde{w}(\mathbf{x}) = \int \tilde{w}(\mathbf{x} - \mathbf{x}') \tilde{w}(\mathbf{x}') d^3\mathbf{x}', \quad (1.19a)$$

$$R_a \equiv R(\mathbf{x}) * w(\mathbf{x}) = \int R(\mathbf{x} - \mathbf{x}') w(\mathbf{x}') d^3\mathbf{x}'. \quad (1.19b)$$

At which point they assumed there exists an integrable function $w(\mathbf{x})$ such that

$$R_a = \sqrt{R(\mathbf{x})^2 + a^2} = \sqrt{x^2 + y^2 + z^2 + a^2}, \quad (1.20)$$

where a is an arbitrary constant meant to represent the dislocation core radius whose value may be estimated from atomistic simulations. This is essentially a definition that can be used to replace R in the classical equations and eliminate the singularity by including a free parameter. However, in order to ensure this is mathematically sound, there must indeed exist a function which yields R_a as Cai et al. [101] defined it. This can be done by making use of the following property for the convolution of two suitably differentiable functions, $\partial_i(f*g) = \partial_i f * g = f * \partial_i g$. We may take the Laplacian twice,

$$\nabla^2[\nabla^2\{R(\mathbf{x}) * w(\mathbf{x})\}] = \nabla^2[\nabla^2 R_a(\mathbf{x})], \quad (1.21a)$$

$$\nabla^2[\nabla^2\{R(\mathbf{x})\}] * w(\mathbf{x}) = \nabla^2[\nabla^2 R_a(\mathbf{x})], \quad (1.21b)$$

$$\nabla^2[\nabla^2\{R(\mathbf{x})\}] = \nabla^2\left[\frac{2}{R}\right] = -8\pi\delta^3(\mathbf{x}), \quad (1.21c)$$

$$\nabla^2[\nabla^2 R_a(\mathbf{x})] = \nabla^2\left[\frac{2}{R_a} + \frac{a^2}{R_a^3}\right] = -\frac{15a^4}{R_a^7}, \quad (1.21d)$$

$$w(\mathbf{x}) = \frac{15a^4}{8\pi R_a^7}. \quad (1.21e)$$

Equation (1.21c) is a very brave, handwavy statement given that,

$$\nabla^2[R^{-1}] = \nabla^2[(x^2 + y^2 + z^2)^{-1/2}] = 0, \quad (1.22)$$

but may be physically “justified” by pretending $\nabla^2[R^{-1}]$ defines a spherical surface of radius 0. And eq. (1.21e) is a similarly handwavy statement that can be “justified” by noting that,

$$\lim_{a \rightarrow 0} w(\mathbf{x}) = \delta^3(\mathbf{x}). \quad (1.23)$$

Nevertheless, the non-singular formulation by Cai et al. [101] fixes the physically and mathematically problematic assumption that Burgers vectors follow 3D Dirac delta distributions, and proves useful in producing analytical expressions (see section 1.4.3) that are not much more complex than the singular case.

1.4.3 Analytical forces exerted by a dislocation line segment on surface elements

Whether using the SM or DCM, coupling DDD to FEM requires the traction field $\boldsymbol{\sigma}^\infty(\mathbf{x}) \cdot \mathbf{n}(\mathbf{x})$ to be distributed among the set of relevant discrete nodes of a FE or BE model. In the DCM model this applies to dislocations that are sufficiently close to the boundary; while in the SM, it applies to all dislocations. Regardless of the coupling model, the force exerted by a dislocation ensemble on a node n on element e is given by,

$$\mathbf{F}^{(n)} = \int_{S_e} [\boldsymbol{\sigma}^\infty(\mathbf{x}) \cdot \mathbf{n}(\mathbf{x})] N_n(\mathbf{x}) \, dS_e, \quad (1.24)$$

where dS_e is the infinitesimal surface element with surface area S_e . $N_n(\mathbf{x})$ are so-called shape functions (interpolation functions) that distribute the traction field among the surface element's nodes.

The problematic singularity associated with the classical Volterra dislocation is avoided by using the non-singular formulation of Cai et al. [101] discussed in section 1.4.2, which changes eq. (1.14) into eq. (1.25),

$$G_{ij}(\mathbf{x} - \mathbf{x}') = \frac{1}{8\pi\mu} \left[\delta_{ij}\partial_{pp} - \frac{1}{2(1-\nu)}\partial_{ij} \right] R_a(\mathbf{x} - \mathbf{x}'). \quad (1.25)$$

Using the non-singular definition of $G(\mathbf{x} - \mathbf{x}')$ in eq. (1.13) we obtain the expression for the stress field of a single straight dislocation line segment bounded by two dislocation nodes (1, 2) [101],

$$\begin{aligned} \boldsymbol{\sigma}^{(12)}(\mathbf{x}) = & -\frac{\mu}{8\pi} \int_{\mathbf{x}_1}^{\mathbf{x}_2} \left(\frac{2}{R_a^3} + \frac{3a^2}{R_a^5} \right) [(\mathbf{R} \times \mathbf{b}) \otimes d\mathbf{x}' + d\mathbf{x}' \otimes (\mathbf{R} \times \mathbf{b})] \\ & + \frac{\mu}{4\pi(1-\nu)} \int_{\mathbf{x}_1}^{\mathbf{x}_2} \left(\frac{1}{R_a^3} + \frac{3a^2}{R_a^5} \right) [(\mathbf{R} \times \mathbf{b}) \cdot d\mathbf{x}'] \mathbf{I}_2 \\ & - \frac{\mu}{4\pi(1-\nu)} \int_{\mathbf{x}_1}^{\mathbf{x}_2} \frac{1}{R_a^3} [(\mathbf{b} \times d\mathbf{x}') \otimes \mathbf{R} + \mathbf{R} \otimes (\mathbf{b} \times d\mathbf{x}')] \\ & + \frac{\mu}{4\pi(1-\nu)} \int_{\mathbf{x}_1}^{\mathbf{x}_2} \frac{3}{R_a^5} [(\mathbf{R} \times \mathbf{b}) \cdot d\mathbf{x}'] \mathbf{R} \otimes \mathbf{R}, \end{aligned} \quad (1.26)$$

Substituting eq. (1.26) into eq. (1.24) yields as many integrals as there are surface nodes. Their exact form depends on the shape functions used. The specifics are out of the scope of this work. For a rectangular surface element, the vector formulation can be converted into a set of local scalar coordinates via a series of

scalar projections of the set of basis vectors via eq. (1.27),

$$\begin{aligned}
\mathbf{R} &= \mathbf{x} - \mathbf{x}' = yt + r\mathbf{p} + s\mathbf{q}, & R_a &= \sqrt{\mathbf{R} \cdot \mathbf{R} + a^2}, \\
\mathbf{n} &= \mathbf{p} \times \mathbf{q}, & y &= \frac{\mathbf{R} \cdot \mathbf{n}}{\mathbf{t} \cdot \mathbf{n}}, \\
r &= \frac{\mathbf{R} \cdot (\mathbf{q} \times \mathbf{t})}{\mathbf{p} \cdot (\mathbf{q} \times \mathbf{t})}, & s &= \frac{\mathbf{R} \cdot (\mathbf{p} \times \mathbf{t})}{\mathbf{q} \cdot (\mathbf{p} \times \mathbf{t})}, \\
d\mathbf{x}' &= -\mathbf{t} dy,
\end{aligned} \tag{1.27}$$

where \mathbf{n} , \mathbf{p} , \mathbf{q} , \mathbf{t} are basis vectors³ that respectively correspond to the outside surface normal of the surface element, the two orthogonal vectors that define the sides of the rectangular surface element, and the dislocation line direction. The integral bounds can then be set up accordingly.

Noting that $\mathbf{n} \equiv \mathbf{p} \times \mathbf{q}$ is normal to the surface element, if \mathbf{t} is parallel to the surface element i.e. a linear combination of \mathbf{p} , \mathbf{q} then the product $\mathbf{t} \cdot \mathbf{n} = 0$, so this formulation is problematic when a dislocation line segment is parallel to a surface. An easy workaround is to slightly around the axis defined by $\mathbf{t} \times \mathbf{n}$ using the line's midpoint as a fulcrum. This works well in serial code but is problematic for parallelisation due to warp divergence (see section 1.4.5).

Figure 1.10 diagrammatically shows the definition of the four basis vectors and summarises the line integrals needed to find an analytical expression of the nodal force. It is worth noting that over 40 triple integrals arise from eqs. (1.26) and (1.27). These were solved via three families of recurrence relationships found via integration by parts and six seed functions found by direct integration. A more detailed description can be found in [86].

Quadratic triangular surface elements pose a much more challenging problem due to the fact that $\mathbf{p} \not\perp \mathbf{q}$. This property is not the only addition that significantly complicates the integrals, the interpolation functions are quadratic which increase the number of integrals. The non-orthogonality of \mathbf{q} , \mathbf{p} means the integration limits in the r , s coordinates must be parametrised appropriately and the integrations should be carried out in an order suitable for the chosen parametrisation. Aside from these technical considerations, the techniques for solving the problem for quadratic rectangular surface elements are the same as the linear rectangular case [86]. It is worth noting however, that the implementation of such a procedure may require quadruple precision arithmetic.

³Unitary vectors that define a space. This space is not orthogonal because in general only $\mathbf{p} \perp \mathbf{q}$, $\mathbf{n} \perp \mathbf{p}$ and $\mathbf{n} \perp \mathbf{q}$.

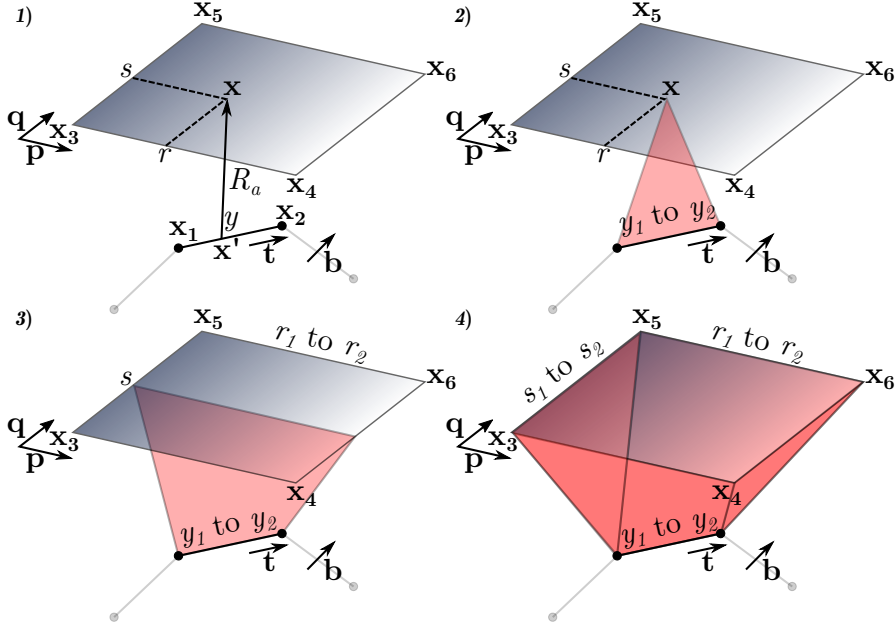


Figure 1.10: Diagram of the line integral method used to find analytical expressions for the forces exerted by dislocation on linear rectangular surface elements [86]. 1) For any given point \mathbf{x} on the surface element and any given point \mathbf{x}' on the dislocation line segment, define distance R_a . 2) Integrate from $x_1 \rightarrow x_2$ along line direction \mathbf{t} . 3) Integrate from $r_1 \rightarrow r_2$ along vector \mathbf{p} . 4) Integrate from $s_1 \rightarrow s_2$ along vector \mathbf{q} .

1.4.4 Multiphase simulations

Modelling heterogeneity in DDD remains challenging. The core assumption of DDD is that we have a homogenous linear elastic space with invariant properties. However, modelling multiphase systems such as multicrystals and inclusions necessitates a weakening of such assumptions, particularly the space's homogeneity. Multiphase models are also necessary to apply DDD to more realistic scenarios.

Fusion in particular is riddled with examples of highly heterogeneous materials. As previously mentioned, neutron bombardment often causes clustering of transmutation products particularly on divertor and first wall materials; such clusters often substantially change many of their mechanical and thermal properties. The whole point of Oxide-Dispersion Strengthened (ODS) steels [112] is to hamper radiation damage by distributing oxide inclusions within their matrix. If we hope to model such alloys with DDD we must find a way to relax our homogeneity criteria.

Furthermore, many potential candidates for structural and even first wall materials of fusion reactors are designed with complex microstructures in order to resist thermal creep and radiation damage. Understanding dislocation behaviours near the crystal boundaries of these microstructurally complex materials is another niche where DDD simulations can shed light into the mechanisms that give

rise to these materials' desirable properties.

1.4.4.1 Polycrystalline materials

Polycrystalline materials have been studied using DDD, however most of these are in 2D. One of the easiest phenomena to investigate with 2D DDD are grain size effects [113, 114].

It is well known that much of the grain size strengthening effects arise from dislocation-grain boundary (GB) interactions including transmission, reflection, emission and absorption of dislocations [115, 116]; with transmission being the most typically observed.

The model depends on the grain boundary energy density, $E_{\text{GB}}(\delta\theta)$, where $\delta\theta$ is the crystallographic misorientation between neighbouring crystals; resolved shear stress, τ , on the incoming dislocation with Burgers vector \mathbf{b}_1 ; critical penetration stress for the GB, τ_{GB} ; and Burgers vector of the dislocation debris, $\Delta\mathbf{b} = \mathbf{b}_1 - \mathbf{b}_2$, left behind when the incoming dislocation, \mathbf{b}_1 , transmits through the grain boundary to become a dislocation with Burgers vector, \mathbf{b}_2 . The relationship may be approximated by,

$$\tau|\mathbf{b}_1|^2 \geq \tau_{\text{pass}}|\mathbf{b}_1|^2 = E_{\text{GB}}(\theta)|\mathbf{b}_1| + \alpha G |\Delta\mathbf{b}|^2, \quad (1.28)$$

where α is the material constant and G the shear modulus. The grain boundary energy density was proposed by [117] to have the simple form,

$$E_{\text{GB}} = \begin{cases} k \frac{\delta\theta}{\theta_1} & 0 \leq \delta\theta < \theta_1, \\ k & \theta_1 \leq \delta\theta < \theta_2, \\ k \frac{\pi/2 - \delta\theta}{\pi/2 - \theta_2} & \theta_2 \leq \delta\theta < \pi/2, \end{cases} \quad (1.29)$$

where k , θ_1 , θ_2 , are material specific.

This is of course a gross simplification of the real 3D problem, but this approach was used by Li et al. [113] to investigate the Hall-Petch effect, which correlates grain size with flow stress of a polycrystal,

$$\sigma = \sigma_0 + \kappa \left(\frac{d_0}{d} \right)^n, \quad (1.30)$$

where σ_0 is the yield stress, d_0 a reference crystal size, κ the Hall-Petch slope and n the crystal size sensitivity parameter. Li et al. [113] showed that the model reproduces the Hall-Petch effect quite successfully. As a consequence, they showed that even what might appear as an overly simplistic approach can describe a

complex emergent phenomenon such as the Hall-Petch effect.

Aside from the Hall-Petch effect, the model has also been utilised by [114] to study the thickness effects of three different types of polycrystalline thin films: 1) no surface treatment, 2) surface passivation layer and 3) surface grain refinement zones . In this study, Frank-Reed sources were seeded across the domain, and the superposition principle was utilised to calculate displacement, strain and stresses in the thin films. Their results qualitatively reproduced experimental observations from expected dislocation patterns, stress distributions, and the eventual disappearance of the size effect as the films got thicker [114].

Two-dimensional models might seem useless but they have their place, particularly when thin films are concerned. However, they may also be of use when investigating the effects of dislocations on the mechanical behaviour of superconducting tape—whose applications range from medical imaging to fusion energy production. The exotic composition and crystallography of many superconductors (perovskites) would make 3D models very complex and computationally expensive, so 2D models may offer viable alternatives. On top of this, a superconducting tape’s operating environment would often have it under strains which might not strictly lie in-plane, but given a small enough segment of tape, strains orthogonal to the its plane may be neglected. Thus making 2D models an acceptable first attempt at tacking the problem, at leas before computational resources and developments in 3D models make more realistic studies of such complex systems possible.

The 3D case is substantially more complicated than the 2D case. A recent study by Fan et al. [118] looked at the role of twinning on the hardening response of polycrystalline Mg using 3D DDD.

The article is a perfect example of why 3D DDD is so much more complex than 2D DDD. Admitedly, it uses a material with a HCP crystal structure which complicates matters compared to FCC or BCC.

In 3D DDD one must account for dislocation-twin boundary (TB) interactions. These may be obtained via geometric considerations, MD, and experimental evidence [119–122]. We must have information regarding how dislocations are transmitted through a TB such as 1) whether a dislocation leaves a residual dislocation on the TB, 2) the possible pre-TB and post-TB slip planes a dislocation can be transmitted to, 3) which loading conditions are conducive to which transmission behaviour and 4) which types of dislocation can be transmitted or reflected and in what ways [118]. All this obviously depends on the twinning plane, so in order to study more realistic scenarios one must have all the necessary knowledge to properly account for all dislocation-TB interactions. Furthermore, it is possible that certain dislocations may leave behind twinning dislocations that end up as

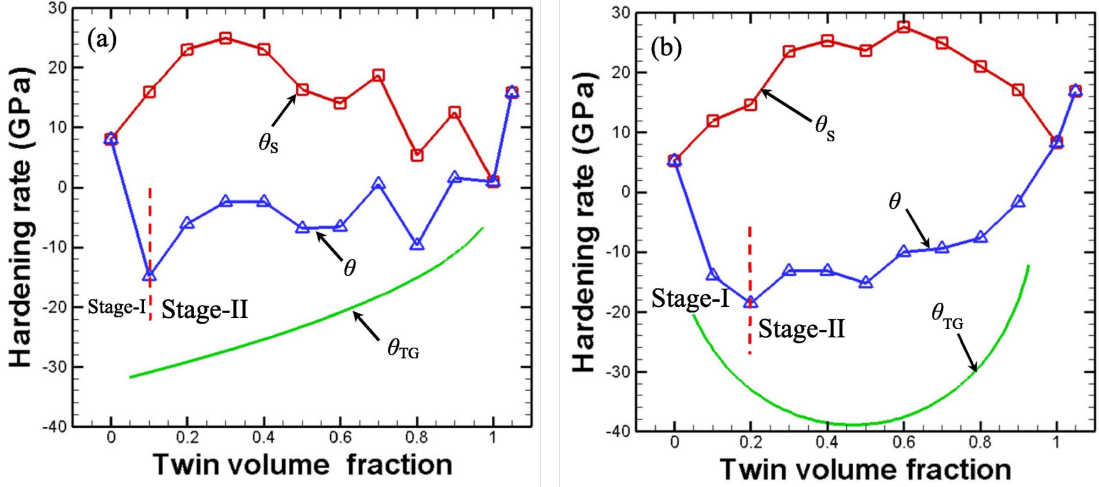


Figure 1.11: Simulated hardening rate as a function of twin volume fraction for (a) yz compressive loading and (b) tensile loading. Image edited from [118].

TB steps, whose movement can lead to TB migration and twin growth [123, 124].

Fan et al. [118] modelled four scenarios in order to deconvolute the effects that twins and grain boundaries have on the mechanical behaviour of a cubic crystal. They modelled 1) a cubic twinned polycrystal with two TBs and GBs on the edges of the cube, 2) a single crystal with no TBs or GBs, 3) a polycrystal with no TBs but GBs, 4) a twinned crystal with TBs but not GBs. It is worth noting that the effects of twin growth in plasticity were not accounted for in their DDD simulation and instead had to be numerically computed via the hardening rate θ ,

$$\theta = \frac{d\sigma}{d\epsilon} = \frac{d}{d\epsilon} \left[E \left(\epsilon - \epsilon_{\text{slip}}^{\text{p}} - \epsilon_{\text{twin}}^{\text{p}} \right) \right] = \theta_s + \theta_{\text{TG}}, \quad (1.31\text{a})$$

$$\theta_{\text{TG}} = -\frac{d}{d\epsilon} [E \epsilon_{\text{twin}}^{\text{p}}] = -E \bar{m} \gamma_{\text{twin}} \frac{d}{d\epsilon} [f_{\text{twin}}], \quad (1.31\text{b})$$

where θ_{TG} is the hardening rate due to twin growth, \bar{m} the mean Schmid factor of the participating twins γ_{twin} the characteristic twinning shear and $\frac{d}{d\epsilon} [f_{\text{twin}}]$ is the change in the change in the twin volume fraction with respect to applied strain. These parameters must be empirically obtained.

With their model, Fan et al. [118] managed to qualitatively reproduce experimental observations, including the concave shape of strain-stress curves that arises from the competing hardening effect of TBs restricting dislocation motion (fig. 1.11), and the softening produced by twin growth as obtained from eq. (1.31b).

Twin boundaries in 3D are analogous to grain boundaries in 2D, given that they are coherent, narrow boundaries rather than messy, often incoherent grain boundaries. Consequently, grain boundaries are much harder to treat in 3D; instead, the community focuses on multiphase models where the details of dis-

location transmission between phases are ignored or simplified as mentioned in section 1.4.4.2.

1.4.4.2 Inclusions

Inclusions have been modelled using the three methods described in section 1.4.1. However, they have gone about it differently. The SM and DCM apply their formulations hierarchically to allow for dislocation motion into and out of the inclusion. Furthermore, being coupled DDD-FEM problems, the inclusions must also be appropriately meshed, oftentimes this means inclusion geometries are limited to the mesh type. However, FEM allows for the calculation of coherency stresses which are seen by the dislocations and cause dislocation localisation and forresting in the vicinity of inclusions, just as experimentally observed [125, 126].

The level set method, having never been coupled to FEM, takes a different approach. Where the particles can be modelled as a region where dislocations experience a user-defined force. Coherency stresses have so far been neglected, but their effects may be modelled with the use of functions akin to diffuse orbital functions used in theoretical and computational quantum chemistry. Within this framework the inclusions may be arbitrarily defined to have any smooth shape, especially if one were to use piecewise parametric fourier curves.

Dislocation-permeable inclusions have been simulated via the SM [125]. As mentioned in section 1.4.1.1, there is a need to calculate polarisation stresses due to differences in the elasticity of both phases. Using the same notation as section 1.4.1.1 this can be done by breaking up the image stress into,

$$\hat{\boldsymbol{\sigma}} = {}^m\mathbf{C}\hat{\boldsymbol{\epsilon}} \in V_m \quad (1.32a)$$

$$\hat{\boldsymbol{\sigma}} = {}^p\mathbf{C}\hat{\boldsymbol{\epsilon}} + [{}^p\mathbf{C} - {}^m\mathbf{C}]\tilde{\boldsymbol{\epsilon}} \in V_p, \quad (1.32b)$$

where m, p denote whether a variable belongs to the matrix or precipitate respectively and \mathbf{C} is the elastic stiffness tensor.

Yashiro et al. [125] not only modelled a cuboid inclusion, but bimetallic interfaces in 3D. They found that under the right conditions, dislocations can pass from one phase to the other. When a dislocation passes into a different phase, it leaves an antiphase boundary on the slip plane. Therefore, in order for a dislocation to move from one phase to another, it needs excess energy equal to the antiphase (APB) energy of the area it sweeps within the precipitate. This means that as a node passes from one phase to another, it feels a repulsive force F_b . The next dislocation moving along the same APB will then feel an attractive force F_b to dissolve the APB. Once both dislocations move into the new matrix, they form a superdislocation bound by the APB energy [127]. However, as the dislo-

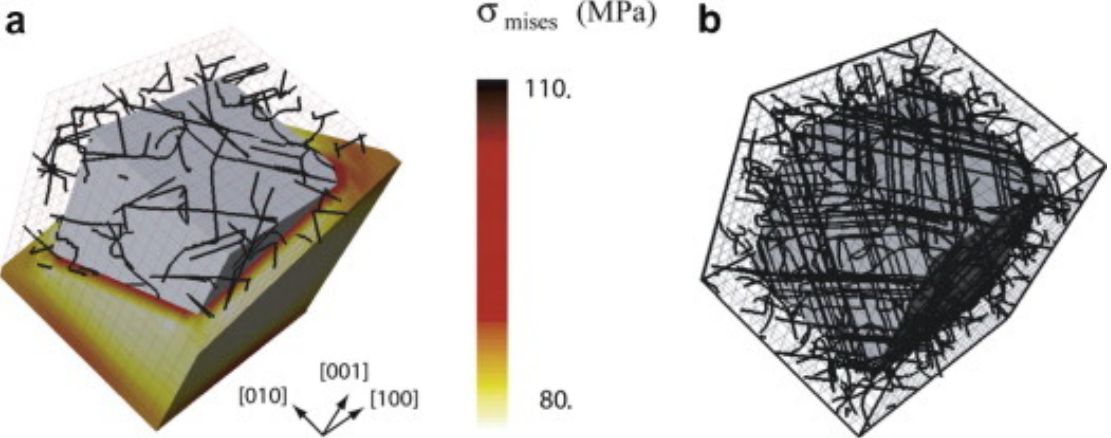


Figure 1.12: (a) Shows the initial dislocation configuration after relaxation in the presence of the calculated von Mises coherency stresses σ_{mises} . (b) Shows the dislocation forresting around the inclusion as a result of 0.2% plastic strain for the [001] case. Image obtained from [126].

tion length increases with respect to the precipitate's volume, the production of Orowan loops around it becomes more energetically favourable than moving into the new phase [125, 127]. Both of these behaviours have been observed when using the superposition method.

The eigenstrain method [128] as described in section 1.4.1.2 has been shown to be a viable solution to this problem. One can compute the stresses and displacements produced by the dislocation ensemble on the inclusions' surfaces via DCM or SM. The SM method however needs to calculate polarisation stresses [88], an operation that significantly increases the number of calculations necessary to solve the problem.

The DCM method has been used to simulate multiphase materials where the simulated dislocations reproduced experimentally observed behaviours such as the zig-zag patterns and dislocation forests produced by dislocations around precipitates in nickel superalloys [95, 126]. Reproducing such behaviours is not as trivial as simply adding inclusions to the simulation domain. In order to produce accurate results, one requires knowledge of the coherency stress between the different phases [126]. Such stresses are often due to lattice mismatches and differences in the thermal expansion coefficients. These coherency stresses localise the dislocations around the inclusions and are responsible for the observed localisation and aggregation of dislocations around precipitates as seen in fig. 1.12 [126].

The level set method has also been successfully used to model inclusions. In contrast to the aforementioned methods, they are assumed to be regions in space where dislocations experience a repelling force, instead of a region in space with distinct characteristics to the matrix. The force profile can be very simply defined to depend on the radial distance from the dislocation to a point in the “inclusion’s”

volume [96]. It can also be modulated depending on the nature of the inclusion by making the force a radial function, thus avoiding many of the numerical issues facing DDD-FEM couplings (see sections 1.4.1 and 1.4.3). It is also possible to make the inclusions impermeable or semi-permeable depending on the magnitude and steepness of the force gradient as presented in [96]. Arbitrarily shaped may also be possible if one were to also use angular components to the force function, or even through the use of spherical harmonics.

Though mathematically appealing, the level set method is far from representing the reality of dislocation-inclusion interactions. More realistic scenarios require use of more commonplace DDD-FEM coupling methods. Implementing arbitrarily shaped particles is not impossible in DDD—particularly if they can be discretised. Aside from the significantly lower computational requirements, one of the biggest advantages of DDD is that one can find tractions and displacements natively through either the DCM or SM, whereas the level set method requires the force to be user-defined and displacements on the inclusion are completely ignored. Furthermore, if the inclusion is a different crystal or a twin of the same material as in [118], it is possible to use the DCM or SM to study the transmission of dislocations from one phase to the other; something that is not yet possible to do with the level set method.

1.4.5 Parallelising discrete dislocation dynamics

It has been shown that DDD lends itself well to parallelisation. Ferroni et al. [85] investigated some of the more computationally intensive parts of DDD in DDLab [129], a freely available DD code for Matlab. The algorithms whose parallel performance was studied in [85] were 1. segment-segment interaction, 2. surface tractions and 3. image stresses.

The segment-segment interaction has $\mathcal{O}(N^2)$ computational complexity, where N is the number of dislocation segments. The quadratic scaling is due to the r^{-1} dependence of the dislocation stress fields, so long range interactions cannot be ignored.

Both the surface traction and image stress calculations have $\mathcal{O}(kN)$ computational where k is the total number of surface nodes and N the number of dislocation line segments.

As is usually the case in parallel computing, there is often more than one way to parallelise a problem. The optimal strategy depends on the problem itself. It was no different in [85] as shown in fig. 1.13. Ferroni et al. [85] realised that the segment-segment interaction calculation can be done via $\mathcal{O}(N^2)$ parallelism, where single pairs of dislocation segments are sent to a single thread, and then globally

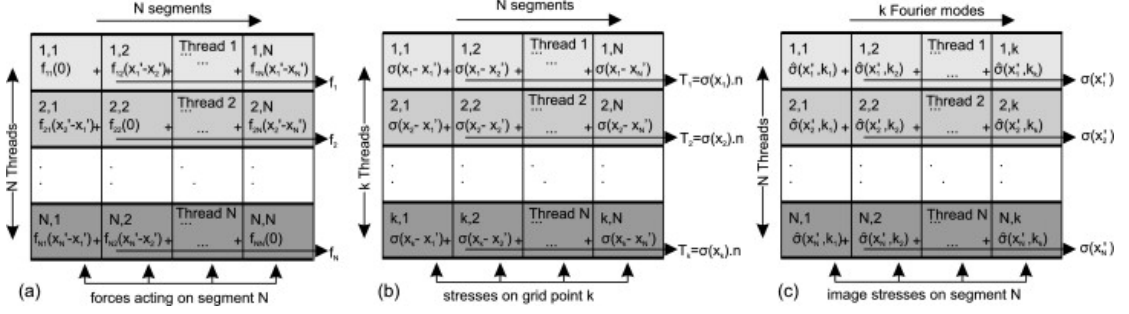


Figure 1.13: Parallelisation strategies for: (a) the N^2 segment interactions; (b) surface traction at k grid points and; (c) and image stresses on N segments. Image taken from [85].

reduced. However this approach requires $\mathcal{O}(N^2)$ memory and can lead to inefficient data reuse. So they opted instead for $\mathcal{O}(N)$ parallelisation and serialisation. In this scheme each thread is assigned a unique segment, and each thread computes the forces between its assigned segment and all the others while serially adding the force contributions. The memory access pattern they found best was that of a serial procedure, the reason is that in-thread calculations are serialised so having coalesced memory access patterns for threads would cause problems when serially accessing data for the calculation.

However, there is another approach Ferroni et al. [85] did not consider. It combines both of the aforementioned strategies, $\mathcal{O}(N^2)$ memory and $\mathcal{O}(N)$ parallelisation and serialisation. Such an approach requires two copies of the input data (one per access pattern). One pattern would allow each thread to obtain its uniquely assigned segment in a coalesced manner. The second would be the serial access pattern already present. Thus obtaining the best performance possible performance at the cost of doubling the required memory. This is a better strategy provided there is enough device memory⁴, if that is not so, the problem must be split into different GPU calls.

New NVidia architectures have made varying degrees of nested parallelisation possible, NVidia calls this “dynamic parallelism”. When applied to the computationally optimal solution, the $\mathcal{O}(N^2)$ memory requirement is relaxed to $\mathcal{O}(N)$ (with the same parallel-specific data structure) and $\mathcal{O}(N^2)$ computational parallelism.

The parallelisation strategies for the other two problems, (b) and (c) in fig. 1.13,

⁴Assuming the line direction is calculated inside the program, each dislocation line segment represents 3, 3-element vectors of type double (8-bytes per entry), totalling 72 bytes in global memory per dislocation line segment (two nodes + Burgers vector per segment). There must also be enough global memory to output the forces, which represent 1, 3-element vector of type double per dislocation node, totalling 24 bytes per node. Assuming a single dislocation loop with N nodes (therefore N segments), this brings the total global memory requirement to $96N$ bytes. Using two access patterns for the dislocation line segments and Burgers vector means an extra $72N$ bytes, giving a grand total of $168N$ bytes. Assuming the material parameters are stored in constant memory.

involved similar decompositions as the segment-segment interaction. For surface tractions Ferroni et al. [85] parallelised over k surface nodes with sequential calculation and addition of the stress from each dislocation line segment. For the image stresses, they chose the reverse strategy since it allows for the serialised addition of the image stresses on dislocation line segments.

Their findings showed very promising results for parallelising DDD simulations. Compared to C, their findings showed that depending on the specific problem and parameters used, the parallel implementation reduced computational time by a factor of ~ 110 at best and ~ 3 at worst for sufficiently large problems. This is of course, provided one uses a card designed for high performance computing, as these are tailored towards double precision arithmetic and computationally intensive procedures. However, gaming graphics cards are increasingly capable of double precision arithmetic and though not as drastic, speed ups are still substantial.

1.5 Project outline and new science

If anything should be clear from this work is that materials science is far from being solved. Even within the small niche of dislocation dynamics modelling, there are a huge number of open problems and an equally large number of solutions; each with its particular sets of advantages, disadvantages, ideoyncrasies and challenges.

The rapid advancement in computer technology; pushed by the ever-increasing complexity of the problems that occupy humankind; but simultaneously restricted by the physical constraints of classical computers, have opened up new avenues for research. Research that blurs the boundaries between fields and produces something new. Undoubtedly materials science sprang up this way, when metallurgists decided to take elements from the fields of chemistry, physics and mathematics to create a new discipline.

With increasing frequency, one finds people across vastly different fields who can understand each other via a common language. The language of scientific computing, where fields intertwine and produce new research methods; where techniques developed accross disciplines are taken, improved and adapted to work on the individual researcher's problem of interest.

This project applies such techniques to accelerate and improve the ease with which outstanding problems in materials science can be tackled; making use of more accurate models, hardware acceleration and the techniques of high performance computing to enable larger and more complex simulations than ever before—striving for increasingly faithful and insightful recreations of reality with a user-friendly code on a desktop PC.

Some of the work presented herein has already proven useful in the simulation

of complex simulations such as nano-indentation [130] and several other research projects within the Tarleton group. Here we showcase the new capabilities, findings and methods; improvements, fixes and redesign of the codebase; as well as a showcase of relatively simple, yet formerly inaccessible simulations resulting from this work. Finally, we present an ambitious proposal for future work resulting from the insights gained during the project.

Chapter 2

EasyDD v2.0

EasyDD can be found in <https://github.com/TarletonGroup/EasyDD>.

As mentioned in section 1.5, this project aims to integrate multidisciplinary skills for creating increasingly faithful recreations of reality in a user friendly way. This chapter details the software engineering that moved us closer to this goal and yielded a much improved version of EasyDD.

2.1 Bug fixes

2.1.1 Correct time-adaptive integrator

The first obvious hurdle to overcome when making more complex simulations possible was the tremendously long computational time taken for a dislocation plasticity simulation to sufficiently advance past the elastic regime. A simple microcantilever bending simulation with a few frank reed sources would take a whole night to reach the plastic regime, some early simulations by Bruce Bromage took days to get there.

The unacceptable slowness prompted a closer examination of the adaptive-time integration method found in algorithm 10.2 and described by equations (10.42, 10.45 and 10.46) found in [129, p. 214–216], an explicit Euler-trapezoid predictor-corrector solver. These are algorithm 2.1 and eq. (2.1),

$$\mathbf{r}_i^P(t + \Delta t) = \mathbf{r}_i(t) + \mathbf{g}_i(\{\mathbf{r}_j(t)\}) \Delta t, \quad (2.1)$$

$$\mathbf{r}_i(t + \Delta t) = \mathbf{r}_i + \frac{\mathbf{g}_i(\{\mathbf{r}_j(t)\}) + \mathbf{g}_i(\{\mathbf{r}_i^P(t + \Delta t)\})}{2} \Delta t, \quad (2.2)$$

$$\mathbf{v}_i := \frac{d\mathbf{r}_i}{dt} = \mathbf{g}_i(\{\mathbf{r}_j\}), \quad (2.3)$$

where \mathbf{r}_i are nodal coordinates, \mathbf{v}_i are nodal velocities, \mathbf{g}_i is the function that uses the mobility model and nodal forces to compute the nodal velocities, and the

superscript P denotes the predictor. This solver is fast and accurate for a small enough timestep Δt . Two free parameters Δt_{\max} and ϵ denote the maximum allowed timestep and accuracy.

Algorithm 2.1 Adaptive Euler-trapezoid predictor-corrector algorithm.

1. Initialise time step $\Delta t \leftarrow \Delta t_{\max}$.
 2. $\Delta t_0 \leftarrow \Delta t$.
 3. Compute $\mathbf{r}_i^P(t + \Delta t)$ and corrector $\mathbf{r}_i(t + \Delta t)$ from eq. (2.1).
 4. If $\max_i (\|\mathbf{r}_i^P(t + \Delta t) - \mathbf{r}_i(t + \Delta t)\|) > \epsilon$, reduce time step $\Delta t \leftarrow \Delta t/2$ and go to 3.
 5. $t \leftarrow t + \Delta t$.
 6. If $\Delta t = \Delta t_0$, increase time step to $\Delta t \leftarrow \min(1.2\Delta t, \Delta t_{\max})$.
 7. Return to 2, unless total number of cycles is reached.
-

The algorithm being used was not exactly this algorithm 2.1, as it used a different way of calculating the error but other than that they were the same. Unfortunately, this only increases the time step after converging to a satisfactory answer and advancing the time. So if anything caused the timestep to decrease, such as a collision or dislocation reaction, the time step would only increase very little every subsequent step, thus leading to unnecessarily small time steps in most cases. The original implementation of this is found in commit 65907b0 under the name `int_trapezoid.m`. An improved algorithm is described in algorithm 2.2. This algorithm takes close to the maximum allowed time step for the maximum allowable accuracy, $(\epsilon_{\max}, v_{\max})$, maximum and minimum timestep, $(\Delta t_{\max}, \Delta t_{\min})$ and number of iterations, iter_{\max} . It also uses a better error heuristic and more conservative timestep increase. It can be found in the most current version of `int_trapezoid.m`.

Algorithm 2.2 is more computationally expensive per iteration, but can increase the timestep much more rapidly than algorithm 2.1 without going through the rest of the simulation, which involves computationally expensive procedures. This improvement by itself let the early version of the software move through the elastic regime of our simulations orders of magnitude times faster than before. Simulations that took hours to days to reach the plastic regime, started doing so in minutes to hours. It also narrowed the gap between using different loading conditions, as the simulations could now effectively adjust the timestep to match the error tolerances much more easily than before. Both of which were a great

Algorithm 2.2 Improved adaptive timestep algorithm.

Convergent \leftarrow false, $\Delta t_{\text{valid}} \leftarrow 0$, iter $\leftarrow 0$, flag \leftarrow false

while Convergent **do**

- Compute $\mathbf{r}_i^P(t + \Delta t)$ and corrector $\mathbf{r}_i(t + \Delta t)$ from eq. (2.1).
- $\Delta \mathbf{r}_i \leftarrow \mathbf{r}_i(t + \Delta t) - \mathbf{r}_i^P(t + \Delta t)$
- $\bar{\mathbf{r}}_i \leftarrow \frac{\mathbf{g}_i(\{\mathbf{r}_j(t)\}) + \mathbf{g}_i(\{\mathbf{r}_i^P(t + \Delta t)\})}{2} \Delta t$
- $\epsilon \leftarrow \max_i (\|\Delta \mathbf{r}_i\|)$
- $v \leftarrow \max_i (\|\Delta \mathbf{r}_i - \bar{\mathbf{r}}_i\|)$
- if** $\epsilon < \epsilon_{\text{max}}$ and $v < v_{\text{max}}$ **then**

 - $\Delta t_{\text{valid}} = \Delta t$
 - $\gamma \leftarrow 1.2 \left(\frac{1}{[1 + (1.2^{20} - 1)(\epsilon/\epsilon_{\text{max}})]} \right)^{1/20}$
 - flag \leftarrow true
 - iter \leftarrow iter + 1
 - $\Delta t \leftarrow \max(\gamma \Delta t, \Delta t_{\text{max}})$

- else**

 - if** flag == true **then**
 - $\Delta t \leftarrow \Delta t_{\text{valid}}$
 - iter $\leftarrow \text{iter}_{\text{max}}$
 - else**
 - $\Delta t \leftarrow \Delta t/2$
 - end if**

- end if**
- if** iter $>$ iter_{max} or $\Delta t == \Delta t_{\text{max}}$ or $\Delta t < \Delta t_{\text{min}}$ **then**

 - Convergent \leftarrow true

- end if**

end while

$t \leftarrow t + \Delta t$

Proceed with the rest of the simulation.

boon to the usability of the code and to the research group's output capacity. This was the first major bottleneck to be fixed, which allowed us to identify and resolve previously unknown issues downstream.

2.1.2 Matrix conditioning

A common problem with dislocation dynamics is the tendency for some networks to have a large degree of variation in the speed of dislocation nodes [129, 131, 132]. This is a consequence of the fact that in discrete dislocation dynamics, nodes are simply the discretised representation of a dislocation line. As such, nodal motion must be constrained to the motion of dislocations, i.e. nodal movement must be consistent with how a dislocation glides, climbs and cross slips accounting for the dislocation character and orientation in the crystal. Moreover, dislocation motion can be assumed to follow a linear, anisotropic viscous drag model [129],

$$\mathbf{F}_{\text{drag}}(\mathbf{x}) = -\mathcal{B}(\boldsymbol{\xi}(\mathbf{x})) \cdot \mathbf{v}(\mathbf{x}), \quad (2.4)$$

where \mathcal{B} is a tensor constructed from the anisotropic drag that a dislocation node, \mathbf{x} , experiences as a result of its constrained velocity $\mathbf{v}(\mathbf{x})$ due to being part of a discretised segment $\boldsymbol{\xi}(\mathbf{x})$. In simple terms, this means a node experiences very different resistances to moving along its allowed directions.

Different mobility laws have different parametrisations for these directions. A problem that often plagues traditional mobility laws¹ is the movement of a node along a line segment itself. Having a node move along a single line segment has no effect on the energy of a network, as seen in section 2.1.2. Both structures are equivalent because the line—and thus the dislocation—does not change from one to the other, merely the limits of the line integral change. Therefore nodal movement along a line should not contribute to the total drag, and therefore have a zero line drag coefficient. On the other end of the spectrum we have climb, which is orders of magnitude less favourable than glide. But this can make eq. (2.7) singular, so its value is the careful balancing act of keeping the matrix invertible whilst keeping the associated energy cost of moving along a line low. This also causes nodal speeds along line directions to be much higher than other directions, which often limits the step size an integrator can take.

In the overdamped regime, $\frac{d\mathbf{v}}{dt}(\mathbf{x}) \rightarrow \mathbf{0}$, known driving forces (Peach-Köhler

¹Bruce Bromage, of [133] has developed a new BCC mobility law, `mobbcc1_bb.m` which can be found in the most current version of EasyDD. It solves many of the issues with traditional laws and is our new go-to for BCC materials. Among the things it fixes are: unreasonable cross-slip, pencil glide, and the problematic line-direction parametrisation. The drag matrix, \mathbf{B} , can still be singular however, so this law also includes the scale-averaged Marquardt-Levenberg regularisation.

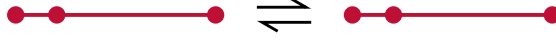


Figure 2.1: Node movement along dislocation line should have no drag contribution.

force + segment-segment forces + self-force) and the unknown drag force sum to give,

$$\mathbf{F}_{\text{drag}}(\mathbf{x}) + \mathbf{F}_{\text{drive}}(\mathbf{x}) = \mathbf{0}. \quad (2.5)$$

Substituting eq. (2.4) into eq. (2.5) and rearranging gives,

$$\mathcal{B}(\boldsymbol{\xi}(\mathbf{x})) \cdot \mathbf{v}(\mathbf{x}) = \mathbf{F}_{\text{drive}}(\mathbf{x}). \quad (2.6)$$

Strictly speaking, solving eq. (2.4) requires global knowledge of the network. The discretisation makes it possible to distribute \mathcal{B} along a line segment $i - j$,

$$\mathbf{B}_{ij} \leftarrow \oint_C N_i(\mathbf{x}) \mathcal{B}(\boldsymbol{\xi}(\mathbf{x})) N_j(\mathbf{x}) dL, \quad (2.7)$$

where C is the whole network, N_i and N_j are simply shape functions that interpolate quantities given the relative position of a node to a segment, and dL is the infinitesimal line segment. Thus giving individual expressions for node i connected to node j . Using this discretisation and assuming the nodes connected to i are subject to similar conditions, eq. (2.6) can be broken up into local segments,

$$\mathbf{v}_i \approx \left(\sum_j \mathbf{B}_{ij} \right)^{-1} \cdot \mathbf{f}_i, \quad (2.8)$$

where i is the node in question, j are the nodes it shares a segment with, and \mathbf{f}_i is the local force on the node. From now on, we will drop the Einstein notation and refer to the local frame as $\mathbf{v} = \mathbf{B}^{-1} \mathbf{f}$.

The immediate implication of the orders of magnitude difference between the drag coefficients used to construct \mathcal{B} —and therefore \mathbf{B} —means the condition number of $\sum_j \mathbf{B}$ can be very large. As \mathbf{B} is symmetric and therefore normal, its condition number is given by,

$$\kappa(\mathbf{B}) = \frac{|\lambda_{\max}|}{|\lambda_{\min}|}, \quad (2.9)$$

where λ_i is the i^{th} eigenvalue.

The condition number of a matrix dictates how much collinearity exists in its basis. The larger the condition number, the larger the collinearity and the

more sensitive the system is to small perturbations. Such systems are said to be ill-conditioned. As a general rule, a condition number $\kappa(\mathbf{A}) = 10^k$ represents a loss of up to k digits of precision on top of what is already lost from arithmetic methods under limited precision [134].

True to Murphy’s law, \mathbf{B} is frequently ill-conditioned—even in the simplest simulations. The way these cases were handled relied on the integrator reducing the timestep enough to sidestep the issue. We call this “strongly coupled” behaviour. Strong coupling between functionally independent functions is a *very* bad practice in software engineering.

A function \mathcal{X} with a set of \mathbb{X} bugs with phase space $\chi(x)$ that is, $\forall x \in \mathbb{X} \chi(x)$. Bugs in production code are often either low impact with broad phase spaces, or high impact with narrow phase spaces. Both of which can be avoided with a combination of proper software design and testing protocols. All this goes out the window when functions are not properly decoupled. The multiplicative product of the corresponding phase spaces is often non-trivial, and can sometimes cancel out in some cases and blow up in others. Complicating the diagnosis and solution of errors.

The way the mobility functions dealt with ill-conditioned \mathbf{B} , relied on the integrator picking up the slack. There are several flaws with the approach found in algorithm 2.3, the actual mobility function can also be found under commit 65907b0 under the name `mobbcc1.m`. Every mobility law in that commit has this issue.

Algorithm 2.3 Avoiding singular matrix by making \mathbf{B} extremely wrong and hoping the integrator error bounds pick it up and the timestep is decreased.

```

Compute eigenvalue matrix,  $\mathbf{D} \leftarrow \mathbf{P}^{-1}\mathbf{B}\mathbf{P}$ 
 $\kappa(\mathbf{B}) \leftarrow |\lambda_{\max}| / |\lambda_{\min}|$ 
if  $\kappa(\mathbf{B}) < \kappa_{\min}$  then
     $\mathbf{D}_{\text{norm}} \leftarrow \mathbf{D} / \lambda_{\max}$ 
     $\mathbf{f} \leftarrow \mathbf{f} / \lambda_{\max}$                                  $\triangleright$  Invert  $\mathbf{D}_{\text{norm}}$ .
for all  $(\lambda_k \in \mathbf{D}_{\text{norm}}) \neq \lambda_{\max}$  do
    if  $\lambda_k > \lambda_{\text{crit}}$  then
         $\lambda_k \leftarrow 1 / \lambda_k$ 
    else
         $\lambda_k \leftarrow 0$                                  $\triangleright$  The inverse of 0 is not 0.
    end if
end for
 $\mathbf{v} = \mathbf{P}\mathbf{D}\mathbf{P}^{-1}\mathbf{f}$ 
else
     $\mathbf{v} = \mathbf{B}^{-1}\mathbf{f}$ 
end if
```

The first is assuming that an ill-conditioned matrix can be fixed by diagonalising. This is simply not true, perturbing the smallest eigenvalue in a direction such that κ improves is a good way of doing so without adding much error. However, perturbations of this type are often not enough when the condition number is too large. Furthermore, one wants to keep the overall behaviour of the system, i.e. maintain the relative sizes of the eigenvalues with respect to one another. If the multiple eigenvalues are close in magnitude to the smallest eigenvalue, one can change the dynamics of the system if the perturbation is too large. Not to mention the fact that κ may still be too large. In a system as stiff and dynamic as discrete dislocation dynamics, this approach is not enough for some cases.

The second flaw is the assumption that the case where $\lambda_k < \lambda_{\text{crit}}$ for non-maximal eigenvalues, is so rare, it won't have much of an effect. Unfortunately, it's common in junctions where nodal mobility is limited, as well as in volumes with large stress gradients. Although to be fair, these are also consequence of the assumption of locality, yielding section 3.2. Moreover, when every non-maximal eigenvalue is smaller than λ_{crit} , the error much greater. For a every eigenvalue under the threshold of $\lambda_{\text{crit}} = 10^{-k}$, the upper bound of the error is k digits in the corresponding mobility component.

The third is the assumption that the integrator will not allow obviously wrong solutions because it will fail the error check and reduce the time step. This assumption breaks down whenever dislocation velocities are calculated outside the context of time integration, such as every topological operation where a new node is spawned.

The regularisation of ill-conditioned systems is an active field of research [135–137]. However, they require some knowledge of the matrix structure or follow a well-known statistical distribution to thier values/eigenvalues. Regularlisation is most often applied to high rank matrices because poorly conditioned low rank matrices ones are often very sensitive to perturbations, thus requiring specialised methods. In this case, \mathbf{B} is of rank equal to the number of orthogonal crystallographic directions, so it is always of low rank.

One of the most effective regularisations for low rank matrices is dampening the inversion by adding a small value, c —called the Marquardt-Levenberg coefficient—to the diagonal of the matrix. This is roughly equivalent to perturbing the smallest eigenvalue as previously mentioned. Luckily, if this factor is added the whole diagonal, the inversion can be dampened sufficiently whilst keeping the main contributions from each basis roughly equal in relation to each other. This amounts to adding a multiple of the identity matrix to an ill-conditioned matrix. For a more accurate solution, one can iteratively refine c to find the smallest value that keeps the matrix inversion from blowing up. A good heuristic for the value

of the Marquardt-Levenberg coefficient is,

$$c = \max(|\mathbf{A}|) \sqrt{(\epsilon)}, \quad (2.10)$$

where ϵ is machine precision. This ensures the perturbation is scaled to a number that will not underflow during arithmetic operations. Simply put, it ensures the perturbation is small but does not disappear during matrix inversion.

It is worth noting that doing this and inverting is still a source of error, adding noise even if small and along the diagonal, does move the system away from its true behaviour. However, the degree to which it is wrong is many orders of magnitude smaller than what is done in algorithm 2.3. Indeed, algorithm 2.4 uses $\pm c$ and both perturbed solutions are averaged to give a much more accurate and simpler solution even under the traditionally problematic scenarios discussed above. This new algorithm is now present in the mobility laws we now use, such as the most current version of `mobbcc_bb.m`.

Algorithm 2.4 Improved regularisation of \mathbf{B} by way of perturbing the diagonal.

```

if  $\|\mathbf{B}\| < \epsilon$  then
     $\mathbf{v} \leftarrow \mathbf{0}$ 
else if  $|\lambda_{\max}|/|\lambda_{\min}| < \epsilon$  then
     $\mathbf{B}_+ \leftarrow \mathbf{B} + \sqrt{\epsilon} \max(\mathbf{B})$ 
     $\mathbf{B}_- \leftarrow \mathbf{B} - \sqrt{\epsilon} \max(\mathbf{B})$ 
     $\mathbf{v}_+ \leftarrow \mathbf{B}_+^{-1} \mathbf{f}$ 
     $\mathbf{v}_- \leftarrow \mathbf{B}_-^{-1} \mathbf{f}$ 
     $\mathbf{v} \leftarrow (\mathbf{v}_- + \mathbf{v}_+)/2$ 
else
     $\mathbf{v} \leftarrow \mathbf{B}^{-1} \mathbf{f}$ 
end if
```

This change enabled other team members, namely Haiyang Yu and Fengxian Liu to get further with their simulations. Haiyang's nanoindentation simulations have particularly complex dislocation structures with a substantial amount of junction formation; while Fengxian's have large localised stress gradients as a result of inclusions. Both require nodal velocities to be accurately calculated, else the dislocations move erratically, readily cross slip, and cause massive slowdowns as simulations advance.

2.2 Research software engineering

Many scientists and researchers spare no thought for good software. However, with the presently on-going SARS-CoV 2 pandemic, the importance of research software has been made clear. Modelling has played a large role in informing

government policy in the UK and the world [138–140]. With modelling thrust into the spotlight and the public release of the Imperial College modelling code used to inform so much policy [140], <https://github.com/mrc-ide/covid-sim>, criticism was levied at the lack of care taken to ensure the correctness of the code [141]. In experimental research, a lot of care is taken to ensure a methodology used is reproducible, robust and sound. There are standards, both external and internal, which ensure the quality of the results. But even with these measures in place, there is already a common issue with irreproducibility in science [142–144]. In obtaining results and analysing them, software is ubiquitous. It should be good, *especially* if the science is modelling-based.

Along this vein, one of the primary goals of this project was to develop a competent codebase that non-experts can take advantage of with minimal preparation. There were multiple sub-objectives that help us achieve this.

1. Provide a generic framework upon which the software can be modularly expanded with minimal change to the source: prevents increasingly divergent and incompatible source code between researchers.
2. Provide an easy way to autocomplete inputs with sensible default parameters: prevents the software from crashing when—inevitably—one of the required arguments for a function is undefined.
3. Improve readability and organisation: makes it easy to identify, fix bugs and know what the code does.
4. Compartmentalise variables: makes the code more generic and increases usability and readability by reducing the number of function arguments.
5. Optimise memory and computation: improves computational speed and reduces resource use.

Akin to the Ship of Theseus, it is hard to tell whether the new version of the code is the same code as when this project began. While `EasyDD v2.0` is “complete”, the process of improving the code is on-going. The amount of initial technical debt since its inception as the infinite-domain discrete dislocation dynamics code, `DDLab` [129], plus what it accrued as the Tarleton Group expanded its functionality and turned it into `EasyDD`, is quite large and needs to be carefully chipped away so as not to introduce regressions. However, while the quality and capabilities of the code can be greatly improved, there is only so much that can be done without fundamentally redesigning it completely. This is in part the subject of chapter 6.

Other team members have made significant contributions to the release of **EasyDD v2.0**. Some of which remain to be added, but should slowly make their way in. Given the code is the amalgam of the research group’s work, we will credit other members’ contributions where relevant but will leave the details for them to explain.

This is actively evolving on research software. Therefore the work described herein will continue past the end of this project, for there are still many improvements to be made to the old codebase on top of whatever functionality is added by future researchers.

2.2.1 Organisation

An oft-overlooked aspect of code useability is the organisational aspect. However as a codebase grows, it becomes more important for both a code be properly organised and source controlled. This makes it easier to browse, understand, is less overwhelming for users and developers and crucially provides a safety blanket against things going wrong.

2.2.1.1 Source control

Source control is a crucial aspect of industrial software development. It is an industry standard and the first thing to set up when starting a software development project. Academia is very far behind in this regard. Not only does it provide a history of restore points in case things break; but keeps a history of changes, who and when they made them; can perform automated checks such as testing or conflict detection; lets developers and users (if the repository is open-sourced) make changes independently and request their changes be added to the main code; among many other tasks.

In regards to reproducibility, source control is a crucial tool. In both sections 2.1.1 and 2.1.2 we took advantage of this to provide a specific commit and a file name, which lets anyone with access to a repository, the ability to see the entire history of the code. In the digital version of this document, those link commits are links directly to the file—and where relevant—specific lines. The advantages of such a system are obvious. For example, when submitting a manuscript for publication one can also submit a link to the specific version of the software used to obtain the results. This is a gigantic stride towards open, reproducible science.

2.2.1.2 Folder structure

An on-going task is improving the folder structure. Which in the past was almost non-existent. Having a default place to place inputs, outputs and source code is

of great import if a code is to be used by non-experts. It is trivial to do and a boon to the quality of life of developers and users.

2.2.2 Modularisation

Modern software practices usually make heavy use of some form of variable encapsulation and code modularisation to make code safer, simpler to expand and easier to use. This enables users and developers to take advantage of a set of toolboxes that can be chosen according to their needs without having to directly modify the source code, this concept is called “modularisation”.

2.2.2.1 Encapsulation

The act of keeping variables neatly stored in a way that fits a purpose is called encapsulation. By encapsulating variables we greatly improve the usability of software by increasing readability, reducing the risk of human error by reducing the number of things to keep track of, and if done properly can even improve performance. This concept is tightly bound to the design philosophy of software as described in the following list.

- Object-Oriented Programming (OOP): where variables are viewed as objects upon which the logic acts. Functions can take these objects and operate on them. This design pattern keeps related variables as part of a single entity and reduces the number of things users and developers have to keep track of, thus reducing the chance of implementation and user error. There are many advanced concepts and pitfalls in OOP that unnecessarily increase complexity, so it is best to apply the KISS (keep it simple, stupid) approach for best results.
- Data-Driven Programming (DDP): where the data dictates the structure of the programme. It is essentially a modified version of OOP where the object is made to fit the data, not the data made to fit the object. It often leads to more performant code and avoids many of the issues that arise from OOP because it forces developers to really think about how to manage the data.
- Functional programming: where everything is a function. There is no state, but also no side effects. This is the strongest form of encapsulation but also the most inflexible.
- Procedural programming: this is the most ancient form of programming where there are only functions and variables. It is the form most scientific software packages take and it is the most difficult to work with both, as

a developer, user. Even modern computers which can make use of branch prediction and deletion, cache pre-fetching, and compiler optimisations can be hindered by this approach.

Procedural programming is what gives us so-called spaghetti code². Unfortunately, education in programming or software engineering in science is sorely lacking. As a result, a large amount of scientific software tends to be written in this way (particularly legacy software). Thus we strive to separate ourselves from it as much as possible.

Functional programming is impractical for most use cases so it is seldom used outside of computer science and very specific industrial and academic applications [145, 146].

Object-oriented programming can be very useful if used properly. But it has the potential to unnecessarily increase complexity and reduce performance. Fortunately, MATLAB does not truly have object-oriented capabilities, so it forces either a procedural or data-driven approach. Unfortunately once more, it leads to software being written in a procedural manner.

This can be remedied by using `struct` and being sensible about, i.e. by taking a data-driven approach, in building them. While they are more of an ordered dictionary (Hash table), than a true object, they are sufficient for our use-case. They have allowed us to make use of generic functions for different mobility functions, loading conditions, finite element meshes, the dislocation network itself, etc. All of which have a massively simplifying effect on the code without sacrificing performance. While this project pioneered this task, Daniel Hortelano-Roig has been doing much in the way of increasing its scope. His changes greatly simplify the code and will slowly be ported over to the main branch.

2.2.2.2 Generic functions

Generic functions are implementation-agnostic functions that can be given by the user as any other variable. Only the variable in this case is a function. MATLAB has an old method of doing so using `feval()`, where the first argument is the name of the file whose function is being called, and subsequent arguments are passed on to the function. However this has some limitations, mainly their performance, and function handles are now preferred, e.g.

¹ % myFunction is defined in 'myFunction.m' and is called
² % like so myFunction(foo, bar)

²Code with many branches and disparate procedures without a clear purpose. It is difficult to work with as a user and developer. It also tends to interfere with branch prediction and deletion as well as compiler optimisations.

```
3 genericFunction = 'myFunction.m';
4 foo = 1;
5 bar = 2;
6 feval('genericFunction', foo, bar);
```

as opposed to,

```
1 % myFunction is defined in 'myFunction.m' and is called
2 % like so myFunction(foo, bar)
3 genericFunction = @myFunction;
4 foo = 1;
5 bar = 2;
6 genericFunction(foo, bar);
```

which are not dissimilar, but the latter is more performant and easier to follow. Generic functions were already in use for dislocation mobility but there are now ones for calculating numeric and analytic tractions (see chapter 4), loading conditions (multi-stage loading, constant loading, cyclic loading), various post-processing functions, boundary conditions and various miscellaneous functions that support different simulation types.

The main advantage of generic functions is reducing the need for direct source code modification. Changing source code, especially when there are no automated tests to speak of, is a dangerous proposition. It greatly increases the probability of introducing regressions (new bugs) and code divergence between researchers. Regressions are always problematic, but code divergence is a big issue that still affects the Tarleton Group. If experts within the same research group find it difficult to incorporate each others' additions to our work, there is little hope for the general user.

The introduction of regressions makes it so code must be thoroughly and exhaustively tested before merging two people's work. The use of generic functions makes it so if there is a problem with a new addition, the problem is localised and can be quickly identified and fixed because it is isolated. We can be sure the changes are only found in the new piece of code. And since it is generic, we can choose whether or not to use it by changing an input file rather than messing with the source code.

If on the other hand, one were to add a new branch to an `if` statement (or a brand new `if` statement) with new computations, likely the function needs new arguments to cover this new case, we may or may not need to make up- or downstream modifications so the function can accommodate the additions. Then very

quickly we will find ourselves procedurally programming and fixing the inevitable problems that come with hard to understand spaghetti code—which is most likely also less performant now than it used to be. The problem worsens as we add more functionality. Which can all be avoided by intelligently designing a generic approach, that can be easily expanded if the need arises.

2.2.3 Optimisation

We *should* forget about small efficiencies, say about 97% of the time: pre-mature optimization is the root of all evil. Yet we should not pass up our opportunities in that critical 3%.

— Donald E. Knuth [147, p. 268]

2.2.3.1 Spurious memory allocation

MATLAB is infamous for the way it will happily dynamically grow an array when going out of bounds. This *terrible* practice is even fundamental to the operation of EasyDD. However, changing this fundamental part of the codebase requires a complete rewrite and not deemed worthwhile, there are worse bottlenecks. However, there were many instances of memory reallocated or arrays grown every cycle that were completely unnecessary.

For example, the amount of memory unnecessarily reallocated in the function that couples DDD and FEM was $12(N_x + 1)(N_y + 1)(N_z + 1)$ double precision floating point numbers, where N_i is the number of elements in dimension i of the finite domain. The cubic scaling is a performance killer at larger mesh sizes. In a simulation with hundreds or thousands of steps and a mesh with a few thousand FE nodes, the cost added up.

It is not only the cost of allocating, but also the cost of garbage collection [148] i.e. automatically freeing memory based on a set of criteria can be significantly higher. Timing the equivalent of allocating a $20 \times 20 \times 20$ mesh in MATLAB 2020b takes on the order of 70 μ sec (for x86 CPU architectures), which is in-line to what it costs in C. Deallocating memory takes about 5 \times longer. In a function that otherwise takes a few msec, adding another 400 μ sec of spurious allocation is a significant overhead that can be easily remedied.

2.2.3.2 Finite element optimisation

The use of sparse arrays is a must when working with finite elements, where matrices often take structured sparse forms will significantly reduce memory footprint

and computational expense. The code already used these special data structures and Cholesky factorisation for faster solution of linear systems. However, MATLAB has a special form of it that exploits sparsity. This reduced the time required for the factorisation by around $50\times$, reduced the memory footprint of the final sparse arrays by a similar amount, and reduced the memory footprint of the actual factorisation procedure by approximately $10\times$. The whole point of this factorisation is to make solving linear systems faster, in this case the calculation of the corrective displacements, $\hat{\mathbf{u}}$ on the free boundaries, S_U of freedom as a result of the forces acting upon them,

$$\hat{\mathbf{u}} = \mathbf{K}^{-1}\mathbf{f} \quad \text{on } S_U \quad (2.11)$$

It improved solution speed by a factor of 3, thus reducing the cost of coupling DDD to FEM to be dominated by the computation of dislocation-induced tractions and displacements.

The final two optimisations also deal with memory. The first, removes unnecessary allocations in the calculation of the global stiffness matrix and the introduction of a reduced stiffness matrix such that it only includes relevant degrees of freedom.

In aggregate these changes have given us the ability to use $15\times$ more nodes as well as letting us build meshes over two orders of magnitude faster, mostly down to improved memory access patterns inside the mesh building loops.

2.2.4 Misc quality of life improvements

Formerly, initialising a simulation would involve a series of non-obvious steps, particularly when initially compiling the C and CUDA code used for accelerating simulations. This is now done automatically on a need-to-compile basis and has a fallback in case no CUDA compiler is found.

There was also a recurring problem with simulations suddenly failing when a function was called with an undefined argument. This extremely common scenario is unbecoming of good software, especially if the failure happened a few minutes after starting a simulation. This has been remedied with the automatic calculation of a set of reasonable defaults for each and every undefined variable, aside from the arrays defining a dislocation network. Any new developments get added to this very simple, yet much needed script.

2.3 Conclusions

Scientific modelling is inherently an interdisciplinary skill. EasyDD is now faster, more efficient and more capable than ever before, in large part thanks to the work—ongoing or otherwise—described within this chapter. Subsequent chapters explore aspects more specific to discrete dislocation dynamics. However, it is important not to overlook the work that enables the obtention of results. Modern academia deems the final result to be paramount. But what is a result if it cannot be scrutinised because nobody can understand how it came about? Moreover, by developing good software, we allow others to partake in the obtention of results. We deem this to be one of the main contributions of the present project. We feel safe our ability to claim that we now have the capacity for providing more faithful recreations of reality in a less user-unfriendly way. And without so much as a glancing touch on dislocation dynamics.

Chapter 3

Topology improvements

In 2D, dislocations are parametrised as points on a surface. Therefore aside from annihilation, interactions with grain boundaries [115, 116], and perhaps the creation of superdislocations, topological changes in the dislocation network can be mostly ignored. However, in 3D, dislocations are parametrised as lines in a volume. This gives rise to extra complexities that result from multiple dislocations coming into contact with one another. These reactions ultimately lead to the formation of many secondary structures with their own properties that affect the rest of the network.

The local dislocation density at these interaction sites, particularly around sessile (immobile) junctions, tends to increase with time. Therefore so do the local stress gradients, and with increasing stress gradients come increasing velocity gradients, which lead to global decreases in timestep. But a smaller timestep is not the only consequence, increases in dislocation density also mean higher probabilities of dislocation-dislocation interactions, so the phenomenon is autocatalytic and self-perpetuating. So properly accounting for these changes is of the utmost importance, particularly for simulations with high dislocation densities such as nanoindentation. This chapter details these improvements.

3.1 Collision

3.1.1 Hinges

The lowest hanging fruit and most obvious problem were collisions that share a lot of similarities with the remeshing criteria that checks for a minimum area enclosed between two segments connected by a single node, as shown in fig. 3.1. A single dislocation hinge can lead to three different final topologies, the conditions for which can be simultaneously met in any combination

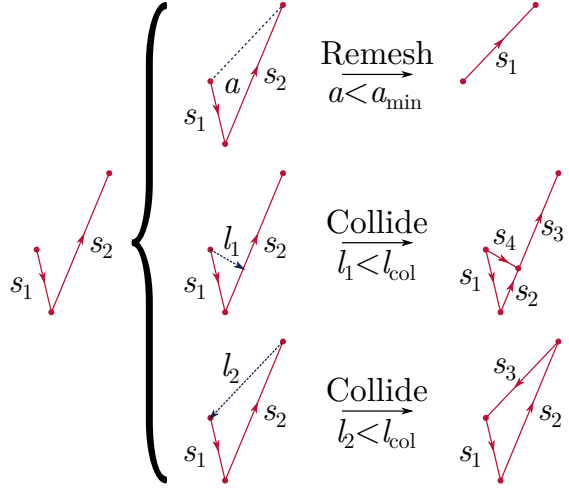


Figure 3.1: A single dislocation hinge can lead to three different final topologies, the conditions for which can be simultaneously met in any combination.

1. Remeshing to eliminate the middle node because the area, a , enclosed by the triangle created by segments s_1 and s_2 is less than the minimum allowable area, a_{\min} .
2. Colliding s_1 into s_2 if the minimum distance between the non-hinge node of s_1 (the node s_1 does not share with s_2) and segment s_2 is less than the collision distance, l_{col} .
3. Colliding s_2 into s_1 if the minimum distance between the non-hinge node of s_2 and segment s_1 is less than the collision distance, l_{col} .

The combination in which these conditions can be met, and the order in which they are checked will have drastic downstream consequences (see section 3.2). *Especially* at high dislocation densities where multiple collisions happen at every timestep. This had not been an issue in prior to fixing the integrator and matrix inversion, but simulations could now advance to a point where this was having a significant impact, particularly in Haiyang Yu's nanoindentation simulations.

This was a multi-stage fix, where each fix progressively uncovered more and more shortcomings resulting from the unavoidable coupling between topological operations. These progressive fixes are detailed in section 3.2 and ???. Here we will only focus on problems with collisions.

The first fix involved prioritising hinge collisions above others, which we call two-line collisions. This meant detecting and forming the new connection. The rationale for this is that segments in a hinge are close enough to and connected with each other at a node already that they will interact more strongly than two unconnected segments approaching one another.

The second was much more subtle. Figure 3.1 has two options for colliding a

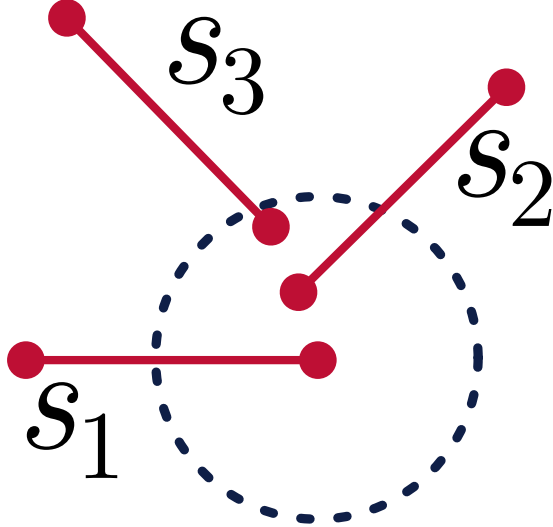


Figure 3.2: Multiple dislocation segments inside the same collision radius.

hinge. And they both result in differently sized segments $l_1 < l_2$. The one the code calculated depended on which segment, s_1 or s_2 it came across. If s_1 was first, then the answer would be l_1 , otherwise it would be l_2 . At the very least, the answer should be the same for a given network regardless of how it is represented. So the first step is to ensure one of these is always chosen, but once this is done it is a simple case of calculating the distance from the short segment to the long one.

Remeshing used to be called after finding a *single* collision. This worked well when the number of collisions at a given time step was small. The problems with this are detailed in section 3.2. But before moving on to that, it became apparent that there was another issue with the collision detection.

3.1.2 Collision distance

In the same vein as section 3.1.1, two-line collisions were being improperly prioritised. They occurred arbitrarily as the code came across them. Again yielding different answers for different representations of the same network. Only this time it had to do with the collision radius as seen in fig. 3.2.

The actual algorithm is more sophisticated because it accounts for both complete segments and finds the two points along them with the minimum distance between each other. But the problem was that as soon as a viable collision was found, the function returned. So in a scenario like fig. 3.2, if the code were looking for a collision on s_1 and it came across s_3 first it would flag that as the collision disregarding the fact that not only was s_2 closer, but s_2 and s_3 are also closer. The same fix had to be applied to hinge collisions.

Despite the fact that checking all possible collisions for the minimum distance

is a more expensive task, it results in faster simulations because the resulting structures are guaranteed to either produce the shortest segments, which can be cleaned up by remeshing, or the highest energy structures which can be cleaned up by separation. Otherwise the structures often end up in a no-man’s land which is energetically unfavourable to separate, or cannot be remeshed; leading to an accumulation of highly immobile, highly energetic structures that cause more and more collisions as simulations advance and create sharp stress gradients that cause the timestep to drop significantly, and preventing simulations from advancing very much after hitting a wall.

3.2 Non-commutativity of topological changes

For a given iteration the time-evolution of the network used to be performed before any topological changes. This was very sub-optimal for a couple of reasons.

The fundamental reason is that by doing so, the time evolution erroneously accounts for complex structures that should have dissipated into lower energy ones as per the quasi-static principle our model is based on. In other words, high energy structures in the network mean large stress gradients. These break the assumption that a node and its neighbours experience similar conditions. These locality assumptions lead to , which is what all our mobility laws based on.

The practical reason is that by leaving these structures around when they should have been removed, the computational complexity increases by virtue of having more nodes and segments that would otherwise not be there.

Moreover, the order in which topological changes were carried out was also very sub-optimal. It used to be the case that separation, collision and remeshing were performed in that order; and collision only detected a single event.

The first step was to ensure all collisions that needed to be performed in a single step were being performed. Unfortunately this quickly revealed the reason why the original version only accounted for a single collision at any given step. It made the terrifyingly-poorly-scaling separation have to separate more high energy structures every time.

The role of separation is to take high energy, highly connected structures and break them apart into lower energy, lower connection ones. Separation is a very poorly scaling operation by itself $\mathcal{O}\left(\sum_i \sum_{j=2}^{\lfloor C_i/2 \rfloor} \frac{C_i!}{(C_i - j)!j!}\right)$. Where the sum over i is done over the nodes with more connections than is allowed; C_i is the number of connections for node i ; and j is the number connections C_i connections can be split into. Mirror symmetries where $2j = C_i$ half the number of possible splitting configurations for that case, but at best this puts the lower bound at approximately

Sterling's factorial formula $N! = \mathcal{O}(N \log N)$. All of these configurations must be generated, which is an $\mathcal{O}(M)$ operation where M are the number of nodes to be added. Unfortunately, this is a relatively expensive operation because the code dynamically expands the relevant arrays. The nodal velocities and segment forces must be calculated for every configuration. Whichever configuration represents the highest energy dissipation is picked as the final configuration. Locality is assumed, so only the forces and mobilities of the segments directly involved are calculated. It is therefore extremely important that the number of separations be kept to a minimum.

The solution was as simple as calling separation after resolving a single collision. This, together with the fixes made to the collision detection, ensured only minimal energy structures were used for subsequent iterations of the collision-separation loop. It also kept the number of possible separations low.

The final pieces of the puzzle were ensuring the network is as clean as possible before running it through the collision-separation loop. This means remeshing the network before to eliminate segments and hinges that need to be remeshed anyway and would only cause problems. And remeshing it after to ensure the next iteration has the cleanest possible network to work with.

3.3 Conclusions

These solved many of the issues with higher densities

Chapter 4

Dislocation-induced surface tractions

Section 4.1 have been adapted from a manuscript prepared for publication. Section 4.2 outlines the work done in parallelising the analytic traction calculation on GPUs.

4.1 Numeric v.s. analytic tractions

4.1.1 Introduction

In-silico experiments are essential for interpreting experimental data and relating the measured mechanical response to dislocation mechanisms [130, 149–151]. Experimentally, we are limited by the electron transparency of the material and our capacity for subjecting samples to representative loads whilst simultaneously keeping dislocations in focus. Modelling, albeit imperfect and idealised, can greatly inform our understanding and provide insight into the dislocation dynamics responsible for our observations.

Simulating micromechanical tests with explicit dislocation interactions necessitates the coupling of discrete dislocation dynamics (DDD) to the finite element method (FEM) [152]. One of the simples and most popular ways of doing so is the superposition method [153–155]. Which works by decomposing the problem into separate DDD and FE problems as illustrated by fig. 4.1.

Specifically, a linear-elastic solid V bounded by a surface S is subjected to traction boundary conditions, \mathbf{T} , on S_T and displacement boundary conditions, \mathbf{U} , on S_U . The (\sim) fields are those generated by the dislocations in an infinite solid and in our case are obtained by evaluating analytic solutions in a DDD simulation

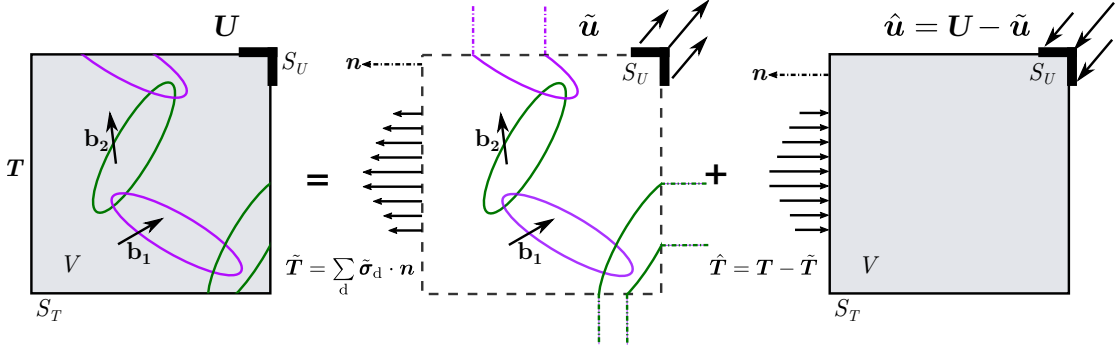


Figure 4.1: The superposition used to couple DDD and FEM. The volume V is bounded by a surface $S = S_T \cup S_U$ and contains a dislocation ensemble and is subjected to tractions \mathbf{T} on S_T and \mathbf{u} on S_U . First, the traction, $\tilde{\mathbf{T}}$, and displacement, $\tilde{\mathbf{u}}$, fields due to the dislocations in the infinite domain (DDD) are evaluated on the boundaries S_T and S_U respectively. Then an elastic boundary value problem can be solved with FEM to calculate the corrective elastic fields required to satisfy the boundary conditions $\hat{\mathbf{T}} = \mathbf{T} - \tilde{\mathbf{T}}$ and $\hat{\mathbf{u}} = \mathbf{U} - \tilde{\mathbf{U}}$.

[101]. Formally, the dislocation field satisfies,

$$\left. \begin{array}{l} \nabla \cdot \tilde{\boldsymbol{\sigma}} = \mathbf{0} \\ \tilde{\boldsymbol{\sigma}} = \mathbf{C} : \tilde{\boldsymbol{\epsilon}} \\ \tilde{\boldsymbol{\epsilon}} = \frac{1}{2} (\nabla \tilde{\mathbf{u}} + (\nabla \tilde{\mathbf{u}})^T) \end{array} \right\} \quad \text{in } V \quad (4.1)$$

$$\tilde{\boldsymbol{\sigma}} \cdot \mathbf{n} = \tilde{\mathbf{T}} \quad \text{on } S_T \quad (4.2)$$

$$\left. \begin{array}{l} \tilde{\mathbf{u}} = \mathbf{U}, \quad t > 0 \\ \tilde{\mathbf{u}} = \mathbf{0}, \quad t = 0 \end{array} \right\} \quad \text{on } S_U. \quad (4.3)$$

As the dislocation fields do not vanish on S , the dislocations load the volume by generating tractions, $\tilde{\mathbf{T}}$, on S_T and displacements, $\tilde{\mathbf{u}}$, on S_U . This additional loading deforms V , generating an additional “image” stress which the dislocations then feel. Therefore corrective ($\hat{\cdot}$) fields must be superimposed to satisfy the desired boundary conditions. The corrective field which accounts for both the applied and image stress is obtained numerically by solving the elastic boundary value problem,

$$\left. \begin{array}{l} \nabla \cdot \hat{\boldsymbol{\sigma}} = \mathbf{0} \\ \hat{\boldsymbol{\sigma}} = \mathbf{C} : \hat{\boldsymbol{\epsilon}} \\ \hat{\boldsymbol{\epsilon}} = \frac{1}{2} (\nabla \hat{\mathbf{u}} + (\nabla \hat{\mathbf{u}})^T) \end{array} \right\} \quad \text{in } V \quad (4.4)$$

$$\hat{\boldsymbol{\sigma}} \cdot \mathbf{n} = \mathbf{T} - \tilde{\mathbf{T}} \quad \text{on } S_T \quad (4.5)$$

$$\hat{\mathbf{u}} = \mathbf{U} - \tilde{\mathbf{u}} \quad \text{on } S_U. \quad (4.6)$$

Once the solutions to both problems are known, their superposition solves the

desired mixed boundary value problem,

$$\left. \begin{aligned} \nabla \cdot \boldsymbol{\sigma} &= \nabla \cdot (\hat{\boldsymbol{\sigma}} + \tilde{\boldsymbol{\sigma}}) = \mathbf{0} \\ \boldsymbol{\sigma} &= \hat{\boldsymbol{\sigma}} + \tilde{\boldsymbol{\sigma}} = \mathbf{C} : (\hat{\boldsymbol{\epsilon}} + \tilde{\boldsymbol{\epsilon}}) = \mathbf{C} : \boldsymbol{\epsilon} \\ \boldsymbol{\epsilon} &= \hat{\boldsymbol{\epsilon}} + \tilde{\boldsymbol{\epsilon}} = \frac{1}{2} \left(\nabla(\hat{\mathbf{u}} + \tilde{\mathbf{u}}) + [\nabla(\hat{\mathbf{u}} + \tilde{\mathbf{u}})]^T \right) = \frac{1}{2} \left(\nabla \mathbf{u} + (\nabla \mathbf{u})^T \right) \end{aligned} \right\} \quad \text{in } V \quad (4.7)$$

$$\boldsymbol{\sigma} \cdot \mathbf{n} = \mathbf{T} \quad \text{on } S_T \quad (4.8)$$

$$\left. \begin{aligned} \mathbf{u} &= \mathbf{U}, \quad t > 0 \\ \mathbf{u} &= \mathbf{0}, \quad t = 0 \end{aligned} \right\} \quad \text{on } S_U \quad (4.9)$$

For all its simplicity and elegance, the method is not without issue. As the distance between dislocation and surface decreases, $\tilde{\boldsymbol{\sigma}}$ diverges [156]. This can be partially solved by using a non-singular formulation for $\tilde{\boldsymbol{\sigma}}$, such as that proposed by Cai et al. [101]. Regardless, the steep gradients in the dislocation field are difficult to accurately capture as the dislocation approaches S . Another problem with this method is the large computational cost when simulating a heterogeneous solid, as this requires calculating polarisation stresses due to the difference in the elastic constants between phases [153, 156, 157].

A modified superposition scheme [158] can overcome this by dividing the problem into separate DDD-FEM problems coupled through a elastic FE problem. This requires accurate evaluation of $\tilde{\mathbf{T}}$ on the domain boundaries—which can only be captured with a fine FE mesh—increasing the computational cost. Therefore, simulating polycrystalline or composite materials using superposition necessitates methods to accurately evaluate both $\tilde{\mathbf{u}}$ and $\tilde{\mathbf{T}}$. The displacements can be evaluated analytically as shown by [133] and this paper investigates the evaluation of the dislocation tractions analytically.

As previously mentioned, the relative simplicity of the superposition method has made it a popular choice for coupling DDD and FEM as all it needs is the evaluation of FE nodal forces and displacements on the boundary. Furthermore, the analytic expression for the stress field produced by a finite, straight dislocation line segment has allowed Queyreau et al. [86] to use the non-singular formulation [101] to obtain closed-form solutions for the tractions generated by the segment on the surface of a finite element.

4.1.2 Theory

The force exerted by a dislocation ensemble on a node, a , belonging to element, e , is given by,

$$\mathbf{F}_a = \int_{S_e} [\tilde{\boldsymbol{\sigma}}(\mathbf{x}) \cdot \mathbf{n}] N_a(\mathbf{x}) \, dS_e. \quad (4.10)$$

Where dS_e is the surface of element e with surface area S_e , and N_a is the finite element shape function for node a . The solutions are for linear rectangular surface elements and as such the shape functions are,

$$\begin{aligned} N_1 &= \frac{1}{4}(1 - s_1)(1 - s_2) \\ N_2 &= \frac{1}{4}(1 + s_1)(1 - s_2) \\ N_3 &= \frac{1}{4}(1 + s_1)(1 + s_2) \\ N_4 &= \frac{1}{4}(1 - s_1)(1 + s_2). \end{aligned} \quad (4.11)$$

Where s_1 and s_2 are the orthogonal coordinates local to the element.

Gauss quadrature is usually used to numerically evaluate the surface integral in eq. (4.10). In 1D this is,

$$\int_{-1}^1 f(s) \, ds \approx \sum_{i=1}^n w_i f(s_i) \quad \text{where} \quad w_i = \frac{2}{(1 - s_i^2) [P'_n(s_i)]^2}, \quad (4.12)$$

is the weighting of the Gauss point, s_i , which is the i^{th} root of the n^{th} normalised Legendre polynomial, $P_n(1) = 1$. P'_n is the first order derivative of P_n . This method is very accurate for functions that can be accurately approximated by polynomials. In fact, for a polynomial of degree n , one needs $n - 1$ points to obtain an exact numerical solution. However, this quadrature is well-known for being unsuitable for integrating functions with poles or near-poles [159, 160].

We avoid the strict pole in $\tilde{\sigma}$ by using the non-singular formulation described in [101], where the true singularity is avoided by adding a small cut-off radius to account for the dislocation core. However, if an integration point falls close to, or within the dislocation core, Gauss quadrature can still produce large errors.

For rectangular surface elements, we must transform from the parent element in (s_1, s_2) in eq. (4.12) to the real element coordinate system (x, y, z) . Evaluating eq. (4.10) in the parent element and mapping to the real element gives the force on node a ,

$$\mathbf{F}_a \approx \sum_{i=1}^Q w_i \sum_{j=1}^Q w_j [\tilde{\sigma}(r_i, s_j) \cdot \mathbf{n}] N_a(r_i, s_j) \det(\mathbf{J}). \quad (4.13)$$

Where the sum is over the Q quadrature points and $J_{ij} = dx_i/ds_j$, is the element Jacobian defining the transformation from $(s_1, s_2) \mapsto (x, y)$. Since the real element is rectangular with surface area S_e , then $\det(\mathbf{J}) = S_e/4$. Figure 4.2 contains examples of how the Gauss points are distributed on the surface.

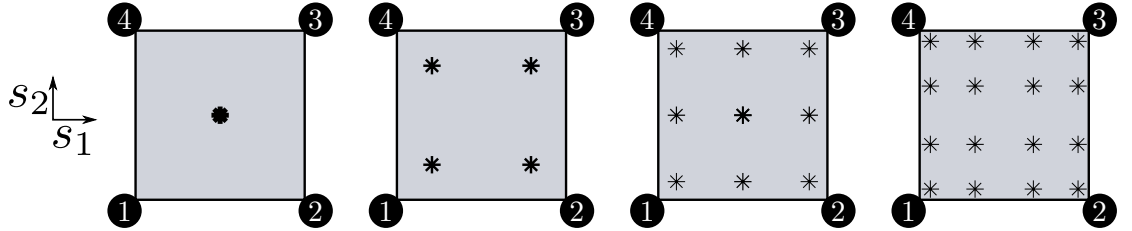


Figure 4.2: Examples of 2D Gauss-Legendre quadrature of the parent element with $Q = 1, 2, 3, 4$. The point size represents the weight w of the integration point. The parent elements are centred at the origin and $s_1, s_2 \in [-1, 1]$. We use an anticlockwise node numbering scheme.

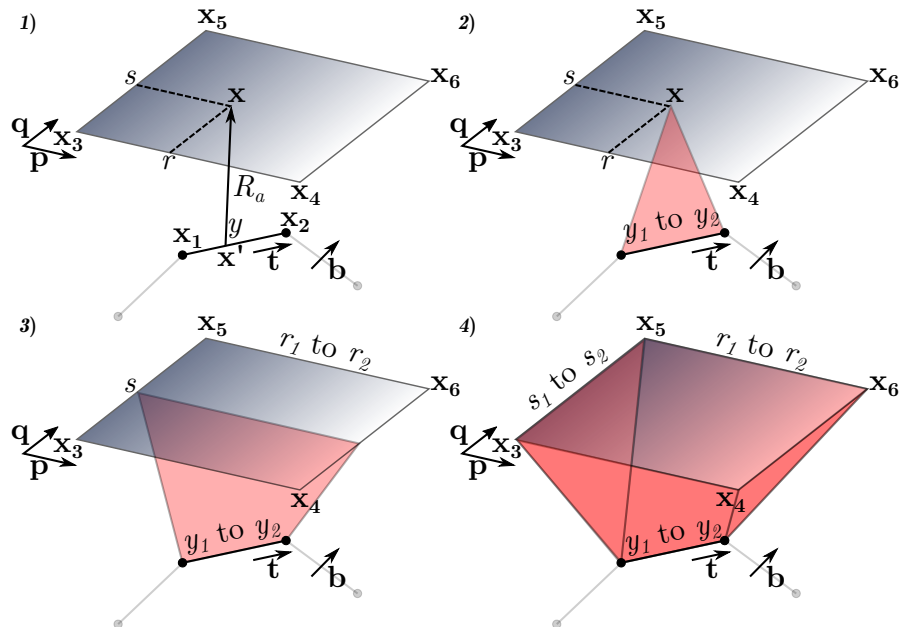


Figure 4.3: Diagram of the parametric line integrals solved by Queyreau et al. [86] to find the forces on linear rectangular surface elements.

Explicitly, eq. (4.10) is actually a triple vector integral as shown in fig. 4.3. This is because given the isotropic Burgers vector distribution proposed in [101], the dyadic form of the stress tensor produced by a straight, finite dislocation segment bounded by nodes at \mathbf{x}_1 and \mathbf{x}_2 [86] is,

$$\begin{aligned}\tilde{\boldsymbol{\sigma}}(\mathbf{x}) = & -\frac{\mu}{8\pi} \int_{\mathbf{x}_1}^{\mathbf{x}_2} \left(\frac{2}{R_a^3} + \frac{3a^2}{R_a^5} \right) [(\mathbf{R} \times \mathbf{b}) \otimes d\mathbf{x}' + d\mathbf{x}' \otimes (\mathbf{R} \times \mathbf{b})] \\ & + \frac{\mu}{4\pi(1-\nu)} \int_{\mathbf{x}_1}^{\mathbf{x}_2} \left(\frac{1}{R_a^3} + \frac{3a^2}{R_a^5} \right) [(\mathbf{R} \times \mathbf{b}) \cdot d\mathbf{x}'] \mathbf{I}_2 \\ & - \frac{\mu}{4\pi(1-\nu)} \int_{\mathbf{x}_1}^{\mathbf{x}_2} \frac{1}{R_a^3} [(\mathbf{b} \times d\mathbf{x}') \otimes \mathbf{R} + \mathbf{R} \otimes (\mathbf{b} \times d\mathbf{x}')] \\ & + \frac{\mu}{4\pi(1-\nu)} \int_{\mathbf{x}_1}^{\mathbf{x}_2} \frac{3}{R_a^5} [(\mathbf{R} \times \mathbf{b}) \cdot d\mathbf{x}'] \mathbf{R} \otimes \mathbf{R},\end{aligned}\quad (4.14)$$

where,

$$\mathbf{R} = \mathbf{x} - \mathbf{x}' = y\mathbf{l} + r\mathbf{p} + s\mathbf{q} \quad (4.15)$$

$$R_a = \sqrt{\mathbf{R} \cdot \mathbf{R} + a^2} \quad (4.16)$$

$$d\mathbf{x}' = -dy\mathbf{l}. \quad (4.17)$$

The vectors \mathbf{p} and \mathbf{q} are aligned with the edges of the rectangular finite element, $\mathbf{n} = \mathbf{p} \times \mathbf{q}$ is the element surface normal (pointing away from the dislocation), and \mathbf{l} is parallel to the dislocation line segment as shown in fig. 4.3. Then (provided \mathbf{l} is not parallel to \mathbf{p} or \mathbf{q}) \mathbf{R} can be expressed in terms of $(\mathbf{l}, \mathbf{p}, \mathbf{q})$ with coefficients,

$$y = \frac{\mathbf{R} \cdot \mathbf{n}}{\mathbf{l} \cdot \mathbf{n}}, \quad r = \frac{\mathbf{R} \cdot (\mathbf{q} \times \mathbf{l})}{\mathbf{p} \cdot (\mathbf{q} \times \mathbf{l})}, \quad s = \frac{\mathbf{R} \cdot (\mathbf{p} \times \mathbf{l})}{\mathbf{q} \cdot (\mathbf{p} \times \mathbf{l})}. \quad (4.18)$$

Substituting eq. (4.14) and eq. (4.11) into eq. (4.10) yields four long and messy equations (one for each FE node) that were elegantly solved by Queyreau et al. [86] by utilising the fact that the triple integrals all had the form,

$$H_{ijkl} = \int_{r_1}^{r_2} \int_{s_1}^{s_2} \int_{y_1}^{y_2} \frac{r^i s^j y^k}{R_a^m} \quad (4.19)$$

$$\begin{aligned}& \text{when } m = 5 \text{ then } i, j \in [0, 3], k \in [0, 2] \\& \text{when } m = 3 \text{ then } i, j \in [0, 2], k \in [0, 1] \\& \text{when } m = 1 \text{ then } i = j = k = 0.\end{aligned}\quad (4.20)$$

Using partial differentiation and integration by parts, they found a series of recurrence relations that lead to double and single integrals of similar form to eq. (4.19). All of which are used to construct a full, exact solution. The recurrence relations stop working when $i = j = k = 0$ and $m = 1, 3$. At which point, direct integration of the remaining single and double integrals (the last triple integrals all cancel out in the global calculation) yields six seed functions that are used as the starting point for the recurrence relations. Three of them are logarithms and three either arctangents or—if a discriminant is negative—hyperbolic arctangents. The details of the procedure can be found in [86].

Although exact, the use of arctangents, hyperbolic arctangents and logarithmic functions, compounded by the large number of recurrence relations is prime territory for error propagation and numerical problems (see section 4.1.3). The problem is particularly egregious when using general purpose compilers instead of high-performance or scientific computing compilers where mathematical functions are implemented more precisely. Such issues must be taken into account when using analytic tractions, which can be done by using numerical tolerances as described in section 4.1.3.

In simulations, tractions are manifested as image stresses calculated by the FE solver at FE nodes. In order to validate and compare the practical differences between analytic and numeric methods, we compare the resulting image stresses from both methods to the analytic expressions for infinite dislocations in inhomogenous media for edge dislocations [161], as well as those for screw dislocations [162, p. 59, 64]. We keep the same nomenclature and coordinate system as both infinite-domain solutions. Where the traction surface is the line $x = 0$, the dislocation line direction is the positive z -direction (pointing out of the page), the dislocation coordinates are represented by (a, c) , and points in the xy -plane described by their (x, y) coordinates.

The original paper by Head [161] has a few typos that have been replicated in other sources. We therefore include the complete and correct expressions in eqs. (4.21) to (4.23). Head [161] gives two basic cases. Equation (4.21) corresponds to the case where \mathbf{b} is perpendicular to the surface and positive b means it points

in the positive x -direction,

$$\sigma_{xx} = D(y - c) \left\{ -\frac{3(x - a)^2 + (y - c)^2}{[(x - a)^2 + (y - c)^2]^2} + \frac{3(x + a)^2 + (y - c)^2}{[(x + a)^2 + (y - c)^2]^2} + 4ax \frac{3(x + a)^2 - (y - c)^2}{[(x + a)^2 + (y - c)^2]^3} \right\}, \quad (4.21a)$$

$$\sigma_{yy} = D(y - c) \left\{ \frac{(x - a)^2 - (y - c)^2}{[(x - a)^2 + (y - c)^2]^2} - \frac{(x + a)^2 - (y - c)^2}{[(x + a)^2 + (y - c)^2]^2} + 4a(2a - x) \frac{(x + a)^2 + (3x + 2a)(y - c)^2}{[(x + a)^2 + (y - c)^2]^3} \right\}, \quad (4.21b)$$

$$\begin{aligned} \sigma_{xy} &= D \left\{ (x - a) \frac{(x - a)^2 - (y - c)^2}{[(x - a)^2 + (y - c)^2]^2} - (x + a) \frac{(x + a)^2 - (y - c)^2}{[(x + a)^2 + (y - c)^2]^2} \right. \\ &\quad \left. + 2a \frac{6x(x + a)(y - c)^2 - (x - a)(x + a)^3 - (y - c)^4}{[(x + a)^2 + (y - c)^2]^3} \right\}. \end{aligned} \quad (4.21c)$$

Equation (4.22) corresponds to the case where the \mathbf{b} lies parallel to the surface and positive b means it points in the positive y -direction,

$$\begin{aligned} \sigma_{xx} &= D \left\{ (x - a) \frac{(x - a)^2 - (y - c)^2}{[(x - a)^2 + (y - c)^2]^2} - (x + a) \frac{(x + a)^2 - (y - c)^2}{[(x + a)^2 + (y - c)^2]^2} \right. \\ &\quad \left. + 2a \frac{(3x + a)(x + a)^3 - 6x(x + a)(y - c)^2 - (y - c)^4}{[(x + a)^2 + (y - c)^2]^3} \right\}, \end{aligned} \quad (4.22a)$$

$$\begin{aligned} \sigma_{yy} &= D \left\{ (x - a) \frac{(x - a)^2 + 3(y - c)^2}{[(x - a)^2 + (y - c)^2]^2} - (x + a) \frac{(x + a)^2 + 3(y - c)^2}{[(x + a)^2 + (y - c)^2]^2} \right. \\ &\quad \left. - 2a \frac{(x - a)(x + a)^3 - 6x(x + a)(y - c)^2 + (y - c)^4}{[(x + a)^2 + (y - c)^2]^3} \right\}, \end{aligned} \quad (4.22b)$$

$$\begin{aligned} \sigma_{xy} &= D(y - c) \left\{ \frac{(x - a)^2 - (y - c)^2}{[(x - a)^2 + (y - c)^2]^2} - \frac{(x + a)^2 - (y - c)^2}{[(x + a)^2 + (y - c)^2]^2} \right. \\ &\quad \left. + 4ax \frac{3(x + a)^2 - (y - c)^2}{[(x + a)^2 + (y - c)^2]^3} \right\}. \end{aligned} \quad (4.22c)$$

Equation (4.23) corresponds to screw dislocations, which are markedly simpler as only the shear components are non-zero. Here $\mathbf{b} = \mathbf{l}$ so positive b means it points in the positive z -direction,

$$\sigma_{xz} = -D \left(\frac{y - c}{(x - a)^2 + (y - c)^2} - \frac{y - c}{(x + a)^2 + (y - c)^2} \right) \quad (4.23a)$$

$$\sigma_{yz} = D \left(\frac{x - a}{(x - a)^2 + (y - c)^2} - \frac{x + a}{(x + a)^2 + (y - c)^2} \right). \quad (4.23b)$$

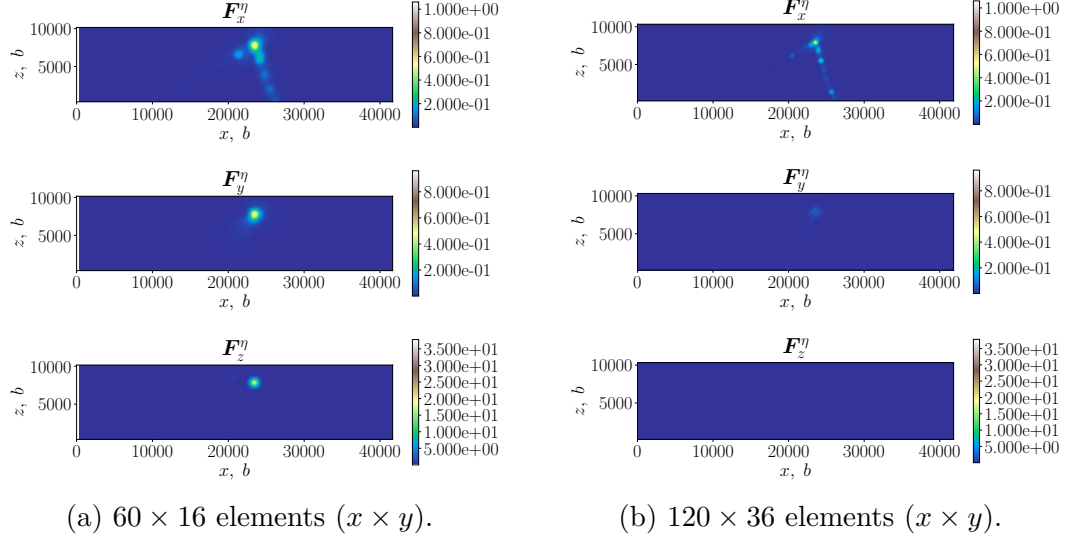


Figure 4.4: Relative error (\mathbf{F}^η) in the nodal force obtained using numerical integration with one quadrature point $Q = 1$, and the analytic solution. The xz -face of a rectangular cantilever with plane normal, $\mathbf{n} = [0\bar{1}0]$. The dislocation is of pure edge character with $\mathbf{b} = [10\bar{1}]$, and line direction, $\mathbf{l} = [\bar{1}2\bar{1}]/\sqrt{6}$ which pierces both xz -faces. The dislocation has its centre at the centroid of the cantilever.

In every case, the constant D is defined by eq. (4.24),

$$D = \frac{\mu}{2\pi} \cdot \frac{1+\nu}{1-\nu^2} \cdot b. \quad (4.24)$$

Note the first terms of eqs. (4.21) to (4.23) all correspond to the stress field generated by the dislocation itself. The following terms are the corrective terms required to make the boundary conditions on the surface equal to zero. Therefore, we can split these equations and only look at the real or corrective terms independently, which we do in order to only visualise the effect of the different traction calculations. Furthermore, eqs. (4.21) to (4.23) are all singular at the dislocation coordinates. Our simulation code uses the non singular expressions found by Cai et al. [101], which smooth out drastic increases in stresses and avoid numerical blow up as we near the dislocation core.

4.1.3 Methodology

Numerical integration of tractions can produce unexpected behaviour such as force hot spots and sign inversions as a dislocation approaches a surface. During a large simulation, these effects are hard to spot. Figure 4.4 has a quick example of the relative errors for an idealised system not dissimilar to what can be found within a simple cantilever bending simulation with a single dislocation loop. As expected, the errors decrease as the mesh gets finer.

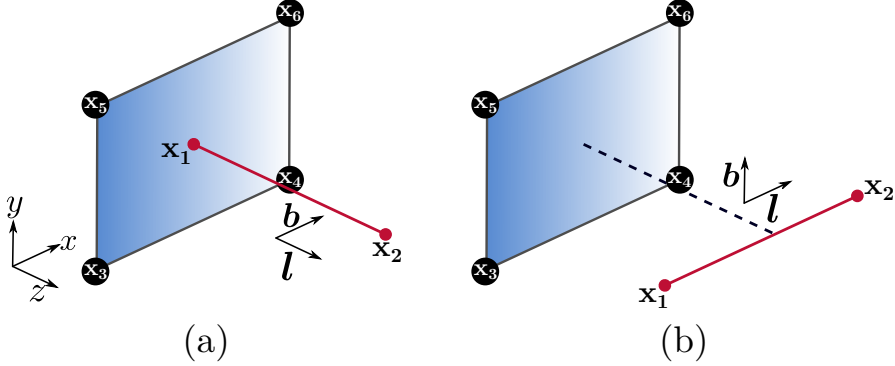


Figure 4.5: Simple test cases for an edge segment and surface element perpendicular (a) and parallel (b). The perpendicular dislocation is centered at the midpoint of the surface element, node \mathbf{x}_1 is separated by a perpendicular distance \mathbf{x}_1^z to prevent the dislocation from intersecting the surface. On the right, the parallel dislocation runs along the x -axis at half the height of the surface element. The nodes of each dislocation line segment are kept at a perpendicular distance of at least one core radius away from the surface element.

Queyreau et al. [86] identified that for a given number of quadrature points, the error is dependent on the dislocation character but always increases rapidly as the distance between the segment and element surface decrease (see figs. 4.9 and 4.10).

Expanding the test cases reveals just how problematic numerical integration of the tractions can be when a dislocation approaches a surface. The two basic test cases, an orthogonal and parallel edge segment, are shown in fig. 4.5.

The symmetry of these simple test cases benefits the accuracy of the numerical solutions because the stress fields exhibit symmetries about the dislocation line. If under ideal conditions for error cancellation, it can be proven that the numerical method is inferior to the analytic one, it can be more effectively argued that the analytic one should always be used instead.

Queyreau et al. [86] found the analytic solution is approximately 10 times more computationally expensive than its numerical counterpart for 1 quadrature point, our findings agree with this result but the implications for a whole simulation are favourable (see section 4.1.4).

One serious disadvantage of the analytic tractions is that the implementation of the analytic solution is also much more involved and full of snags. One issue is the calculation of the y -coordinate in the local coordinate frame as shown in fig. 4.3 and eq. (4.18). If $\mathbf{l} \perp \mathbf{n}$, we get a singularity. As mentioned in [86], an easy fix is to rotate the line segment. We do this about its midpoint and around the $\mathbf{l} \times \mathbf{n}$ axis in both clockwise and anticlockwise directions. We use the mean of the values as the answer for $\theta = 0$. An example of what this rotation looks like in terms of the forces on a surface element can be seen in fig. 4.6 (avoiding the

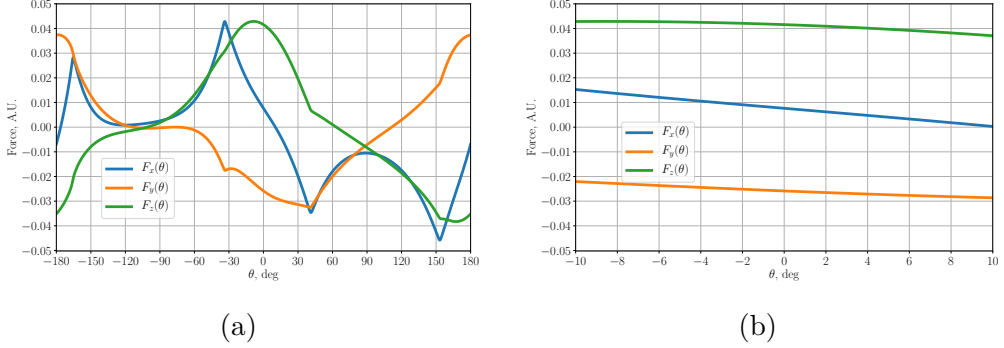


Figure 4.6: (a) Example of the components of the total force on a surface element (the force summed over all four FE nodes) as a dislocation segment parallel to the surface element ($\theta = 0$) is rotated about its midpoint around the axis defined by $\mathbf{l} \times \mathbf{n}$. (b) is zooms into ± 10 deg, the force is smooth but not necessarily antisymmetric about the neighbourhood of $\theta = 0$.

singularity at $\theta = 0$). The specific shape of the curves will vary depending on the element-segment configuration, but is smooth and well-behaved about singularity. For our purposes, we use a total of 8 perturbations of 1 deg each (4 clockwise and 4 anti-clockwise). We found this worked well, but can be changed if desired.

However, under finite-precision arithmetic, the check for orthogonality is dependent on the length scales involved in the simulation. This is particularly important considering the aforementioned use of arctangents, hyperbolic arctangents, logarithms and the large number of recurrence relations. Causing unexpected and rampant error propagation and numerical blow up is not difficult to achieve. When it happens, finding the root cause can lead one on a wild goose chase that is best avoided and often leads to a single segment in a single step of a long simulation that is slightly too small compared to its distance to a surface element to which it is slightly too parallel. To avoid these rare but high impact scenarios, we created a heuristic that dictates how strict the tolerance should be in order for the code to consider a segment to be parallel,

$$|\mathbf{l} \cdot \mathbf{n}| \lesssim \frac{\max(|\mathbf{R} \cdot \mathbf{n}|)}{10^8}. \quad (4.25)$$

In our case the numerator on the RHS is simply the FEM domain's largest dimension. 10^8 is used instead of actual machine precision $\sim 10^{15}$ because the seed functions and large number of recurrence relations of the solution propagate errors if the value of $\mathbf{l} \cdot \mathbf{n}$ is too close to zero. Ironically, tolerances which are too large can cause the perturbations to rotate the dislocation segment closer to the singularity, producing erroneous results. Larger than necessary tolerances can also slow down the calculation by detecting dislocations that are far enough from the special case that they can be treated like non-parallel segments. This heuristic is

a good general purpose rule that keeps the tolerance in a goldilocks zone.

Another issue with the rotation is that one does not want a dislocation segment to intersect the surface when it is being rotated. Naively one would calculate the maximum rotational angle, θ_{\max} , to be,

$$\theta_{\max} = \arctan \left(\frac{2d}{|\mathbf{x}_2 - \mathbf{x}_1|} \right). \quad (4.26)$$

Where d is the minimum orthogonal distance from the dislocation to the surface element i.e. the collision distance—which in our case is a function of the dislocation core radius—and \mathbf{x}_1 , \mathbf{x}_2 are the dislocation segment node coordinates—whose maximum and minimum lengths are also functions of the dislocation core radius. However, θ_{\max} might be too small in cases where the segment length is too small compared to the distance to a surface element, or when the segment length is much greater than d . Fine-tuning the angle is a task that involves knowing the minimum collision distance, minimum segment length, dislocation core radius, and the compiler’s implementation of mathematical functions. Given the rarity of such cases and their comparatively low impact, we chose our 1 deg perturbation such that we safely avoid this problem while keeping within the bounds of the non-singular model.

Furthermore, the chirality and self-consistency of the FE nodes must be accounted for such that they are in the proper order regardless of the element face they belong to. Here we use 8-node linear hexahedral (brick) elements. The node ordering for the various surfaces is that for which the calculated normals point out from the domain, this is dependant on the specific FE mesh implementation.

The total force on a given node must include the force contributions from every element in which said node appears, see fig. 4.7. The specifics of the mapping depend on the global FE node numbering. Using fig. 4.7 as our reference labels for elements and nodes, e and n respectively, we can give a concrete example of

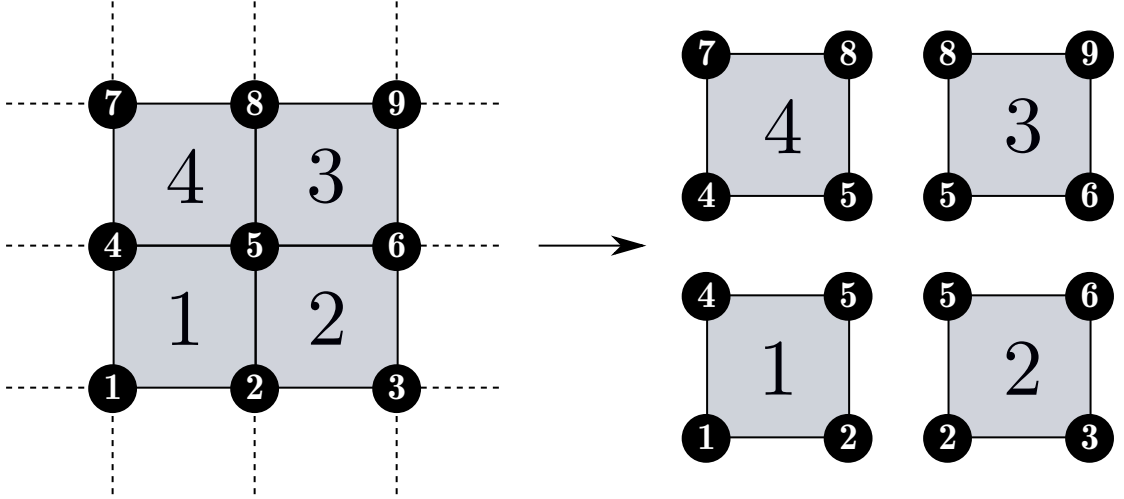


Figure 4.7: FE nodes are shared by either 4 element faces or 3 if it is a corner node. The total force on a given node is the summation of the force contributions from each element it belongs to.

how this is done by defining,

$$\mathbf{x}_{e,n} \equiv [x_{e,n} \ y_{e,n} \ z_{e,n}]^T, \quad \mathbf{x}_n \equiv [x_n \ y_n \ z_n]^T \quad (4.27a)$$

$$\mathbf{N}_L = \begin{bmatrix} l_{1,1} & l_{1,2} & l_{1,4} & l_{1,5} \\ l_{2,2} & l_{2,3} & l_{2,5} & l_{2,6} \\ l_{3,5} & l_{3,6} & l_{3,8} & l_{3,9} \\ l_{4,4} & l_{4,5} & l_{4,7} & l_{4,8} \end{bmatrix}, \quad \boldsymbol{\gamma} = \begin{bmatrix} l_1 \\ l_2 \\ \vdots \\ l_9 \end{bmatrix} \quad (4.27b)$$

$$\mathbf{F}_e = \begin{bmatrix} \mathbf{x}_{1,1} & \mathbf{x}_{1,2} & \mathbf{x}_{1,4} & \mathbf{x}_{1,5} \\ \mathbf{x}_{2,2} & \mathbf{x}_{2,3} & \mathbf{x}_{2,5} & \mathbf{x}_{2,6} \\ \mathbf{x}_{3,5} & \mathbf{x}_{3,6} & \mathbf{x}_{3,8} & \mathbf{x}_{3,9} \\ \mathbf{x}_{4,4} & \mathbf{x}_{4,5} & \mathbf{x}_{4,7} & \mathbf{x}_{4,8} \end{bmatrix}, \quad \tilde{\mathbf{F}} = \begin{bmatrix} \mathbf{x}_1 \\ \mathbf{x}_2 \\ \vdots \\ \mathbf{x}_9 \end{bmatrix}. \quad (4.27c)$$

Where $\mathbf{x}_{e,n}$ is a 3×1 column vector corresponding to the (x, y, z) dislocation induced forces on node, n , on the surface element, e . There are four of these per rectangular surface element, where a given node, n , can appear in multiple surface elements (e.g. node 5 in fig. 4.7 is shared by all 4 surface elements), all of which independently contribute to the total force on said node. \mathbf{x}_n is a 3×1 column vector corresponding to the total (x, y, z) dislocation induced forces on node n . These are used to shorten the definition of eq. (4.27c) and are not explicitly defined in the implementation, rather they give the force matrices \mathbf{F}_e and $\tilde{\mathbf{F}}$ a specific row order. \mathbf{N}_L is crucial for the correct implementation of this analytical solution in traditional FE codes. It is the $E \times 4$ matrix corresponding to the global label of each node in a given surface element. Each row of the matrix represents a surface element and each column represents a node in the surface element. We cannot

naïvely add the columns together as that would give the total force acting on the element as a whole, not each FE node individually. We chose to arrange the columns in accordance to fig. 4.3 as it makes it easier to implement the solution, but the only thing that matters is that the basis vectors \mathbf{n} , \mathbf{p} , \mathbf{q} are calculated appropriately. $\boldsymbol{\gamma}$ is the vector with the FE node labels, which makes mapping force to node possible. \mathbf{F}_e is the $3E \times 4$ matrix where the forces acting on each of the four nodes (column) in a particular surface element (each element corresponds to three consecutive rows because there are three dimensions) are stored. $\tilde{\mathbf{F}}$ is the $3N \times 1$ column vector where the total forces on each node are stored (each node has three rows because there are three dimensions). This is easily generalisable to E elements and N nodes.

Algorithm 4.1 illustrates how the total force on each node is obtained. However, our implementation does not strictly follow it because we memoise a generalised version of \mathbf{L} upon simulation initialisation instead of finding one at every iteration, reducing computational time but requiring us to account for nodes without traction boundary conditions. Our indexing also starts at 1, but zero indexing makes the algorithm easier to follow.

Algorithm 4.1 Assuming $\tilde{\mathbf{F}}$ is arranged the same way as γ and indexing starts at 0.

- ```

1: ▷ Loop through the array containing the node labels of the relevant surface
nodes.
2: for $i = 0; i < \text{length}(\gamma); i++ \text{ do}$
3: ▷ Save the global node label for the current iteration.
4: $n \leftarrow \gamma[i]$
5: ▷ Use the node label to find a vector, \mathbf{L} , with the linearised indices
in \mathbf{N}_L where node n appears as part of a surface element whose tractions we
are calculating.
6: $\mathbf{L} \leftarrow \text{find}(\mathbf{N}_L == n)$
7: ▷ Loop over coordinates.
8: for $k = 0; k < 3; k++ \text{ do}$
9: ▷ Use global node label vector to index the force
array from the analytical force calculation. Multiplied by 3 because there are
three coordinates per node. We sum the forces from the analytical calculation
because the same global node can be part of multiple surface elements. We
add k because the x, y, z coordinates are consecutively stored in \mathbf{F}_e .
10: $\tilde{\mathbf{F}}[3n + k] \leftarrow \tilde{\mathbf{F}}[3n + k] + \sum \mathbf{F}_e[3\mathbf{L} + k]$
11: end for
12: end for

```

The resulting force vector is then used in eq. (4.5) to calculate  $\hat{\sigma}$ , since  $\tilde{\mathbf{T}} \equiv \tilde{\mathbf{F}}$ . Figure 4.8 shows the simple system we used to compare the image stresses calculated by our FE solver using numeric tractions v.s. analytic tractions v.s.

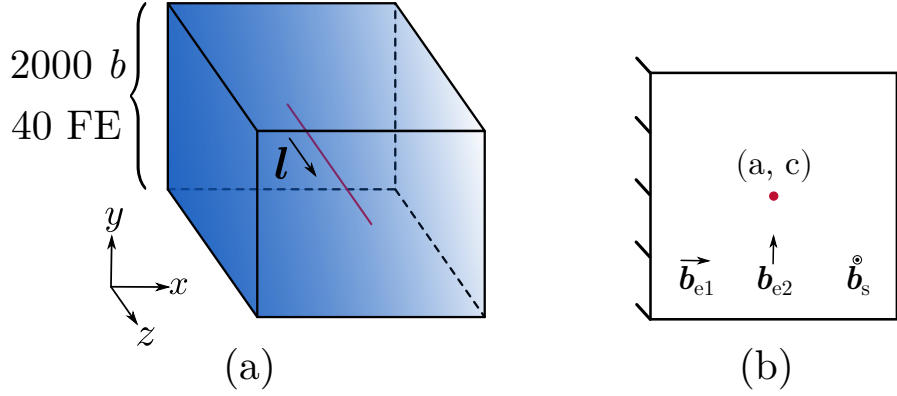


Figure 4.8: Dislocation parallel to a surface described by the line  $x = 0$ , where the  $(x, y)$  dislocation coordinates are  $(a, c)$  and the dislocation line going in the positive  $z$ -direction. (a) describes the box we used for our comparison, a  $40 \times 40 \times 40$  element cubic box with side lengths equal to 2000 with  $\mathbf{T} = \mathbf{0}$ , traction boundary conditions only on the nodes along  $x = 0$ , and  $\mathbf{U} = \mathbf{0}$ , displacement conditions everywhere else. (b) is the 2D view with the dislocation coordinates  $(a, c)$ , as well as the two edge Burgers vectors in [161],  $\mathbf{b}_{e1} \equiv \mathbf{b} = [1\ 0\ 0]$ ,  $\mathbf{b}_{e2} \equiv \mathbf{b} = [0\ 1\ 0]$  and the screw Burgers vector  $\mathbf{b}_s \equiv \mathbf{b} = \mathbf{l} = [0\ 0\ 1]$  in [162, p. 59, 64].

infinite-domain, singular image stresses in eqs. (4.21) to (4.23). The three test cases are: two edge dislocations and one screw, all of which have line direction  $\mathbf{l} = [0\ 0\ 1]$ . The Burgers vectors for the different scenarios are  $\mathbf{b}_{e1} \equiv \mathbf{b} = [1\ 0\ 0]$ ,  $\mathbf{b}_{e2} \equiv \mathbf{b} = [0\ 1\ 0]$ , as defined in [161]; and  $\mathbf{b}_s \equiv \mathbf{b} = \mathbf{l} = [0\ 0\ 1]$ , as defined in [162, p. 59, 64].

The units in all our examples are normalised to lattice parameter,  $a$  is the dislocation core radius for the non-singular formulation discussed in [101], and  $b \equiv \|\mathbf{b}\|$ .

The slices we took for our contour plots in section 4.1.4 are on the middle plane of the domain at  $z = 1000$ .

We also ran a very simple simulation comparing the results between using analytic tractions as opposed to numeric ones. Finding a simple yet clear case of tractions producing catastrophically wrong behaviours can be difficult. Large differences in image forces are relatively rare and other factors often dominate. Such factors include the core radius—which affects the dislocation line tension and therefore works against the deformation of a dislocation line—mobility law and mobility parameters used, external loading, etc.

However, we found a simple and realistic configuration that is close to the setup in the infinite domain examples. The differences between those comparisons and the simulation are described in table 4.1. We use a mobility law developed in-house by B. Bromage [133], that corrects common issues found in other laws. We also rotate the domain such that the  $[1\ 1\ 1]$  and  $[1\ \bar{1}\ 0]$  crystallographic directions respectively correspond to the simulation’s  $x$  and  $y$ -directions, for this we use the

Table 4.1: Parameters for our simulation. Where  $\mathbf{R}$  is a rotation matrix such that the  $\mathbf{x}, \mathbf{y}, \mathbf{z}$  basis vectors of our simulation correspond to the  $\mathbf{b}, \mathbf{n}, \mathbf{l}$  crystallographic directions, i.e.  $\mathbf{Rx} = \mathbf{b}$ . Everything else was kept just as the previous comparisons. All values are in units of lattice parameters.

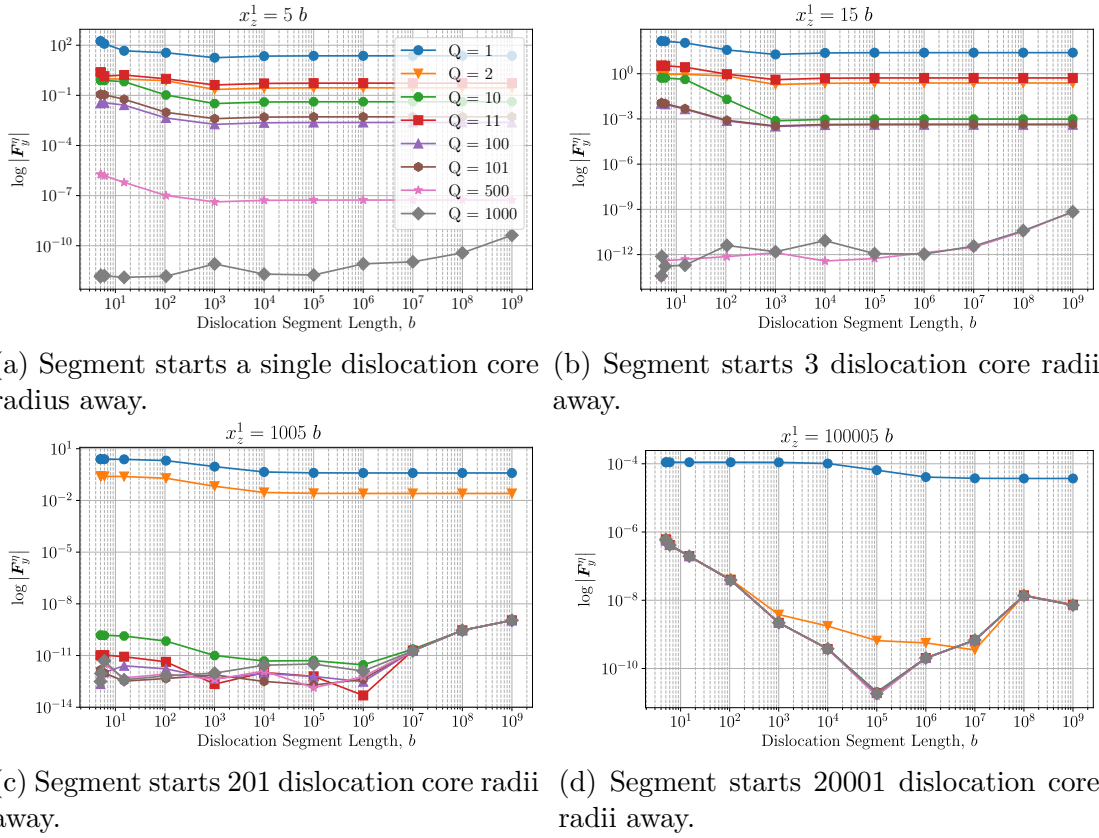
| Parameter          | Value                                                  |
|--------------------|--------------------------------------------------------|
| Crystal Structure  | BCC                                                    |
| $\mathbf{b}$       | [1 1 1]                                                |
| $\mathbf{n}$       | [1 $\bar{1}$ 0]                                        |
| $\mathbf{l}$       | [1 1 $\bar{2}$ ]                                       |
| $b$                | $\sqrt{3}/2$                                           |
| $a$                | 5                                                      |
| Grid Size          | (20, 20, 20)                                           |
| Domain Size        | (2000, 2000, 2000)                                     |
| Lattice size       | $3.18 \times 10^{-4} \mu\text{m}$                      |
| $(x_0, y_0)$       | (62.5, 1000)                                           |
| Min segment length | 50                                                     |
| Max segment length | 125                                                    |
| $\mathbf{R}$       | $[\hat{\mathbf{b}} \hat{\mathbf{n}} \hat{\mathbf{l}}]$ |

same rotation technique as [130]. The dislocation was allowed to move under no external loads or displacements, with  $\mathbf{T} = \mathbf{0}$  boundary conditions only on the  $yz$ -plane and  $\mathbf{U} = \mathbf{0}$  everywhere else.

#### 4.1.4 Results and discussion

Figure 4.9 shows that even for dislocations only one dislocation core radius (5) away from the surface element, the force can be obtained, up to numerical precision, with 1000 Gauss quadrature points  $Q$  for all segment lengths tested. It also shows a very peculiar issue Gauss quadrature has when computing integrals of rational functions when the Gauss nodes are close poles/maximal values. This undesirable behaviour is observed in the case where  $Q = 11$ . Where the highest weighted Gauss node is closest to the point where  $1/R_a$  is maximal, resulting in lower accuracy when compared to  $Q = 2, 10$  in fig. 4.9 (a) and (b). It is worth noting however that the relative errors for small numbers of quadrature points don't really start decreasing until relatively large distances. And when close to a surface, these can be quite large even under highly symmetric circumstances.

The limitations become even more evident when the dislocation line segment is parallel to a surface element. In fig. 4.10, we observe the relative errors are quite large when close to the surface. At distances larger than  $10^4$ , loss of significance causes the relative errors to converge at  $\sim 1$  which is expected as two finite precision floating point numbers get closer to zero. Of particular note is how large the



(a) Segment starts a single dislocation core radius away. (b) Segment starts 3 dislocation core radii away.

(c) Segment starts 201 dislocation core radii away. (d) Segment starts 20001 dislocation core radii away.

Figure 4.9: Log-log plot of the relative error as a function of dislocation segment length for a perpendicular edge dislocation (fig. 4.5a).  $x_z^1$  is the  $z$ -coordinate of node  $\mathbf{x}_1$ .  $\mathbf{b} = [1\ 0\ 0]$ , line direction,  $\mathbf{l} = [0\ 0\ 1]$ , and dislocation core radius,  $a = 5$ , the surface element's normal and size are,  $\mathbf{n} = [0\ 0\ 1]$ ,  $L = 1000$ , respectively.  $Q$  is the number of quadrature points per dimension.

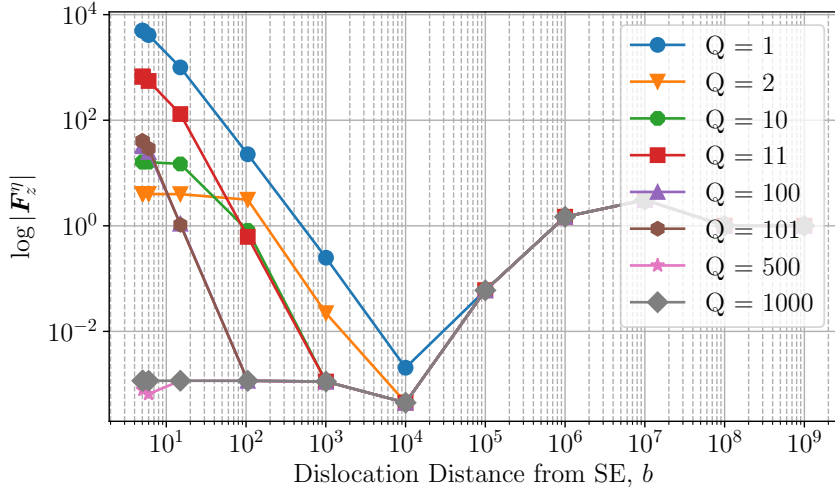


Figure 4.10: Log-log plot of the relative error as a function of distance from the surface element for a parallel edge dislocation (fig. 4.5b). Burgers vector,  $\mathbf{b} = [0\ 1\ 0]$ , line direction,  $\mathbf{l} = [1\ 0\ 0]$ , dislocation core and surface element parameters are the same as fig. 4.9. The dislocation length is fixed to  $10^6$ ,  $x \in [-0.5 \times 10^6, 0.5 \times 10^6]$  and bisects the surface element along the  $[1\ 0\ 0]$  direction. The whole dislocation was segmented into  $10^4$  pieces of length 100 to prevent the dislocation from intersecting the surface element when they were rotated to avoid the singularity. The relative error at large distances ( $> 10^6$ ) converges to one due to loss of significance.

relative errors are even at 100 lattice units away from the surface, even for large numbers of quadrature points. This figure backs up the earlier point regarding Gauss nodes close to maximal values of rational functions. It can be shocking to see that as  $Q = 2$  performs significantly better than  $Q = 10, 11, 100, 1000$  at distances from the surface as having nodes near the maximal values is a large source of error. Consequently, different configurations have different optimal numbers of points. The numerical instability of this method, which when coupled to the chaotic nature of dislocation dynamics and stiffness of the equations of motion, can lead to large deviations between simulations.

From figs. 4.9 and 4.10 one might be tempted to say that for a segment parallel to a surface, Gauss quadrature performs far worse than for a perpendicular one. However there is a further wrinkle in this problem: symmetry. To exemplify this we plot the relevant components of the stress tensor for the arrangement found in fig. 4.5(a) in figs. 4.11a to 4.11c. The  $\sigma_{xz}$  and  $\sigma_{zz}$  components are antisymmetric about the centre of the element. If we use Gauss quadrature on them, we sample equivalent but oppositely valued points that are equally weighted, thus the sum vanishes and therefore do not contribute to fig. 4.9. However,  $\sigma_{yz}$  does not vanish, but can be accurately integrated with sufficiently large  $Q$ . If we were to move the dislocation off-centre such that these symmetries are broken, the errors would

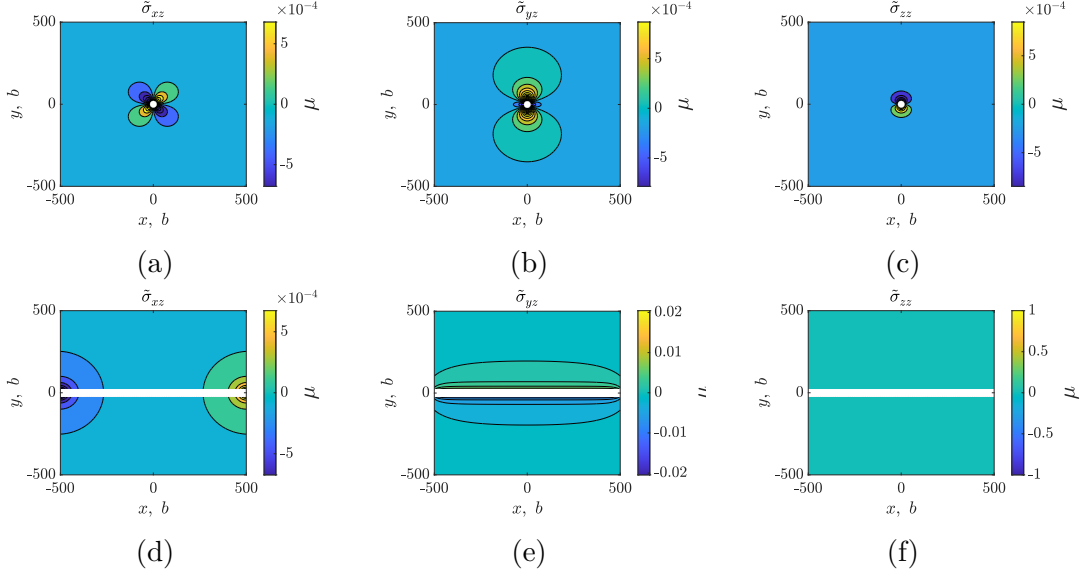


Figure 4.11: (a) to (c) show the real stress fields from a dislocation in the same configuration that yields the plots found in fig. 4.9 as shown in fig. 4.5(a), where the closest node is a dislocation core radius away from the surface,  $a = 5$ . (e) to (f) does the same for the configuration that yields fig. 4.10 as shown in fig. 4.5(b), where the whole dislocation is a core radius away from the surface,  $a = 5$ . The white line or dot is the dislocation. Units are in terms of lattice parameters.

increase.

We also plot the relevant stresses for the arrangement described by fig. 4.5(b) in figs. 4.11d to 4.11f. From fig. 4.11d and fig. 4.11e, it is immediately apparent why gauss quadrature fails so spectacularly in fig. 4.10. At low numbers of quadrature points, it fails to appropriately sample the rapidly changing value of  $\tilde{\sigma}_{xz}$  at both ends of the dislocation, as well those in the neighbourhood of the dislocation in  $\tilde{\sigma}_{yz}$ . Moreover, the further away the quadrature points are from the midpoint of the domain, the lower their relative weighting. So even with a relatively large number of them, there can still be large errors. Which is a particularly egregious problem in fig. 4.11e, and explains why such a large number of quadrature points is required to accurately compute the integral.

Despite these being artificially idealised examples that illustrate the failings of Gauss quadrature, other problematic scenarios commonly show up in simulations. These tend to worsen with smaller core radii  $a$ , fewer Gauss nodes, higher dislocation densities near surfaces, more permissive mobility functions, and coarser FE meshes. The  $\mathcal{O}(1/R)$  decay rate of  $\tilde{\sigma}$  and chaotic nature of dislocation dynamics, means these errors may result in unwarranted topological changes that cascade as the simulation advances. This is particularly deleterious when doing simulations with higher dislocation densities and/or where a large number of dislocations are close to the surface, such as nanoindentation simulations.

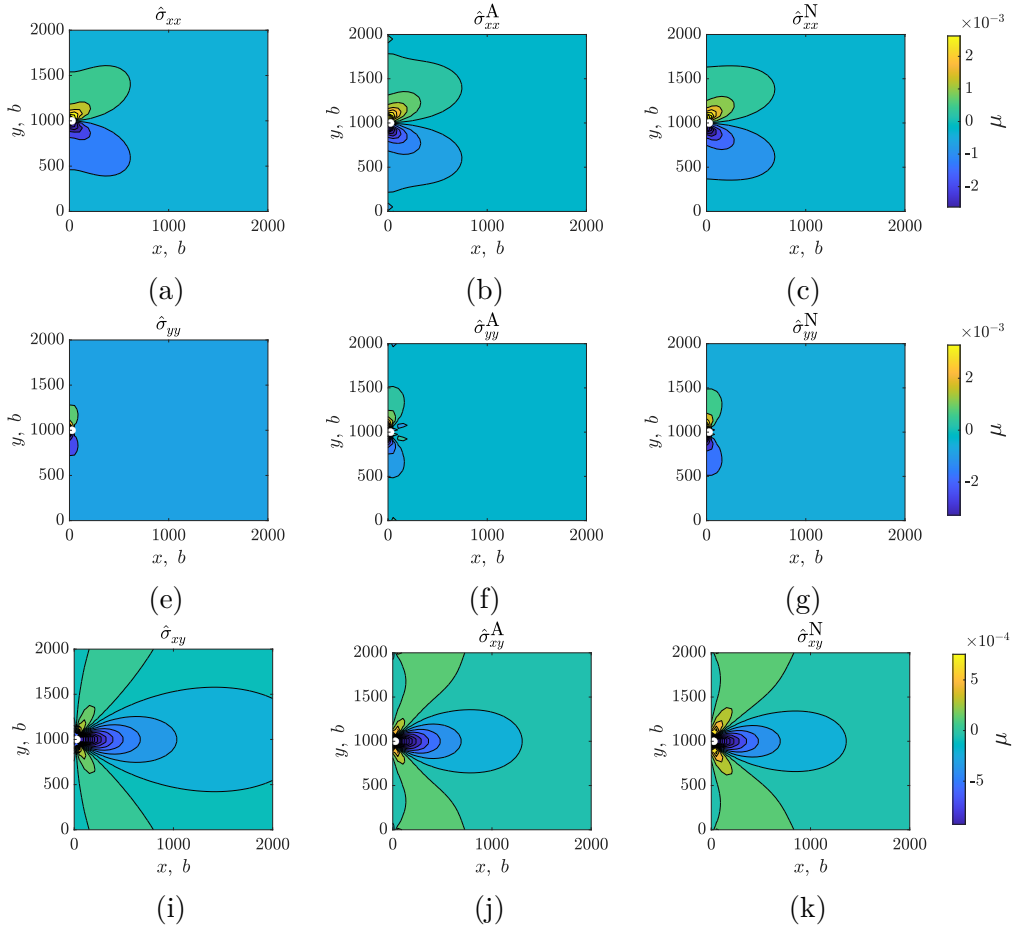


Figure 4.12: Image stresses for an edge dislocation with  $\mathbf{l} = [001]$ ,  $\mathbf{b} = [100]$ , where  $a = 5$ , with coordinates (26, 1000), i.e. the centre of the first FE from the surface at  $x = 0$ , and in the centre of the simulation box along the  $y$ -direction. (a), (e) and (i) are the stress fields for the infinite-domain solution,  $\hat{\boldsymbol{\sigma}}$ ; (b), (f) and (j) are those obtained from analytic tractions + FEM,  $\hat{\boldsymbol{\sigma}}^A$ ; (c), (g) and (k) are those obtained using numeric tractions ( $Q = 1$ ) + FEM,  $\hat{\boldsymbol{\sigma}}^N$ . (a) to (c) represent the  $xx$ ; (e) to (g) the  $yy$ ; and (i) to (k) the  $xy$  components of the stress tensor.

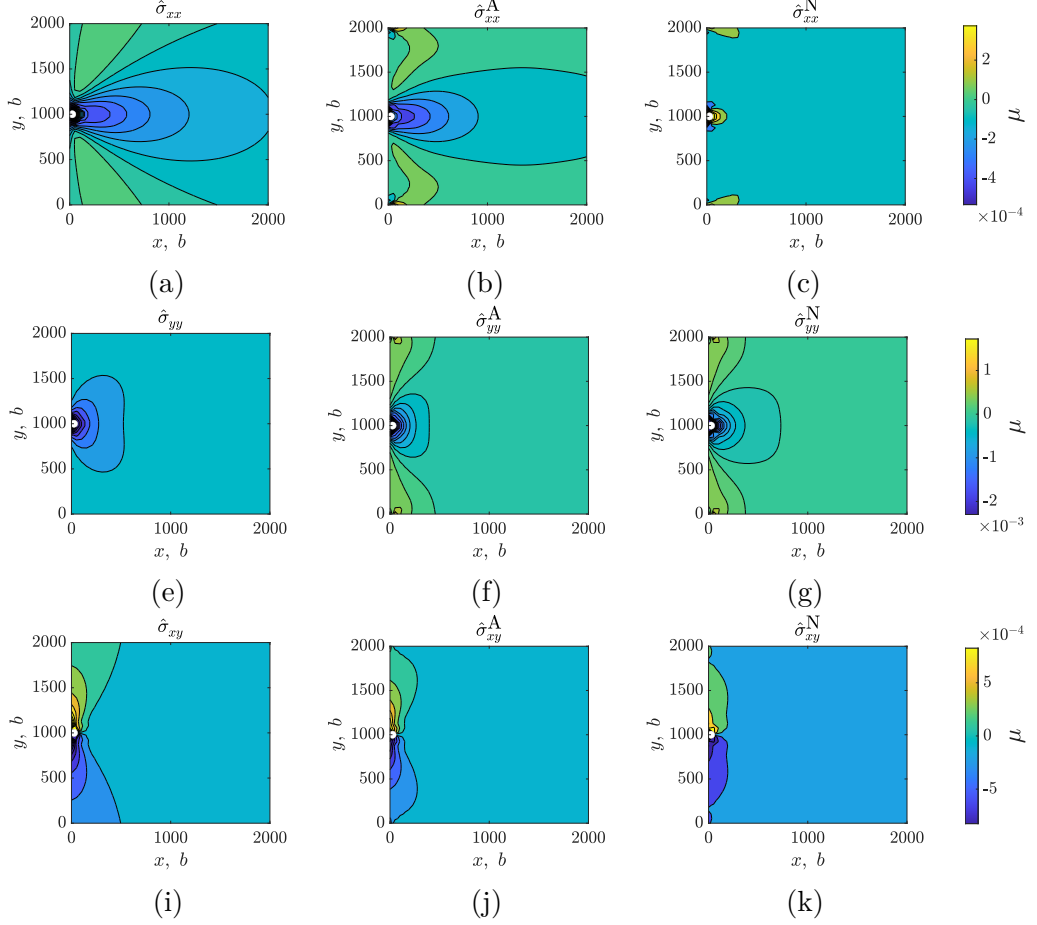


Figure 4.13: Image stresses for an edge dislocation with  $\mathbf{l} = [0\ 0\ 1]$ ,  $\mathbf{b} = [0\ 1\ 0]$ , where  $a = 5$ , with coordinates  $(26, 1000)$ , i.e. the centre of the first FE from the surface at  $x = 0$ , and in the centre of the simulation box from top to bottom. (a), (e) and (i) are the stress fields for the infinite-domain solution,  $\hat{\boldsymbol{\sigma}}$ ; (b), (f) and (j) are those obtained from analytic tractions + FEM,  $\hat{\boldsymbol{\sigma}}^A$ ; (c), (g) and (k) are those obtained using numeric tractions ( $Q = 1$ ) + FEM,  $\hat{\boldsymbol{\sigma}}^N$ . (a) to (c) represent the  $xx$ ; (e) to (g) the  $yy$ ; and (i) to (k) the  $xy$  components of the stress tensor.

As stated in section 4.1.3, tractions are used to calculate the image stresses resulting from the boundary conditions. We therefore compare the differences in image stresses resulting from numeric ( $Q = 1$ ) and analytic traction calculations of both our implementations and how they compare to the infinite-domain, singular expressions in eqs. (4.21) to (4.23)<sup>1</sup>. The stress field comparisons for all three cases are found in figs. 4.12 to 4.14, where the dislocation is denoted by a white dot.

Figure 4.12 shows the stress fields corresponding to analytic expressions for image stress components,  $\hat{\sigma}_{ij}$  in eq. (4.21) where no superscript denotes the infinite-domain singular expressions, the A superscript are the stresses calculated from

<sup>1</sup>Since the first term in each equation corresponds to the real stresses, we omit them to view the image stresses.

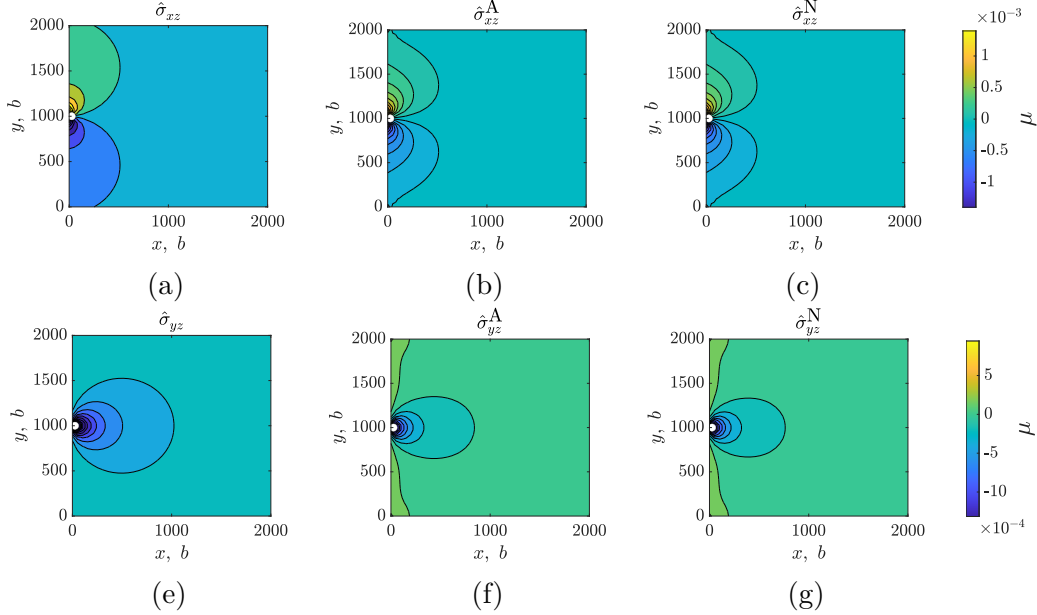


Figure 4.14: Image stresses for a screw dislocation with  $\mathbf{l} = [0\ 0\ 1]$ ,  $\mathbf{b} = [0\ 0\ 1]$ , where  $a = 5$ , with coordinates  $(26, 1000)$ , i.e. the centre of the first FE from the surface at  $x = 0$ , and in the centre of the simulation box from top to bottom. (a) and (e) are the stress fields for the infinite-domain solution,  $\hat{\boldsymbol{\sigma}}$ ; (b) and (f) are those obtained from analytic tractions + FEM,  $\hat{\boldsymbol{\sigma}}^A$ ; (c) and (g) are those obtained using numeric tractions ( $Q = 1$ ) + FEM,  $\hat{\boldsymbol{\sigma}}^N$ . (a) to (c) represent the  $xz$ ; (e) to (g) the  $yz$ .

analytic tractions and the N superscript are those coming from numeric tractions where  $Q = 1$  (same nomenclature in figs. 4.13 and 4.14). The setup corresponds to the one described in fig. 4.8 where  $\mathbf{b} = \mathbf{b}_{e1} = [1\ 0\ 0]$  and the dislocation is found at  $(26, 1000)$ .

It is clear edge effects play a role in the generated stresses. All three components have notable differences from the infinite-domain solutions resulting from the finite constraints, but the overall agreement between them all is quite good.

Things get markedly more interesting when looking at  $\mathbf{b} = \mathbf{b}_{e2} = [0\ 1\ 0]$  in fig. 4.13 for a dislocation in the same place,  $(26, 1000)$ . Of particular note is  $\hat{\sigma}_{xx}$ , where a comparison between figs. 4.13a and 4.13b and fig. 4.13c reveals one of the major issues with numeric tractions. If we look at the neighbourhood of the dislocation (just to the right), we will find a sign inversion i.e. yellow and green contours as opposed to purple and blue. As well as a drastically different isosurface shape. Image stresses like those can lead dislocations to behave quite differently than they should, particularly if the sign inversion also has a significantly different magnitude than the correct solution. Specifically, there is a region in the positive  $x$ -direction away from the dislocation where  $\hat{\sigma}_{xx}$  is tensile rather than compressive. It is as absurd as a ship that floats by lowering the water level.

Perhaps the most evident deformation resulting from the displacement bound-

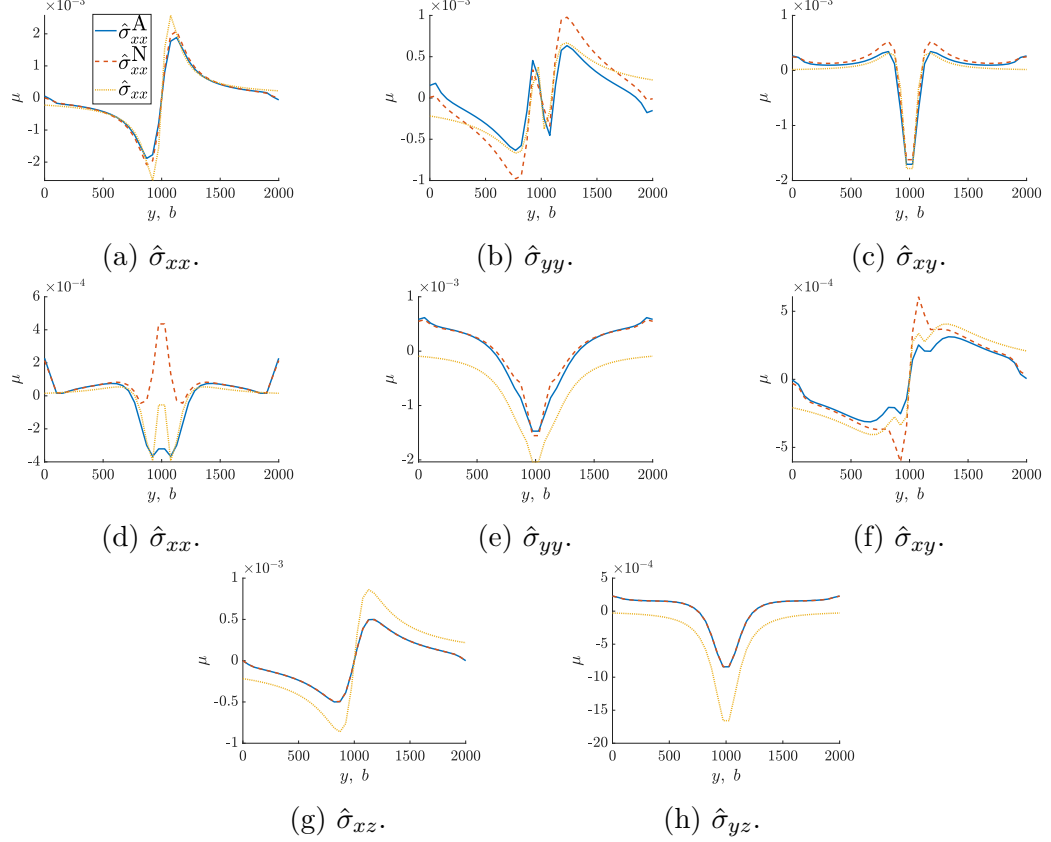


Figure 4.15: Line plots of the image stresses of a dislocation at  $(26, 1000)$  for a line going through  $x = 103$  (start of the third element) for the analytic image stresses, as well as those calculated with numeric and analytic tractions. (a) to (c) correspond to  $\mathbf{b} = \mathbf{b}_{\text{e}1}$ , (d) to (f)  $\mathbf{b} = \mathbf{b}_{\text{e}2}$  and (g) to (h) to  $\mathbf{b} = \mathbf{b}_{\text{s}}$ .

aries can be seen when  $\mathbf{b} = \mathbf{b}_{\text{s}}$  in fig. 4.14, where the lobes of the isolines are highly deformed when compared to the infinite-domain solutions. Though deformed, their familiar shape is still recognisable and both analytic and numeric tractions yield fairly similar fields.

From figs. 4.12 to 4.14 it seems like both analytic and numeric tractions are appropriate in most cases. At least at these scales, there is only one instance where numeric tractions yield very incorrect results. That said, these can have a significant impact on simulations, particularly those where multiple dislocations interact with surfaces in close proximity with one another.

We also produced line plots to better show how the stress fields deviate from one another. Figure 4.15 shows line plots through the line  $x = 103$  for a dislocation at  $(26, 1000)$ . Figures 4.15a to 4.15c correspond to  $\mathbf{b} = \mathbf{b}_{\text{e}1}$ , figs. 4.15d to 4.15f to  $\mathbf{b} = \mathbf{b}_{\text{e}2}$  and figs. 4.15g and 4.15h to  $\mathbf{b} = \mathbf{b}_{\text{s}}$ . Here, the singular nature of the infinite-domain solutions is evidenced by the sharp spikes in its stresses. In general, the non-singular formulation smoothes out the stress line plots. However, there are a few instances where the numeric tractions lead to larger spikes than

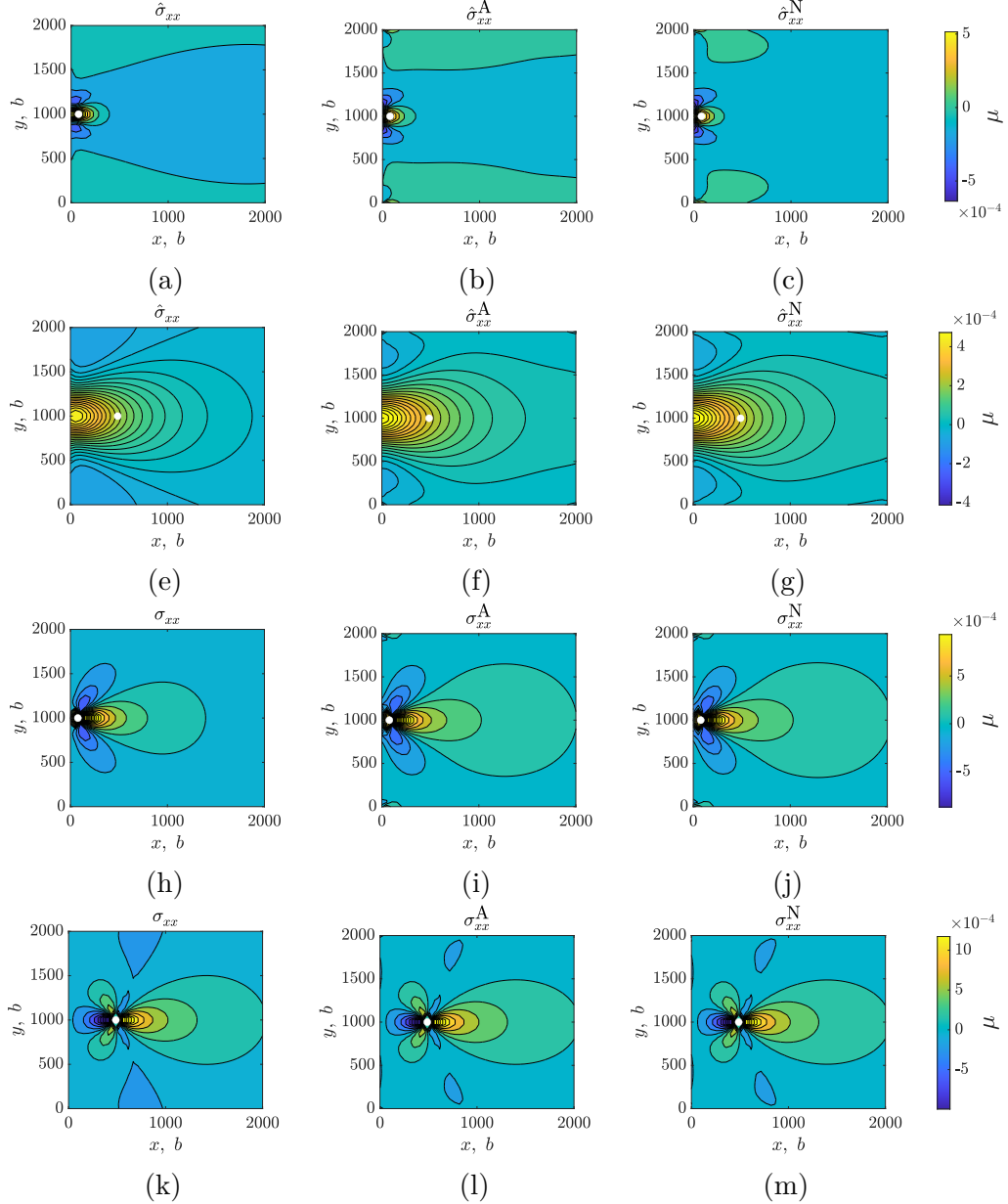


Figure 4.16: Stresses for an edge dislocation with  $\mathbf{l} = [0\ 0\ 1]$ ,  $\mathbf{b} = [0\ 1\ 0]$ . Subfigures (a) to (g) show image stresses; (h) to (m) show total stresses. In subfigures (a) to (c) and (h) to (j) the dislocation is found at  $(77, 1000)$ ; in (e) to (g) and (k) to (m) the dislocation is at  $(487, 1000)$ .

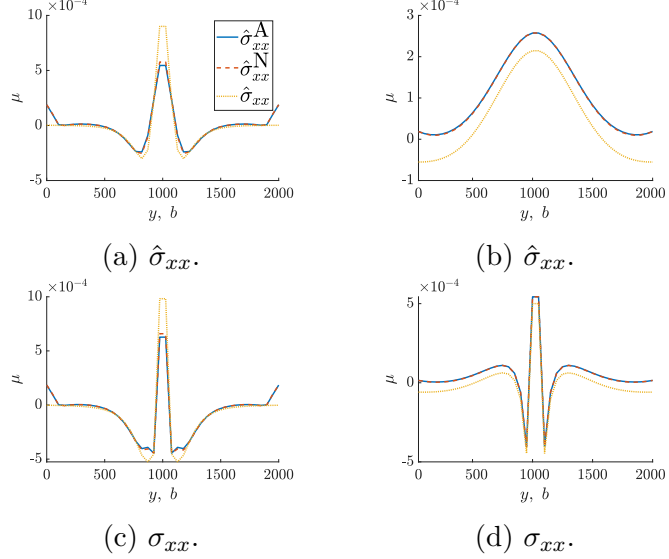


Figure 4.17: Line plots corresponding to fig. 4.16. (a) and (c) are of the image stresses; (b) and (d) are of total stresses. (a) and (b) are of a dislocation at  $(77, 1000)$ , taken along the line  $x = 103$ . (b) and (d) are of a dislocation at  $(487, 1000)$ , taken along the line  $x = 513$ .

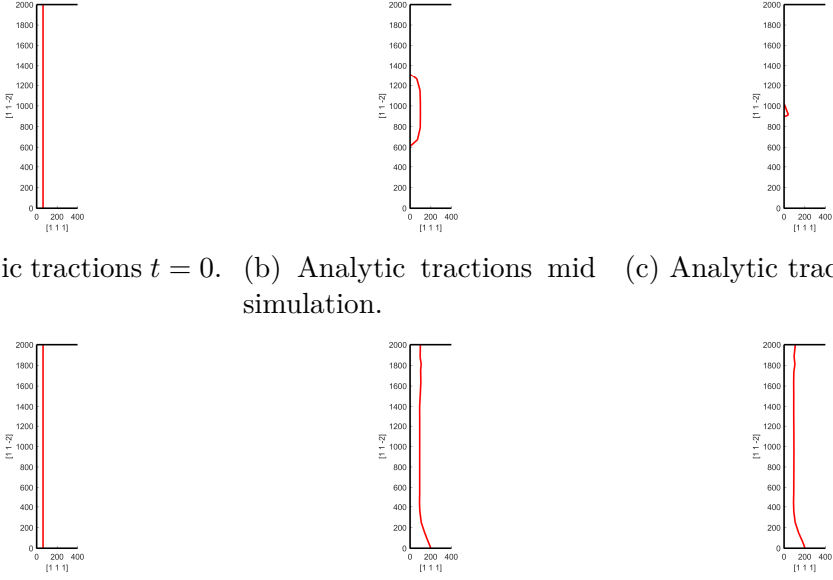
even the infinite-domain solutions such as in fig. 4.15d. Again, the general shape of the line plots is the same but the tendency for numerical tractions to spike under specific circumstances is evident in almost every case.

To show the convergence in methods we also show stress fields in fig. 4.17 and line plots fig. 4.17 of the image and total stress fields as an edge dislocation with  $\mathbf{b} = \mathbf{b}_{e2}$  moves from  $(77, 1000)$  to  $(487, 1000)$ . The line plots are taken from the second closest set of nodes in the positive  $x$ -direction i.e. at  $x = 103, 513$ .

Notice that the image stresses in figs. 4.16a to 4.16c are all very close to fig. 4.13c, which is the stress field calculated via numerical tractions for a dislocation that is slightly closer to the surface. Essentially, the numerical tractions over or underestimated a set of forces something that become the dominant contributors as the dislocation moves away from the surface.

From figs. 4.16 and 4.17 it can be observed that both analytic and numeric tractions converge to similar shapes to each other as expected. However it also becomes clear that the infinite-domain solution is not totally accurate for image stresses in finite domains due to edge effects.

Lastly, to show how much numeric tractions can affect a result, fig. 4.18 shows a few snapshots of the simulation described in section 4.1.3. The figures shown are not at equivalent times because the simulations using numeric tractions ran indefinitely. The line tension equilibrated with the image forces on the traction-free surface, preventing the dislocation from exiting and keeping it oscillating in a local energy minimum. The simulation using analytic tractions ended when the



(a) Analytic tractions  $t = 0$ . (b) Analytic tractions mid simulation. (c) Analytic tractions end.

(d) Numeric tractions  $t = 0$ . (e) Numeric tractions mid simulation. (f) Numeric tractions  $t \rightarrow \infty$ .

Figure 4.18: Progression of simulations using both traction calculation methods.

dislocation completely exited the surface as expected. It is feasible that at some point, the simulation using numeric tractions could jump out of the local minimum due to some spike in the tractions, but the last image was taken for a simulation time approximately 20 times greater than it took the one using analytic tractions to end when the dislocation fully exited the box.

### 4.1.5 Conclusions

Often the effects of tractions on a simulation can be quite subtle if things do not go catastrophically wrong, but a quick and easy way of seeing how the numeric tractions have a tendency to spike and invert sign (as in fig. 4.15d) is to pause a simulation while its running and scatter plot the numeric tractions v.s. analytic ones. The plot will show a positive correlation—as the sign inversions in numeric tractions are relatively rare events—but whichever axis corresponds to the numeric tractions will have the largest range. Using proportional axes makes the differences quite evident even at a quick glance as the aspect ratio will be far from 1:1.

In other parts of our work, we have noted that despite the analytic tractions taking approximately 10 times longer to compute than numerically calculated tractions with  $Q = 1$  (which agrees with the findings in [86]), yield more stable and ultimately faster simulations. Even simple simulations are typically faster when using analytic tractions over numeric ones. This was not the case with the simulation we show here, but the numeric tractions led to a hung simulation, which we have found is quite common. The margin by which using analytic tractions

leads to faster overall simulations grows as simulation complexity increases. Only the simplest simulations initially benefit from numeric tractions but this often decreases and reverses as the simulation advances. Another fortunate side effect of more accurate tractions is the fact that fewer dislocation segments are generated during simulations, which Bromage and Tarleton [133] found when correctly accounting for the displacements generated by dislocations.

Given our findings, we cannot recommend using numeric tractions when analytic ones are available. The losses in computational speed that result from moving from one to the other are more than made up for by the fewer topological operations, fewer generated segments, and more accurate velocities. All of which result in fewer calculations of segment-segment interactions, fewer collisions, larger timesteps and ultimately cleaner simulations that run into fewer snags along the way.

There is a case however, for combining both approaches in larger scale simulations. Since both numeric and analytic tractions converge to the same value as the dislocation-surface distance increases, a hybrid approach may possibly be undertaken without many negatives. Furthermore, [86] also derived a Taylor series expansion of the solutions which can be used in cases where the dislocation-surface distance is large. These may be worth exploring in larger scale simulations. However, in the types of systems we model, other parts of our model tend to be much more rate-limiting than tractions. As such, we have all but ceased to use numeric tractions in our work.

## 4.2 GPU parallelisation of analytic tractions

### 4.2.1 Introduction

Graphics Processing Units (GPUs) have been leveraged by digital art, animation studios and gaming companies since the 1990s to offload repetitive, grid-based mathematical computations away from the Central Processing Units (CPUs). These operations are usually very computationally cheap, require minimal logic, and do not need more than single precision (32-bit) arithmetic [66–68], in fact, increases in accuracy would get lost in the RGB channel regardless. As such, GPUs evolved primarily to efficiently perform lightweight operations on vast amounts of 32-bit data. As such, their memory buses are extremely fast and their processors very minimalistic.

It wasn't until much later that engineers and scientists picked up on the potential of GPUs [72, 163, 164]. Fields where lower precision is advantageous—because it increases the signal to noise ratio, or real-world tolerances exceed the in-silico

precision—such as data science, civil engineering and image/signal processing, first leveraged this technology. In fact, many big data applications operate on half and some even go as low as quarter precision simply due to the low sensitivity, large amount of noise and vast quantities of data [165].

NVidia has spearheaded the development and adoption of scientific-computing and high performance computing (HPC) GPUs with the development of their proprietary Compute Unified Device Architecture, CUDA technology. They now produce a wide range of GPUs tailored for scientific applications. These have specialised architecture [61].

- Tensor modules for fast, piecewise matrix multiplication.
- Larger but slower memory buses mean higher concurrent resource use because scientific computations are expensive, so it is better to have them work through a lot of data while more memory is being fetched, rather than fetching small amounts of memory really quickly but having to wait for the processors to finish their computation.
- Expanded precision capabilities.
- Specialised registers, specialised hierarchical memory architecture, etc.

For all their advantages, parallel algorithms are fundamentally different to serial ones. In particular the way GPUs differ from CPUs makes it a non-trivial task to properly parallelise an algorithm. Doing so poorly can result in decreased performance, particularly when using high performance/scientific computing cards. There is also the issue of scaling, whereby the cost of utilising the GPU may not be worth paying until a certain computation size. In this section, we detail the work, results and conclusions of parallelising the analytic traction calculation.

## 4.2.2 Methodology

### 4.2.2.1 Data mapping

A cache is a store of memory used to reduce the cost of accessing data from the main memory. CPUs and GPUs have cache hierarchies designed to progressively get smaller and faster the closer they are to the processor. This reduces the average cost of accessing data because the missing data can be looked for in progressively higher cache levels. It is important to know that caches operate as single units, meaning that every time a processor needs data that is not found in a cache (cache miss), the whole cache needs to be updated. This means that every time there is a cache miss, any operations dependent on the missing data have to wait until the

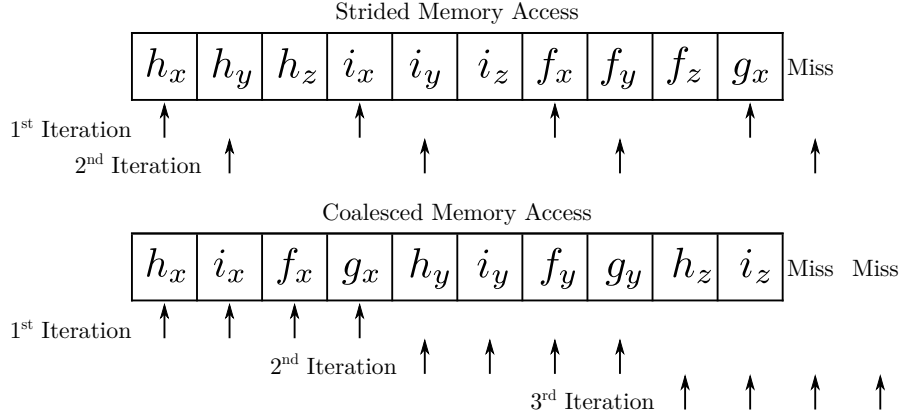


Figure 4.19: Memory access patterns. Arrows are threads in a warp simultaneously requesting access to memory from the cache. All processors work simultaneously, so they can only proceed until every one of them has the necessary data.

new data arrives. As processors have gotten faster, memory speeds have not kept up. As a result, minimising the ratio of cache misses to cache hits has become an important aspect of optimising software applications [166, 167]. Optimising cache use is of particular importance in GPUs.

The increasingly divergent speeds of processors and memory, are the reason why scientific computing GPUs opt for larger but slower memory buses. In properly written software, this feature decreases the time spent waiting for a processor to finish whilst the data is ready [168–170]. Instead the infrastructure and cost associated with faster memory can be better utilised on more processing power. However, in improperly written code, the cache miss to hit ratio will be large. Non-scientific applications can get away with this to an extent, because memory buses are fast and computational cost is low. But for scientific applications—and in particular when using specialised GPUs—this can be catastrophic for performance.

In NVidia GPUs, “coalesced memory access” is when, a single cache line contains all the data needed by a “warp”—a collection of 32 threads which operate “simultaneously” as a single unit on separate pieces of data—to carry out an instruction/process. This is not always possible because it is problem-dependent, so usually the best we can do is ensure there are no unnecessary memory fetches by arranging simultaneously-used data in a contiguous manner. Figure 4.19 is a simple example of this.

Since threads in a warp behave as a single unit, they hang until every other thread in the warp has the data it needs to execute the next instruction. Under a strided memory access pattern, this happens more often than if the data were contiguously accessed. Furthermore, cache usage optimisation heuristics have the task of deciding what memory to bring in order to minimise future cache misses.

Under a contiguous memory access model, this done by simply placing the first missing item as the first item in the next cache line. However, even in the simple example of strided memory access shown in fig. 4.19, it's easy to see how this is suboptimal. To start with, a new cache line is needed for the second iteration instead of the third, as it would be if the access pattern were contiguous. Then, the new cache line could start with  $h_y$  and still work for the second iteration, but then a new cache line would be needed for the third. However, grabbing the first missing item as the first item of the cache line used in the second iteration means going back down for the third iteration. In fact, the optimum strategy in this case would be to start the cache line for the second iteration on the third item,  $h_z$ , in the cache line for the first iteration.

As a result, we have to be extremely careful when mapping CPU (host) memory, arranged to be advantageous for serial access (and therefore human intuition), to device (GPU) memory, arranged for parallel access.

#### 4.2.2.2 Parallelisation schemes

The traction calculation is  $\mathcal{O}(MN)$ , where  $M$  is the number of surface elements and  $N$  the number of segments. As such, there are two first order parallelisation strategies. Parallelising over elements and looping over segments; parallelising over segments and looping over elements. And two second order parallelisation strategies. Parallelising over elements and subparallelising over segments and vice-versa. However, higher order parallelisations are usually disadvantageous unless the problem is very computationally cheap because there is more competition for parallel resource use. We only implemented both first order parallelisations. There cannot be a parallelisation over nodes as the unit problem is a single surface element and dislocation segment.

Both first order parallelisations have similar performances, but parallelising over dislocations have better scaling as simulations advance because the number of surface elements is constant while the number of dislocation segments tends to increase. The choice of parallelisation will depend on the relative amounts of surface elements to dislocation segments.

The algorithm for mapping from the objects to be parallelised over from host (CPU) to device (GPU) memory is the same in either case. The only thing that changes is that surface elements have 4 nodes and dislocation segments have 2. If parallelising over dislocation segments, the Burgers vector also needs to be mapped in the same manner, but it is equivalent to having a single ‘node’. The mapping

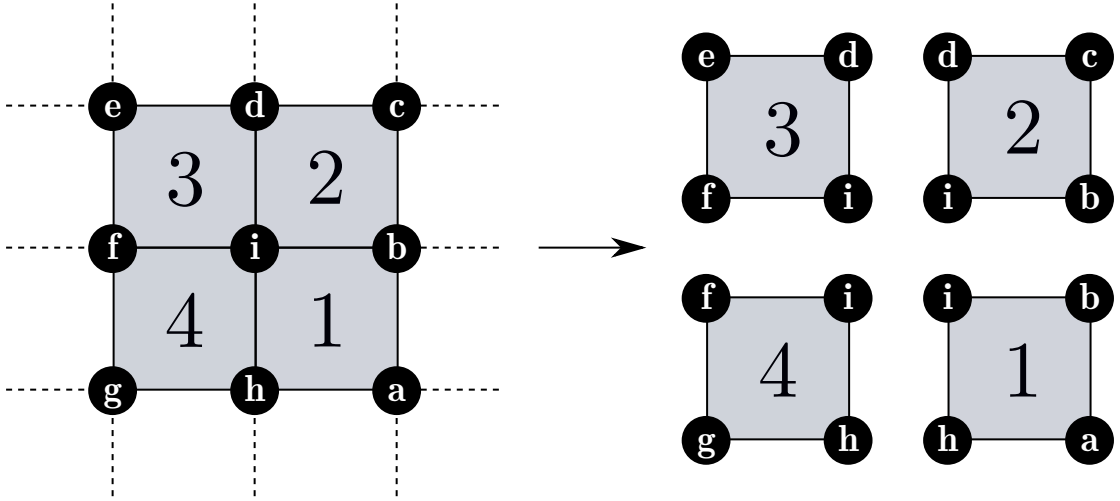


Figure 4.20: Each linear rectangular surface element is mapped to one thread.

is as follows,

$$\mathbf{X}_{en} := [x_{en}, y_{en}, z_{en}] \quad (4.28a)$$

$$\begin{aligned} \mathbf{X}_{(1 \rightarrow E)n} &\mapsto \mathbf{X}_n \\ \mathbf{X}_n &:= [x_{1n}, y_{1n}, z_{1n}, \dots, x_{En}, y_{En}, z_{En}] \end{aligned} \quad (4.28b)$$

$$\begin{aligned} \mathbf{X}_{1 \rightarrow N} &\mapsto \mathbf{X} \\ &[x_{11}, \dots, x_{E1}, x_{12}, \dots, x_{E2}, \dots, x_{1N}, \dots, x_{EN}, \\ \mathbf{X} &:= y_{11}, \dots, y_{E1}, y_{12}, \dots, y_{E2}, \dots, y_{1N}, \dots, y_{EN}, \\ &z_{11}, \dots, z_{E1}, z_{12}, \dots, z_{E2}, \dots, z_{1N}, \dots, z_{EN}] . \end{aligned} \quad (4.28c)$$

where  $e$  is the element to be mapped,  $n$  the node number,  $E$  the total number of elements and  $N$  the total number of nodes per element.

For a set up like fig. 4.20, parallelising over the surface elements with node labels corresponding to fig. 4.3,  $\mathbf{x}_1$ ,  $\mathbf{x}_2$ ,  $\mathbf{x}_3$  and  $\mathbf{x}_4$  yields,

$$\mathbf{X} = \left[ \underbrace{h_x, i_x, f_x, g_x}_{\mathbf{x}_1}, \underbrace{a_x, b_x, i_x, h_x}_{\mathbf{x}_2}, \underbrace{i_x, d_x, e_x, f_x}_{\mathbf{x}_3}, \underbrace{b_x, c_x, d_x, i_x}_{\mathbf{x}_4}, \dots \text{y-coord} \dots, \dots \text{z-coord} \dots \right] . \quad (4.29)$$

Whether the parallelisation is done over dislocation line segments or surface elements, the item that wasn't parallelised over must also be mapped such that it can be contiguously accessed by the GPU. However this just means merging

arrays in a very simple manner,

$$\mathbf{X}_{en} := [x_{en}, y_{en}, z_{en}] \quad (4.30a)$$

$$\begin{aligned} \mathbf{X}_{(1 \rightarrow E)n} &\mapsto \mathbf{X}_n \\ \mathbf{X}_n &:= [x_{1n}, \dots, x_{En}, y_{1n}, \dots, y_{En}, z_{1n}, \dots, z_{En}] \end{aligned} \quad (4.30b)$$

$$\begin{aligned} \mathbf{X}_{1 \rightarrow N} &\mapsto \mathbf{X} \\ &[x_{11}, \dots, x_{E1}, y_{11}, \dots, y_{E1}, z_{11}, \dots, z_{E1} \\ \mathbf{X} &:= \dots, \\ &x_{1M}, \dots, x_{EN}, y_{1N}, \dots, y_{EN}, z_{1N}, \dots, z_{EN}] \end{aligned} \quad (4.30c)$$

In a similar vein to eq. (4.29), using eq. (4.30) to map the data yields,

$$\begin{aligned} \mathbf{X} = & \dots \underbrace{\mathbf{x}_0, xyz\text{-coords} \dots,}_{h_x, i_x, f_x, g_x, h_y, i_y, f_y, g_y, h_z, i_z, f_z, g_z,} \\ & \dots \mathbf{x}_1, xyz\text{-coords} \dots, \\ & \dots \mathbf{x}_2, xyz\text{-coords} \dots, \\ & \dots \mathbf{x}_3, xyz\text{-coords} \dots]. \end{aligned} \quad (4.31)$$

#### 4.2.2.3 Maximising performance

In order to maximise performance after properly mapping memory to the GPU we have to minimise hang time. A good rule of thumb is to try optimising cache use. Full cache line utilisation (coalesced memory access) is achieved if cache lines can accomodate  $l$  entries given by eq. (4.32),

$$l = \begin{cases} a \times N \times E, & a > 0 \in \mathbb{N} \\ \text{or} \\ \frac{1}{2^a} \times N \times E, & a \geq 0 \in \mathbb{N}, N \times E \equiv 0 \pmod{2^a}, \end{cases} \quad (4.32)$$

where  $a$  is the number of entries,  $N$  the number of nodes and  $E$  the number of elements. This can be achieved by making use of the flexibility afforded by the NVidida architecture. Every GPU has various collections of warps called Streaming Microprocessors (SMs). Each SM is independent of other SMs, however, warps within an SM all share certain resources such as various levels of caches and schedulers. Each SM can be split into blocks of threads, all of which share some resources. The optimal usage entails finding the best block size (preferably a multiple of 32 to maximise thread usage, as the smallest unit of processing is a warp) for a particular problem. Each block as a dimension (the number of threads

$$N = 4, E = 4$$

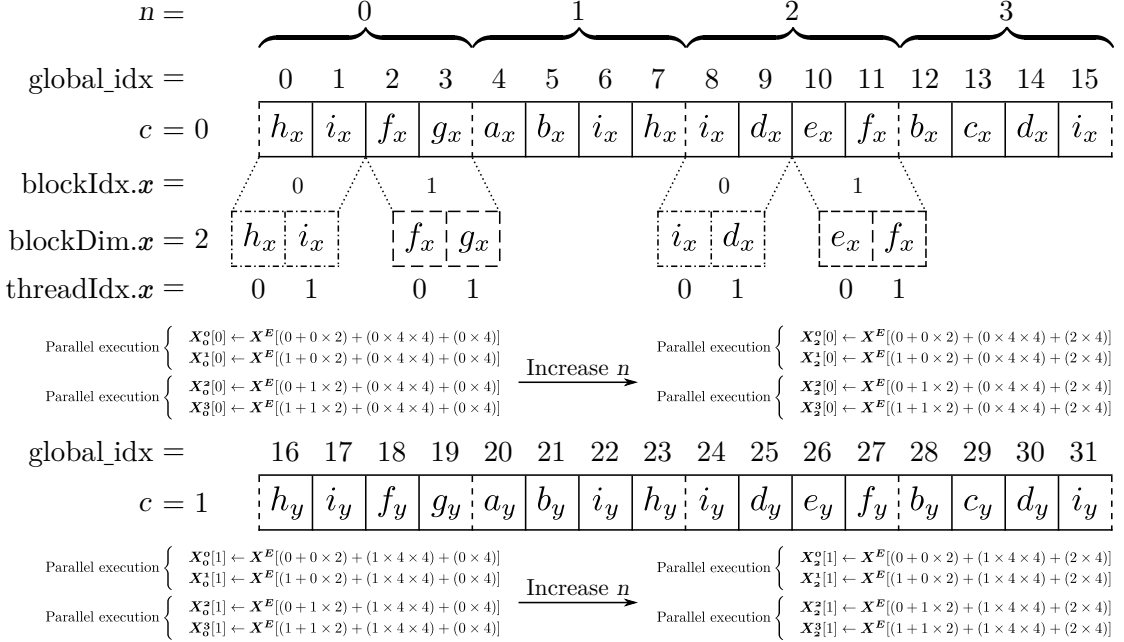


Figure 4.21: Minimum working complete example of a thread block obtaining data from global memory, from parallelising over the four surface elements in fig. 4.20 and mapped by eq. (4.28).  $\mathbf{X}_a^b$  denotes a 1D array of length three containing the  $xyz$ -coordinates of node  $a$  of element  $b$ . Each thread concerns itself with only one element at a time. The dash-dot and dashed boxes represent cache lines for a thread block, the dotted line represents a memory fetch, and the dashed lines in  $\mathbf{X}^E$  represent steps of  $E$  entries (the start of the data for the next node of the element type we're dealing with). The memory operations are not shown twice to minimise redundancy.

inside it), an index (there can be multiple blocks in a single SM), and each thread has an index that identifies it within its block. These values are used to index the global device memory. Figure 4.21 has an example of how this works for a block of two threads and a set up as described by fig. 4.20 and mapping by eq. (4.28).

Realistically, this is extremely difficult to achieve, particularly in dynamic, non-conservative simulations such as discrete dislocation dynamics. So we also came up with two heuristics that aim to utilise as many computational resources as possible.

$$T = 32 \lceil (n \bmod T_{\max}) / 32 \rceil \quad (4.33)$$

$$G = \lceil (n + T - 1) / T \rceil, \quad (4.34)$$

where  $n$  is the number of items to be parallelised (either surface elements or dislocation line segments),  $T$  is the number of threads per block,  $T_{\max}$  is the maximum number of threads allowed in a block (GPU dependent) and  $G$  is the total number of blocks.  $G$  ensures the load gets distributed evenly across as many

blocks as possible, and  $T$  ensures each thread block is busy for the longest time possible between memory fetches.

#### 4.2.2.4 Solving parallelisation problems

One of the things that can be missed during parallelisation is the fact that writing to global memory is asynchronous. This means that threads can race each other to write to global memory. Fortunately we avoided some of the more egregious issues because each unit problem is independent of the rest. However, the forces calculated independently across threads have to be sequentially added to the overall force on each node. This is done with atomic operations, that force the threads to sequentially write their contributions to the global memory.

The second issue is that of the singularity when a dislocation segment is parallel to a surface, see eq. (4.18).

The reason this is such an issue is because GPUs cannot branch. That is to say, every case of an if or case statement is executed regardless of whether a condition is met or not. The only difference is that the values are only stored if a condition is met. This means that cases as rare yet costly as these, disproportionately impact performance. Parallelising over special cases is not worth the time because they are not common enough, so the best solution use the fact that GPUs and CPUs work asynchronously and have the GPU only store the data for non-special cases, while the CPU only calculates the contributions from the special cases. Both contributions are added back at the end.

### 4.2.3 Results, discussion and conclusions

One of the greatest disappointments of this project can be seen in fig. 4.22. It was produced using a linux workstation with an NVidia GTX 750 and an Intel Core i5-8500 @ 3.0 GHz. Both GPU and CPU are equally outdated so the comparison remains relatively fair insofar as other non-HPC set ups are concerned. That said, using a high performance GPU would help a great deal as CPUs have somewhat stagnated in comparison. Regardless it wouldn't help the root cause. The  $x$ -axis is scaled to  $10^5$  dislocation segments. We have nowhere near the capacity to run a simulation with  $10^5$  segments. The  $(O)(N^2)$  collision and segment-segment force algorithms and  $(O)(N!)$  separation prevent us from going much past  $10^4$  segments. Moreover, fig. 4.22 was obtained using only non-parallel segments, the code checking for parallel ones in the CPU was not even compiled. Therefore, the speed up is purely from the GPU. Unfortunately, checking for the special case means the CPU can lag behind the GPU in some scenarios, reducing the true gains by a noticeable margin.

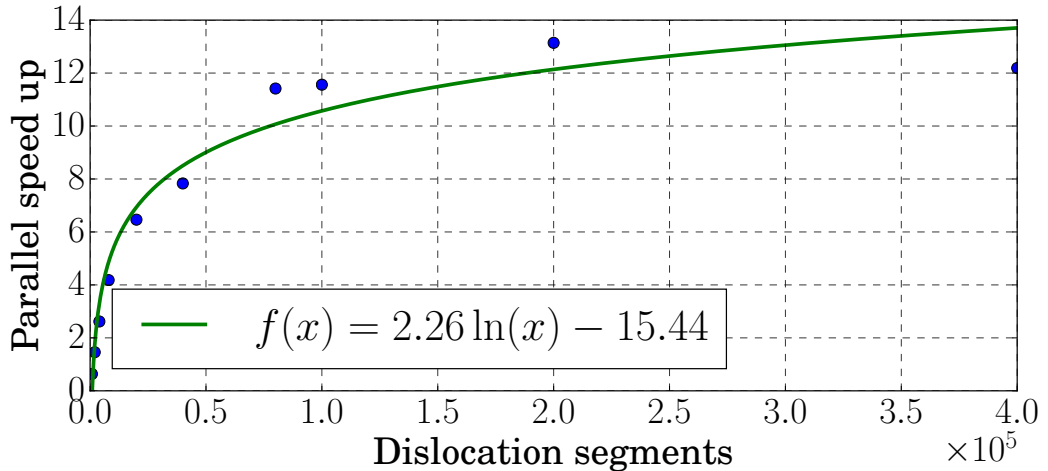


Figure 4.22: Parallel speedup on an NVidia GTX 750 and an Intel Core i5-8500 @ 3.0 GHz.

While using the GPU-accelerated code does not actively hinder most simulations, it doesn't help much either. Larger simulations on more advanced hardware are sped up, but other processes slow them down before the computational gains can be realised.

The analytic traction calculation is particularly troublesome for parallelisation. Not only is it much more computationally intensive than what GPUs are normally used for, but also has disproportionately expensive and rare corner cases, and has an awkward unit problem that necessitates a lot of data. It is too far removed from the relatively simpler layouts of "trivially" parallelisable grid-based problems found in fluid dynamics, civil engineering and image processing that get so much out of GPU parallelisation.

The silver lining to this is that the parallelised code is close to optimal. So when the rest of the software and hardware catch up to the complexity presented by the analytic tractions, it'll be there to shine like it deserves.



# **Chapter 5**

## **Simulations**

### **5.1 Zinc tensile cantilever**

#### **5.1.1 Introduction**

#### **5.1.2 Methodology**

#### **5.1.3 Results and discussion**

#### **5.1.4 Conclusions**

### **5.2 Tungsten cyclic loading and unloading cantilever**

#### **5.2.1 Introduction**

#### **5.2.2 Methodology**

#### **5.2.3 Results and discussion**

#### **5.2.4 Conclusions**



# Chapter 6

## Future work

It is clear that there are some fundamental problems preventing us from exploiting the capabilities of discrete dislocation dynamics. The code DDLab, the code that EasyDD is based on made some decisions that would ultimately limit its potential. Namely, the lack of attention paid to the cost of dynamic memory allocation, procedural nature of the code, and its choice of programming language. These choices were reasonable upon inception, but as the Tarleton group has increased in size and maturity it has become evident that it is not enough. We are reaching the upper limits of what can be done with **MATLAB**. There are more things we can do, more things we are doing. But a constant obstacle in obtaining results is how long they take to get and how difficult it is to add new functionality, even changing boundary conditions.

The work described in chapters 2 to 4 has done much in not only producing more accurate simulations, but doing so faster. Fengxian Liu's work on modelling climb, diffusion and inclusions would greatly benefit from better designed code. Haiyang Yu's work on modelling hydrogen [130] and nanoindentation would also stand to benefit a great deal from a parallelised and faster dislocation separation algorithm. Potential work relevant to modelling dislocation dynamics in nuclear reactors such as post-damage cascade dislocation dynamics [171], necessitates spontaneous generation of dislocations as a network evolves. Including stochasticity in the form of Langevin dynamics [172] is also highly relevant, especially at higher temperatures.

Many of these require a complete overhaul to some of the most fundamental parts of EasyDD. Even so it would be hindered by the fact that **MATLAB** is a scripting language, not designed to be a scientific computing one. It lacks many modern features that make life easy when dealing with large codebases. Furthermore, the need for licences can represent a prohibitive barrier for users and researchers. Not only this, but the cost of distributed licences that allow **MATLAB** to run on clusters severely limits scalability and potential for collaboration.

But there is a better way. Prompted by the public release of the Imperial College COVID-19 source code <https://github.com/mrc-ide/covid-sim>, and the recurring issues with computational efficiency, compiler compatibility and availability, and fundamental technical debt inherited from DDLab [129]. We started a weekend project that has turned out to be *extremely* promising.

The language of choice is **Julia** [173]. An open-source JIT (just in time) compiled language designed for scientific computing. It has many features that make it an excellent candidate for a new generation of open, scientific software.

1. Multiple dispatch: methods are dispatched and compiled based on the types of all their arguments, the types propagate their way through child functions, creating optimal code without having to worry about data types.
2. Type system: its type system is based on set theory, where types are arranged in a genealogical tree with broader types giving way to narrower ones, e.g. `Float64 <: AbstractFloat <: Real <: Number <: Any == true`. Structures can be parametric on type. These features let developers create generic code without bothering with type annotations. This type of code greatly improves modularity and allows for “magic” like automatic differentiation without the programme knowing the rules of calculus.
3. CPU and GPU Parallelisation: parallelising loops is trivial.
4. Metaprogramming: lets code write code. This can be used to autoparallelise functions without rewriting. It also lets developers define custom syntax and precompute values like an extremely powerful C-preprocessor.
5. Modern features: **Julia** has all the features of a modern programming language. From a booming and quickly growing package ecosystem already with a few best in class libraries; an integrated testing system and documentation generation; extremely powerful code introspection tools; to interactivity.

The code can be found here <https://github.com/dcelisgarza/DDD.jl>. As it has been a didactic side project, it is nowhere near feature complete. But so far, comparisons with C-accelerated portions of EasyDD peg it at around 10% faster. Direct comparisons to pure MATLAB show between 5 to  $> 1000 \times$  faster depending on the function. It is the result of the lessons learned while working on EasyDD. Its design avoids the same pitfalls and has a clear vision for usability, modularity, and extensibility, without sacrificing performance. We think it to be a more than worthwhile endeavour to bite the bullet now rather than wait until there is no more juice to squeeze out of MATLAB. We are looking to continue this as a research software engineering project. Not only so that the shackles of proprietary software can be broken; but also so the full, ambitious vision of EasyDD can be realised.

# **Chapter 7**

## **Conclusions**



# Bibliography

- [1] Ellen G Howe and Ulrich Petersen. Silver and lead in the late prehistory of the mantaro valley, peru. *Archaeometry of pre-Columbian sites and artifacts*, pages 183–198, 1994.
- [2] John Chapman. *Fragmentation in archaeology: people, places and broken objects in the prehistory of south eastern Europe*. Routledge, 2013.
- [3] Kris MY Law and Marko Kesti. *Yin Yang and Organizational Performance: Five elements for improvement and success*. Springer, 2014.
- [4] Bryan K Hanks and Katheryn M Linduff. *Social complexity in prehistoric Eurasia: Monuments, metals and mobility*. Cambridge University Press, 2009.
- [5] Jared M Diamond. *Guns, germs and steel: a short history of everybody for the last 13,000 years*. Random House, 1998.
- [6] Arthur Wilson. *The living rock: the story of metals since earliest times and their impact on developing civilization*. Woodhead Publishing, 1994.
- [7] EW Hart. Theory of the tensile test. *Acta metallurgica*, 15(2):351–355, 1967.
- [8] SU Benscoter. A theory of torsion bending for multicell beams. *Journal of Applied Mechanics*, 21(1):25–34, 1954.
- [9] RF Bishop, Rodney Hill, and NF Mott. The theory of indentation and hardness tests. *Proceedings of the Physical Society*, 57(3):147, 1945.
- [10] S Zhandarov, E Pisanova, and B Lauke. Is there any contradiction between the stress and energy failure criteria in micromechanical tests? part i. crack initiation: stress-controlled or energy-controlled? *Composite Interfaces*, 5 (5):387–404, 1997.
- [11] Srinivasa D Thoppul and Ronald F Gibson. Mechanical characterization of spot friction stir welded joints in aluminum alloys by combined experi-

- mental/numerical approaches: part i: micromechanical studies. *Materials characterization*, 60(11):1342–1351, 2009.
- [12] Dierk Raabe, M Sachtleber, Zisu Zhao, Franz Roters, and Stefan Zaeferer. Micromechanical and macromechanical effects in grain scale polycrystal plasticity experimentation and simulation. *Acta Materialia*, 49(17):3433–3441, 2001.
  - [13] YW Kwon and JM Berner. Micromechanics model for damage and failure analyses of laminated fibrous composites. *Engineering Fracture Mechanics*, 52(2):231–242, 1995.
  - [14] Dierk Raabe, M Sachtleber, Zisu Zhao, Franz Roters, and Stefan Zaeferer. Micromechanical and macromechanical effects in grain scale polycrystal plasticity experimentation and simulation. *Acta Materialia*, 49(17):3433–3441, 2001.
  - [15] Risto M Nieminen. From atomistic simulation towards multiscale modelling of materials. *Journal of Physics: Condensed Matter*, 14(11):2859, 2002.
  - [16] JA Elliott. Novel approaches to multiscale modelling in materials science. *International Materials Reviews*, 56(4):207–225, 2011.
  - [17] Lihua Wang, Xiaodong Han, Pan Liu, Yonghai Yue, Ze Zhang, and En Ma. In situ observation of dislocation behavior in nanometer grains. *Physical review letters*, 105(13):135501, 2010.
  - [18] T Tabata and HK Birnbaum. Direct observations of the effect of hydrogen on the behavior of dislocations in iron. *Scripta Metallurgica*, 17(7):947–950, 1983.
  - [19] M Dao, L Lu, RJ Asaro, J Th M De Hosson, and E Ma. Toward a quantitative understanding of mechanical behavior of nanocrystalline metals. *Acta Materialia*, 55(12):4041–4065, 2007.
  - [20] MR Gilbert, SL Dudarev, S Zheng, LW Packer, and J-Ch Sublet. An integrated model for materials in a fusion power plant: transmutation, gas production, and helium embrittlement under neutron irradiation. *Nuclear Fusion*, 52(8):083019, 2012.
  - [21] Steven J Zinkle and GS Was. Materials challenges in nuclear energy. *Acta Materialia*, 61(3):735–758, 2013.

- [22] Ian Cook. Materials research for fusion energy. *Nature Materials*, 5(2):77, 2006.
- [23] Heinrich Hora. Developments in inertial fusion energy and beam fusion at magnetic confinement. *Laser and Particle Beams*, 22(04):439–449, 2004.
- [24] Weston M Stacey. *Fusion: an introduction to the physics and technology of magnetic confinement fusion*. John Wiley & Sons, 2010.
- [25] ROBERT L McCrory and CHARLES P Verdon. Inertial confinement fusion. *Computer Applications in Plasma Science and Engineering (Springer Science & Business Media, 2012)*, page 291, 2012.
- [26] Mohamed E Sawan. Geometrical, spectral and temporal differences between icf and mcf reactors and their impact on blanket nuclear parameters. *Fusion Technology*, 10(3P2B):1483–1488, 1986.
- [27] GL Kulcinski and ME Sawan. Differences between neutron damage in inertial and magnetic confinement fusion materials test facilities. *Journal of nuclear materials*, 133:52–57, 1985.
- [28] Steven J Zinkle and Jeremy T Busby. Structural materials for fission & fusion energy. *Materials Today*, 12(11):12–19, 2009.
- [29] Alban Mosnier, PY Beauvais, B Branas, M Comunian, A Facco, P Garin, R Gobin, JF Gournay, R Heidinger, A Ibarra, et al. The accelerator prototype of the ifmif/eveda project. *IPAC*, 10:588, 2010.
- [30] T Muroga, M Gasparotto, and SJ Zinkle. Overview of materials research for fusion reactors. *Fusion engineering and design*, 61:13–25, 2002.
- [31] JL Bourgade, AE Costley, R Reichle, ER Hodgson, W Hsing, V Glebov, M Decreton, R Leeper, JL Leray, M Dentan, et al. Diagnostic components in harsh radiation environments: Possible overlap in r&d requirements of inertial confinement and magnetic fusion systemsa). *Review of Scientific Instruments*, 79(10):10F304, 2008.
- [32] OA Hurricane, DA Callahan, DT Casey, PM Celliers, Charles Cerjan, EL Dewald, TR Dittrich, T Döppner, DE Hinkel, LF Berzak Hopkins, et al. Fuel gain exceeding unity in an inertially confined fusion implosion. *Nature*, 506(7488):343, 2014.
- [33] D Böhne, I Hofmann, G Kessler, GL Kulcinski, J Meyer-ter Vehn, U von Möllendorff, GA Moses, RW Müller, IN Sviatoslavsky, DK Sze, et al.

- Hiball—a conceptual design study of a heavy-ion driven inertial confinement fusion power plant. *Nuclear Engineering and Design*, 73(2):195–200, 1982.
- [34] John D Lindl, Robert L McCrory, and E Michael Campbell. Progress toward ignition and burn propagation in inertial confinement fusion. *Phys. Today*, 45(9):32–40, 1992.
  - [35] RW Moir, RL Bieri, XM Chen, TJ Dolan, MA Hoffman, PA House, RL Leber, JD Lee, YT Lee, JC Liu, et al. Hylife-ii: A molten-salt inertial fusion energy power plant design—final report. *Fusion Science and Technology*, 25(1):5–25, 1994.
  - [36] Roger E Stoller, Mychailo B Toloczko, Gary S Was, Alicia G Certain, Shyam Dwaraknath, and Frank A Garner. On the use of SRIM for computing radiation damage exposure. *Nuclear instruments and methods in physics research section B: beam interactions with materials and atoms*, 310:75–80, 2013.
  - [37] GH Kinchin and RS Pease. The displacement of atoms in solids by radiation. *Reports on progress in physics*, 18(1):1, 1955.
  - [38] James F Ziegler, Matthias D Ziegler, and Jochen P Biersack. SRIM—the stopping and range of ions in matter (2010). *Nuclear Instruments and Methods in Physics Research Section B: Beam Interactions with Materials and Atoms*, 268(11):1818–1823, 2010.
  - [39] Daniel Mason. Incorporating non-adiabatic effects in embedded atom potentials for radiation damage cascade simulations. *Journal of Physics: Condensed Matter*, 27(14):145401, 2015.
  - [40] AE Sand, SL Dudarev, and K Nordlund. High-energy collision cascades in tungsten: Dislocation loops structure and clustering scaling laws. *EPL (Europhysics Letters)*, 103(4):46003, 2013.
  - [41] T Diaz De La Rubia and MW Guinan. New mechanism of defect production in metals: A molecular-dynamics study of interstitial-dislocation-loop formation in high-energy displacement cascades. *Physical review letters*, 66(21):2766, 1991.
  - [42] V Barabash, G Federici, J Linke, and CH Wu. Material/plasma surface interaction issues following neutron damage. *Journal of Nuclear Materials*, 313:42–51, 2003.

- [43] Luke L Hsiung, Michael J Fluss, Scott J Tumey, B William Choi, Yves Serruys, Francois Willaime, and Akihiko Kimura. Formation mechanism and the role of nanoparticles in fe-cr ods steels developed for radiation tolerance. *Physical Review B*, 82(18):184103, 2010.
- [44] Xunxiang Hu, Takaaki Koyanagi, Makoto Fukuda, NAP Kiran Kumar, Lance L Snead, Brian D Wirth, and Yutai Katoh. Irradiation hardening of pure tungsten exposed to neutron irradiation. *Journal of Nuclear Materials*, 480:235–243, 2016.
- [45] AE Sand, SL Dudarev, and K Nordlund. High-energy collision cascades in tungsten: Dislocation loops structure and clustering scaling laws. *EPL (Europhysics Letters)*, 103(4):46003, 2013.
- [46] DEJ Armstrong, X Yi, EA Marquis, and SG Roberts. Hardening of self ion implanted tungsten and tungsten 5-wt% rhenium. *Journal of Nuclear Materials*, 432(1):428–436, 2013.
- [47] MR Gilbert and J-Ch Sublet. Neutron-induced transmutation effects in w and w-alloys in a fusion environment. *Nuclear Fusion*, 51(4):043005, 2011.
- [48] Robin A Forrest et al. *FISPACT-2007: User manual*. EURATOM/UKAEA fusion association, 2007.
- [49] Robin A Forrest, Michael G Sowerby, Bryan H Patrick, and David AJ Endacott. The data library ukact1 and the inventory code fispact. In *Nuclear data for science and technology*, 1988.
- [50] Makoto Fukuda, Kiyohiro Yabuuchi, Shuhei Nogami, Akira Hasegawa, and Teruya Tanaka. Microstructural development of tungsten and tungsten–rhenium alloys due to neutron irradiation in hfir. *Journal of Nuclear Materials*, 455(1):460–463, 2014.
- [51] Akira Hasegawa, Takashi Tanno, Shuhei Nogami, and Manabu Satou. Property change mechanism in tungsten under neutron irradiation in various reactors. *Journal of Nuclear Materials*, 417(1):491–494, 2011.
- [52] Akira Hasegawa, Makoto Fukuda, Kiyohiro Yabuuchi, and Shuhei Nogami. Neutron irradiation effects on the microstructural development of tungsten and tungsten alloys. *Journal of Nuclear Materials*, 471:175–183, 2016.
- [53] M Klimentov, U Jäntschi, M Rieth, HC Schneider, DEJ Armstrong, J Gibson, and SG Roberts. Effect of neutron irradiation on the microstructure of tungsten. *Nuclear Materials and Energy*, 2016.

- [54] Xiaou Yi, Michael L Jenkins, Marquis A Kirk, Zhongfu Zhou, and Steven G Roberts. In-situ tem studies of 150 kev w+ ion irradiated w and w-alloys: Damage production and microstructural evolution. *Acta Materialia*, 112: 105–120, 2016.
- [55] Alan Xu, Christian Beck, David EJ Armstrong, Krishna Rajan, George DW Smith, Paul AJ Bagot, and Steve G Roberts. Ion-irradiation-induced clustering in w-re and w-re-os alloys: A comparative study using atom probe tomography and nanoindentation measurements. *Acta Materialia*, 87:121–127, 2015.
- [56] Alan Xu, David EJ Armstrong, Christian Beck, Michael P Moody, George DW Smith, Paul AJ Bagot, and Steve G Roberts. Ion-irradiation induced clustering in w-re-ta, w-re and w-ta alloys: An atom probe tomography and nanoindentation study. *Acta Materialia*, 124:71–78, 2017.
- [57] Robert N Noyce. Microelectronics. *Scientific American*, 237(3):62–69, 1977.
- [58] Dermot Roddy. *Introduction to microelectronics*. Elsevier, 2013.
- [59] Kihwan Choi, Wonbok Lee, Ramakrishna Soma, and Massoud Pedram. Dynamic voltage and frequency scaling under a precise energy model considering variable and fixed components of the system power dissipation. In *Proceedings of the 2004 IEEE/ACM International conference on Computer-aided design*, pages 29–34. IEEE Computer Society, 2004.
- [60] Karel De Vogeeler, Gerard Memmi, Pierre Jouvelot, and Fabien Coelho. The energy/frequency convexity rule: Modeling and experimental validation on mobile devices. In *International Conference on Parallel Processing and Applied Mathematics*, pages 793–803. Springer, 2013.
- [61] NVidia, CUDA. NVidia CUDA C programming guide. *NVidia Corporation*, 120(18):8, 2011.
- [62] John Goodacre and Andrew N Sloss. Parallelism and the arm instruction set architecture. *Computer*, 38(7):42–50, 2005.
- [63] Stephen M Trimberger. *Field-programmable gate array technology*. Springer Science & Business Media, 2012.
- [64] Peter Wonka, Michael Wimmer, and Dieter Schmalstieg. Visibility preprocessing with occluder fusion for urban walkthroughs. In *Rendering Techniques 2000*, pages 71–82. Springer, 2000.

- [65] John A Flanders, David C Ready, Steven Van Seters, Leonard Schwartz, and William D Townsend. Hardware filtering method and apparatus, March 21 2000. US Patent 6,041,058.
- [66] Brian Kelleher and Thomas C Furlong. Software configurable memory architecture for data processing system having graphics capability, August 28 1990. US Patent 4,953,101.
- [67] Masayuki Sumi. Image processing devices and methods, March 31 1998. US Patent 5,734,807.
- [68] Joseph Celi Jr, Jonathan M Wagner, and Roger Louie. Advanced graphics driver architecture, February 3 1998. US Patent 5,715,459.
- [69] Thomas J Bensky and SE Frey. Computer sound card assisted measurements of the acoustic doppler effect for accelerated and unaccelerated sound sources. *American Journal of Physics*, 69(12):1231–1236, 2001.
- [70] Daniel E Evanicky. Enhanced viewing experience of a display through localised dynamic control of background lighting level, April 9 2013. US Patent 8,416,149.
- [71] Rolf Rabenseifner, Georg Hager, and Gabriele Jost. Hybrid mpi/openmp parallel programming on clusters of multi-core smp nodes. In *Parallel, Distributed and Network-based Processing, 2009 17th Euromicro International Conference on*, pages 427–436. IEEE, 2009.
- [72] John Nickolls and William J Dally. The gpu computing era. *IEEE micro*, 30(2), 2010.
- [73] John E Stone, David Gohara, and Guochun Shi. Opencl: A parallel programming standard for heterogeneous computing systems. *Computing in science & engineering*, 12(3):66–73, 2010.
- [74] Ruymán Reyes, Iván López, Juan J Fumero, and Francisco de Sande. A preliminary evaluation of openacc implementations. *The Journal of Supercomputing*, 65(3):1063–1075, 2013.
- [75] Vipin Kumar, Ananth Grama, Anshul Gupta, and George Karypis. *Introduction to parallel computing: design and analysis of algorithms*, volume 400. Benjamin/Cummings Redwood City, 1994.
- [76] Cristobal A Navarro, Nancy Hitschfeld-Kahler, and Luis Mateu. A survey on parallel computing and its applications in data-parallel problems using gpu

- architectures. *Communications in Computational Physics*, 15(2):285–329, 2014.
- [77] YJ Lee and LB Freund. Fracture initiation due to asymmetric impact loading of an edge cracked plate. *Journal of Applied Mechanics*, 57(1):104–111, 1990.
  - [78] Stefan Sandfeld, Thomas Hochrainer, Peter Gumbsch, and Michael Zaiser. Numerical implementation of a 3d continuum theory of dislocation dynamics and application to micro-bending. *Philosophical Magazine*, 90(27-28):3697–3728, 2010.
  - [79] Vasily Bulatov, Wei Cai, Jeff Fier, Masato Hiratani, Gregg Hommes, Tim Pierce, Meijie Tang, Moono Rhee, Kim Yates, and Tom Arsenlis. Scalable line dynamics in paradis. In *Proceedings of the 2004 ACM/IEEE conference on Supercomputing*, page 19. IEEE Computer Society, 2004.
  - [80] MP O’day and William A Curtin. A superposition framework for discrete dislocation plasticity. *Transactions of the ASME-E-Journal of Applied Mechanics*, 71(6):805–815, 2004.
  - [81] Robert Gracie, Giulio Ventura, and Ted Belytschko. A new fast finite element method for dislocations based on interior discontinuities. *International Journal for Numerical Methods in Engineering*, 69(2):423–441, 2007.
  - [82] Franz Roters, Philip Eisenlohr, Luc Hantcherli, Denny Dharmawan Tjahjanto, Thomas R Bieler, and Dierk Raabe. Overview of constitutive laws, kinematics, homogenization and multiscale methods in crystal plasticity finite-element modeling: Theory, experiments, applications. *Acta Materialia*, 58(4):1152–1211, 2010.
  - [83] El Arzt. Size effects in materials due to microstructural and dimensional constraints: a comparative review. *Acta materialia*, 46(16):5611–5626, 1998.
  - [84] R Madec, B Devincre, L Kubin, T Hoc, and D Rodney. The role of collinear interaction in dislocation-induced hardening. *Science*, 301(5641):1879–1882, 2003.
  - [85] Francesco Ferroni, Edmund Tarleton, and Steven Fitzgerald. Gpu accelerated dislocation dynamics. *Journal of Computational Physics*, 272:619–628, 2014.
  - [86] S Queyreau, J Marian, BD Wirth, and A Arsenlis. Analytical integration of the forces induced by dislocations on a surface element. *Modelling and Simulation in Materials Science and Engineering*, 22(3):035004, 2014.

- [87] Erik Van der Giessen and Alan Needleman. Discrete dislocation plasticity: a simple planar model. *Modelling and Simulation in Materials Science and Engineering*, 3(5):689, 1995.
- [88] B Devincre, A Roos, and S Groh. Boundary problems in dd simulations. In *In: Thermodynamics, Microstructures and Plasticity, A. Finel et al., Nato Sciences Series II: Mathematics, Physics and Chemistry, 108, p. 275, Eds (Kluwer, NL-Dordrecht. Citeseer, 2003.*
- [89] CS Shin, MC Fivel, and KH Oh. Nucleation and propagation of dislocations near a precipitate using 3d discrete dislocation dynamics simulations. *Le Journal de Physique IV*, 11(PR5):Pr5–27, 2001.
- [90] MC Fivel and GR Canova. Developing rigorous boundary conditions to simulations of discrete dislocation dynamics. *Modelling and Simulation in Materials Science and Engineering*, 7(5):753, 1999.
- [91] Akiyuki Takahashi and Nasr M Ghoniem. A computational method for dislocation–precipitate interaction. *Journal of the Mechanics and Physics of Solids*, 56(4):1534–1553, 2008.
- [92] O Jamond, R Gatti, A Roos, and B Devincre. Consistent formulation for the discrete-continuous model: Improving complex dislocation dynamics simulations. *International Journal of Plasticity*, 80:19–37, 2016.
- [93] Toshio Mura. *Micromechanics of defects in solids*. Springer Science & Business Media, 2013.
- [94] G Saada and XL Shi. Description of dislocation cores. *Czechoslovak Journal of Physics*, 45(11):979–989, 1995.
- [95] A Vattré, B Devincre, F Feyel, R Gatti, S Groh, O Jamond, and A Roos. Modelling crystal plasticity by 3d dislocation dynamics and the finite element method: the discrete-continuous model revisited. *Journal of the Mechanics and Physics of Solids*, 63:491–505, 2014.
- [96] Yang Xiang and DJ Srolovitz. Dislocation climb effects on particle bypass mechanisms. *Philosophical magazine*, 86(25-26):3937–3957, 2006.
- [97] Yang Xiang, Li-Tien Cheng, David J Srolovitz, and E Weinan. A level set method for dislocation dynamics. *Acta Materialia*, 51(18):5499–5518, 2003.
- [98] Siu Sin Quek, Yang Xiang, and David J Srolovitz. Loss of interface coherency around a misfitting spherical inclusion. *Acta Materialia*, 59(14):5398–5410, 2011.

- [99] John P Hirth and Jens Lothe. Theory of dislocations. 1982.
- [100] Toshio Mura. *Micromechanics of defects in solids*. Springer Science & Business Media, 2013.
- [101] Wei Cai, Athanasios Arsenlis, Christopher R Weinberger, and Vasily V Bulatov. A non-singular continuum theory of dislocations. *Journal of the Mechanics and Physics of Solids*, 54(3):561–587, 2006.
- [102] R De Wit. Some relations for straight dislocations. *physica status solidi (b)*, 20(2):567–573, 1967.
- [103] R De Wit. The self-energy of dislocation configurations made up of straight segments. *physica status solidi (b)*, 20(2):575–580, 1967.
- [104] Vladimir L Indenbom and Jens Lothe. *Elastic strain fields and dislocation mobility*. Elsevier, 2012.
- [105] Bernard Fedelich. The glide force on a dislocation in finite elasticity. *Journal of the Mechanics and Physics of Solids*, 52(1):215–247, 2004.
- [106] M Yu Gutkin and EC Aifantis. Screw dislocation in gradient elasticity. *Scripta Materialia*, 35(11):1353–1358, 1996.
- [107] M Yu Gutkin and EC Aifantis. Edge dislocation in gradient elasticity. *Scripta Materialia*, 36(1):129–135, 1997.
- [108] LM Brown. The self-stress of dislocations and the shape of extended nodes. *Philosophical Magazine*, 10(105):441–466, 1964.
- [109] SD Gavazza and DM Barnett. The self-force on a planar dislocation loop in an anisotropic linear-elastic medium. *Journal of the Mechanics and Physics of Solids*, 24(4):171–185, 1976.
- [110] R Peierls. The size of a dislocation. *Proceedings of the Physical Society*, 52(1):34, 1940.
- [111] FRN Nabarro. Dislocations in a simple cubic lattice. *Proceedings of the Physical Society*, 59(2):256, 1947.
- [112] K Gururaj and C Robertson. Plastic deformation in ods ferritic alloys: A 3d dislocation dynamics investigation. *Energy Procedia*, 7:279–285, 2011.
- [113] Zhenhuan Li, Chuantao Hou, Minsheng Huang, and Chaojun Ouyang. Strengthening mechanism in micro-polycrystals with penetrable grain

- boundaries by discrete dislocation dynamics simulation and hall-petch effect. *Computational Materials Science*, 46(4):1124–1134, 2009.
- [114] Haidong Fan, Zhenhuan Li, Minsheng Huang, and Xiong Zhang. Thickness effects in polycrystalline thin films: Surface constraint versus interior constraint. *International Journal of Solids and Structures*, 48(11-12):1754–1766, 2011.
  - [115] Z Shen, RH Wagoner, and WAT Clark. Dislocation pile-up and grain boundary interactions in 304 stainless steel. *Scripta metallurgica*, 20(6):921–926, 1986.
  - [116] Z Shen, RH Wagoner, and WAT Clark. Dislocation and grain boundary interactions in metals. *Acta metallurgica*, 36(12):3231–3242, 1988.
  - [117] GC Hasson and C Goux. Interfacial energies of tilt boundaries in aluminium. experimental and theoretical determination. *Scripta metallurgica*, 5(10):889–894, 1971.
  - [118] Haidong Fan, Sylvie Aubry, Athanasios Arsenlis, and Jaafar A El-Awady. The role of twinning deformation on the hardening response of polycrystalline magnesium from discrete dislocation dynamics simulations. *Acta Materialia*, 92:126–139, 2015.
  - [119] S Lay and G Nouet. Interaction of slip dislocations with the  $(01\ 1\ 2)$  twin interface in zinc. *Philosophical Magazine A*, 70(6):1027–1044, 1994.
  - [120] JI Dickson and C Robin. The incorporation of slip dislocations in  $\{1102\}$  twins in zirconium. *Materials Science and Engineering*, 11(5):299–302, 1973.
  - [121] DI Tomsett and M Bevis. The incorporation of basal slip dislocations in  $\{10\ 1\ 2\}$  twins in zinc crystals. *Philosophical Magazine*, 19(157):129–140, 1969.
  - [122] MH Yoo and CT Wei. Slip modes of hexagonal-close-packed metals. *Journal of Applied Physics*, 38(11):4317–4322, 1967.
  - [123] A Serra and DJ Bacon. A new model for  $\{10\ 1\ 2\}$  twin growth in hcp metals. *Philosophical Magazine A*, 73(2):333–343, 1996.
  - [124] Jindong Wang, Gen He, Jinwen Qin, Lidong Li, and Xuefeng Guo. Preparation of silicon nanowires by in situ doping and their electrical properties. *Colloids and Surfaces A: Physicochemical and Engineering Aspects*, 450:156–160, 2014.

- [125] Kisaragi Yashiro, F Kurose, Y Nakashima, K Kubo, Yoshihiro Tomita, and HM Zbib. Discrete dislocation dynamics simulation of cutting of  $\gamma$  precipitate and interfacial dislocation network in ni-based superalloys. *International Journal of Plasticity*, 22(4):713–723, 2006.
- [126] A Vattré, B Devincre, and A Roos. Orientation dependence of plastic deformation in nickel-based single crystal superalloys: Discrete–continuous model simulations. *Acta Materialia*, 58(6):1938–1951, 2010.
- [127] SI Rao S, TA Parthasarathy, DM Dimiduk, and PM Hazzledine. Discrete dislocation simulations of precipitation hardening in superalloys. *Philosophical Magazine*, 84(30):3195–3215, 2004.
- [128] Hesam Askari, Hussein M Zbib, and Xin Sun. Multiscale modeling of inclusions and precipitation hardening in metal matrix composites: Application to advanced high-strength steels. *Journal of Nanomechanics and Micromechanics*, 3(2):24–33, 2012.
- [129] Vasily Bulatov and Wei Cai. *Computer simulations of dislocations*, volume 3. Oxford University Press on Demand, 2006.
- [130] Haiyang Yu, Alan Cocks, and Edmund Tarleton. Discrete dislocation plasticity helps understand hydrogen effects in bcc materials. *Journal of the Mechanics and Physics of Solids*, 2018. ISSN 0022-5096. doi: <https://doi.org/10.1016/j.jmps.2018.08.020>.
- [131] N Bertin, S Aubry, A Arsenlis, and W Cai. Gpu-accelerated dislocation dynamics using subcycling time-integration. *Modelling and Simulation in Materials Science and Engineering*, 27(7):075014, 2019.
- [132] Athanasios Arsenlis, Wei Cai, Meijie Tang, Moono Rhee, Tomas Oppelstrup, Gregg Hommes, Tom G Pierce, and Vasily V Bulatov. Enabling strain hardening simulations with dislocation dynamics. *Modelling and Simulation in Materials Science and Engineering*, 15(6):553, 2007.
- [133] B Bromage and E Tarleton. Calculating dislocation displacements on the surface of a volume. *Modelling and Simulation in Materials Science and Engineering*, 26(8):085007, 2018.
- [134] E Ward Cheney and David R Kincaid. *Numerical mathematics and computing*. Cengage Learning, 2012.

- [135] Paul Rodríguez. Total variation regularization algorithms for images corrupted with different noise models: a review. *Journal of Electrical and Computer Engineering*, 2013, 2013.
- [136] Peter J Bickel, Bo Li, Alexandre B Tsybakov, Sara A van de Geer, Bin Yu, Teófilo Valdés, Carlos Rivero, Jianqing Fan, and Aad van der Vaart. Regularization in statistics. *Test*, 15(2):271–344, 2006.
- [137] Zhanxuan Hu, Feiping Nie, Rong Wang, and Xuelong Li. Low rank regularization: A review. *Neural Networks*, 2020.
- [138] Coronavirus (covid-19): modelling the epidemic. URL <https://www.gov.scot/collections/coronavirus-covid-19-modelling-the-epidemic/>.
- [139] Grant Hill-Cawthorne. Models of covid-19: Part 1, Dec 2020. URL <https://post.parliament.uk/models-of-covid-19-part-1/>.
- [140] Grant Hill-Cawthorne. Models of covid-19: Part 2, Dec 2020. URL <https://post.parliament.uk/models-of-covid-19-part-2/>.
- [141] Dalmeet Singh Chawla. Critiqued coronavirus simulation gets thumbs up from code-checking efforts, Jun 2020. URL <https://www.nature.com/articles/d41586-020-01685-y>.
- [142] Niels G Mede, Mike S Schäfer, Ricarda Ziegler, and Markus Weißkopf. The “replication crisis” in the public eye: Germans’ awareness and perceptions of the (ir) reproducibility of scientific research. *Public Understanding of Science*, page 0963662520954370, 2020.
- [143] David Randall and Christopher Welser. *The Irreproducibility Crisis of Modern Science: Causes, Consequences, and the Road to Reform*. ERIC, 2018.
- [144] Roberto Bolli. Reflections on the irreproducibility of scientific papers. *Circulation research*, 117(8):665–666, 2015.
- [145] Simon Thompson. *Haskell: the craft of functional programming*, volume 2. Addison-Wesley, 2011.
- [146] Konrad Hinsen. The promises of functional programming. *Computing in Science & Engineering*, 11(4):86–90, 2009.
- [147] Donald E Knuth. Structured programming with go to statements. *ACM Computing Surveys (CSUR)*, 6(4):261–301, 1974.

- [148] David R Hanson. Fast allocation and deallocation of memory based on object lifetimes. *Software: Practice and Experience*, 20(1):5–12, 1990.
- [149] M Verdier, M Fivel, and I Groma. Mesoscopic scale simulation of dislocation dynamics in fcc metals: Principles and applications. *Modelling and Simulation in Materials Science and Engineering*, 6(6):755, 1998.
- [150] C. Déprés, C. F. Robertson, and M. C. Fivel. Low-strain fatigue in 316l steel surface grains: a three dimension discrete dislocation dynamics modelling of the early cycles. part 2: Persistent slip markings and micro-crack nucleation. *Philosophical Magazine*, 86(1):79–97, 2006. doi: 10.1080/14786430500341250.
- [151] E Tarleton, DS Balint, J Gong, and AJ Wilkinson. A discrete dislocation plasticity study of the micro-cantilever size effect. *Acta Materialia*, 88:271–282, 2015.
- [152] S. Groh and H. M. Zbib. Advances in Discrete Dislocations Dynamics and Multiscale Modeling. *Journal of Engineering Materials and Technology*, 131(4):041209, 2009. ISSN 00944289. doi: 10.1115/1.3183783.
- [153] Erik Van der Giessen and Alan Needleman. Discrete dislocation plasticity: a simple planar model. *Modelling and Simulation in Materials Science and Engineering*, 3(5):689, 1995.
- [154] MC Fivel and GR Canova. Developing rigorous boundary conditions to simulations of discrete dislocation dynamics. *Modelling and Simulation in Materials Science and Engineering*, 7(5):753, 1999.
- [155] Akiyuki Takahashi and Nasr M Ghoniem. A computational method for dislocation–precipitate interaction. *Journal of the Mechanics and Physics of Solids*, 56(4):1534–1553, 2008.
- [156] B Devincre, A Roos, and S Groh. Boundary problems in dd simulations. In *In: Thermodynamics, Microstructures and Plasticity, A. Finel et al., Nato Sciences Series II: Mathematics, Physics and Chemistry, 108, p. 275, Eds (Kluwer, NL-Dordrecht. Citeseer, 2003.*
- [157] CS Shin, MC Fivel, and KH Oh. Nucleation and propagation of dislocations near a precipitate using 3d discrete dislocation dynamics simulations. *Le Journal de Physique IV*, 11(PR5):Pr5–27, 2001.

- [158] M. P. O'Day and W. a. Curtin. A Superposition Framework for Discrete Dislocation Plasticity. *Journal of Applied Mechanics*, 71(November 2004): 805, 2004. ISSN 00218936. doi: 10.1115/1.1794167.
- [159] Gene H Golub and John H Welsch. Calculation of gauss quadrature rules. *Mathematics of computation*, 23(106):221–230, 1969.
- [160] Michael A Khayat and Donald R Wilton. Numerical evaluation of singular and near-singular potential integrals. *IEEE Transactions on Antennas and Propagation*, 53(10):3180–3190, 2005.
- [161] AK Head. Edge dislocations in inhomogeneous media. *Proceedings of the Physical Society. Section B*, 66(9):793, 1953.
- [162] John Price Hirth, Jens Lothe, and T Mura. Theory of dislocations, 1983.
- [163] Shengquan Wang, Chao Wang, Yong Cai, and Guangyao Li. A novel parallel finite element procedure for nonlinear dynamic problems using gpu and mixed-precision algorithm. *Engineering Computations*, 2020.
- [164] Xun Jia, Peter Ziegenhein, and Steve B Jiang. Gpu-based high-performance computing for radiation therapy. *Physics in Medicine & Biology*, 59(4): R151, 2014.
- [165] Amir Sabbagh Molahosseini and Hans Vandierendonck. Half-precision floating-point formats for pagerank: Opportunities and challenges. In *2020 IEEE High Performance Extreme Computing Conference (HPEC)*, pages 1–7. IEEE, 2020.
- [166] Carlos Carvalho. The gap between processor and memory speeds. In *Proc. of IEEE International Conference on Control and Automation*, 2002.
- [167] Bin Wang, Weikuan Yu, Xian-He Sun, and Xinning Wang. Docache: Memory divergence-aware gpu cache management. In *Proceedings of the 29th ACM on International Conference on Supercomputing*, pages 89–98, 2015.
- [168] Cedric Nugteren, Gert-Jan Van den Braak, Henk Corporaal, and Henri Bal. A detailed gpu cache model based on reuse distance theory. In *2014 IEEE 20th International Symposium on High Performance Computer Architecture (HPCA)*, pages 37–48. IEEE, 2014.
- [169] Martin Schindewolf, Jie Tao, Wolfgang Karl, and Marcelo Cintra. A generic tool supporting cache design and optimisation on shared memory systems. In *9th workshop on parallel systems and algorithms–workshop of the GI/ITG*

*special interest groups PARS and PARVA.* Gesellschaft für Informatik e. V., 2008.

- [170] Lu Wang, Magnus Jahre, Almutaz Adileho, and Lieven Eeckhout. Mdm: The gpu memory divergence model. In *2020 53rd Annual IEEE/ACM International Symposium on Microarchitecture (MICRO)*, pages 1009–1021. IEEE, 2020.
- [171] Andrea Elisabet Sand, Kai Nordlund, and SL Dudarev. Radiation damage production in massive cascades initiated by fusion neutrons in tungsten. *Journal of Nuclear Materials*, 455(1-3):207–211, 2014.
- [172] Yang Li, Max Boleininger, Christian Robertson, Laurent Dupuy, and Sergei L Dudarev. Diffusion and interaction of prismatic dislocation loops simulated by stochastic discrete dislocation dynamics. *Physical Review Materials*, 3(7):073805, 2019.
- [173] Jeff Bezanson, Alan Edelman, Stefan Karpinski, and Viral B Shah. Julia: A fresh approach to numerical computing. *SIAM review*, 59(1):65–98, 2017.  
URL <https://doi.org/10.1137/141000671>.

tran\_Binding